

Energy & Environmental Science

Accepted Manuscript

This article can be cited before page numbers have been issued, to do this please use: X. Li, J. liang, X. Yang, K. Adair, C. Wang, F. Zhao and X. Sun, *Energy Environ. Sci.*, 2020, DOI: 10.1039/C9EE03828K.



This is an Accepted Manuscript, which has been through the Royal Society of Chemistry peer review process and has been accepted for publication.

Accepted Manuscripts are published online shortly after acceptance, before technical editing, formatting and proof reading. Using this free service, authors can make their results available to the community, in citable form, before we publish the edited article. We will replace this Accepted Manuscript with the edited and formatted Advance Article as soon as it is available.

You can find more information about Accepted Manuscripts in the [Information for Authors](#).

Please note that technical editing may introduce minor changes to the text and/or graphics, which may alter content. The journal's standard [Terms & Conditions](#) and the [Ethical guidelines](#) still apply. In no event shall the Royal Society of Chemistry be held responsible for any errors or omissions in this Accepted Manuscript or any consequences arising from the use of any information it contains.

Progress and Perspectives for Halide Solid-State Electrolyte for All-Solid-State Lithium Batteries

*Xiaona Li,⁺ Jianwen Liang,⁺ Xiaofei Yang, Keegan R. Adair, Changhong Wang, Feipeng Zhao, and Xueliang Sun**

Department of Mechanical and Materials Engineering, University of Western Ontario, 1151 Richmond St, London, Ontario, N6A 3K7, Canada.

*Corresponding email: xsun9@uwo.ca

Abstract

Halide solid-state electrolytes (SSEs) with high room-temperature ionic conductivity ($>10^{-3}$ S cm⁻¹), wide electrochemical windows, and good compatibility toward oxide cathode materials have achieved impressive progress and attracted significant attention for application in all-solid-state lithium batteries (ASSLBs). This review presents an overview of the halide SSEs, including their development, structure, ionic conductivity, chemical stability, and current limitations. Firstly, we give a brief overview of the historical development of halide-based SSEs, followed by an introduction to the different types of halide SSEs. From a practical point of view, the synthesis methods, especially scalable liquid-phase synthesis, are intensively discussed. Then, the associated stability issues involving basic structure stability, air/humidity stability, and electrochemical stability (electrolyte/SSE interface and electrochemical stability window) are also discussed in detail. Comprehensive coverage and thorough understanding of the properties of halide SSEs are provided and it is expected to help guide the development of future SSEs towards ASSLBs for energy storage applications.

Keyword: halide, lithium conductor, all-solid-state battery, energy storage, antiperovskite

Outline

View Article Online
DOI: 10.1039/C9EE03828K

1. Introduction
2. The state-of-the-arts of various halide SSEs
 - 2.1 Halide SSEs with group 3 elements (Sc, Y, La-Lu)
 - 2.2 Halide SSEs with group 13 elements (Al, Ga, In)
 - 2.3 Halide SSEs with divalent metal elements (Ti, V, Cr, Mn, Fe, Co, Ni, Cu, Zn, Cd, Mg, Pb)
 - 2.3.1 Olivine structure
 - 2.3.2 Spinel structure
 - 2.3.3 Distorted structure
 - 2.3.4 Suzuki structure (deficient LiCl-type)
 - 2.4 Halide SSEs with non-metal elements (N, O, S)
3. Synthesis
 - 3.1 Solid-state reaction method (Mechanical milling, annealing)
 - 3.2 Liquid-phase synthesis
 - 3.2.1 Water-mediated synthesis of Li_3InCl_6 SSE
 - 3.2.2 Possible other liquid synthesis route based on halide hydrated complexes
 - 3.3 Chemical vapor synthesis
4. Chemical/electrochemical stability
 - 4.1 Structure stability (temperature influence)
 - 4.2 Stability toward air/humidity
 - 4.3 Stability toward electrodes
 - 4.3.1 Stability toward cathodes
 - 4.3.2 Stability toward anodes
 - 4.4 Electrochemically stable window
5. Applications of halide SSEs in energy storage
 - 5.1 Applications of halide SSEs
 - 5.2 Evaluation of the energy density for halide-based solid-state lithium batteries
6. Summary and Perspective

1. Introduction

The development of rechargeable batteries with high specific energy and extended lifetime is urgently required to satisfy the stringent demands of large-scale energy-storage devices and various consumer electronics. Conventional lithium-ion batteries (LIBs) that revolutionized the portable electronics industry are widely used in daily life.¹ However, the rapidly growing application of LIBs has raised concerns regarding their physicochemical energy density limit and potential safety risks caused by the flammable organic liquid electrolytes. All-solid-state lithium batteries (ASSLBs) utilizing solid-state electrolytes (SSEs) rather than combustible liquid electrolytes not only possess enhanced safety, but may also offer new opportunities for the utilization of high voltage cathode materials (such as $\text{LiNi}_{0.5}\text{Mn}_{1.5}\text{O}_4$) and high-capacity electrodes (such as Li/Na anodes and sulfur cathodes) to achieve high-energy-density batteries.^{2, 3} In addition, ASSLBs also possess further advantages including SSEs with high Li^+ transference numbers, versatile geometries, simple battery design as well as a wide range of operating temperature.⁴⁻⁷

In this context, SSEs are one of the most vital components in ASSLBs as the performance of ASSLBs is highly dependent on the properties of SSEs. To realize ASSLBs that can operate at ambient temperatures, the primary parameters that must be considered are high room-temperature (RT) ionic conductivity ($>10^{-3} \text{ S cm}^{-1}$) and a wide electrochemical stable window. Hitherto, current research efforts on SSEs focus mostly on oxides,^{8, 9} sulfide,^{5, 10} and borohydrides,^{11, 12} which present RT ionic conductivity as high as $10^{-2} \text{ S cm}^{-1}$ (mostly in the case of sintered pellets rather than cold-pressed).^{4, 5, 13} Compared to those SSEs, the development of halide SSEs has been delayed due to the view of low ionic conductivity ($\sim 10^{-5} \text{ S cm}^{-1}$) and low oxidation voltage.^{2, 3} Nevertheless, the recent experimental¹⁴⁻¹⁶ and theoretical¹⁷⁻²¹ results demonstrate that halide SSEs are quite promising due to their high RT ionic conductivity ($>10^{-3} \text{ S cm}^{-1}$, theoretically possible $10^{-2} \text{ S cm}^{-1}$), wide electrochemical stable window (up to 6 V), good stability toward oxide cathode materials, and even soluble water synthesis

strategies¹⁶. These new developments make it necessary to revisit the halide SSEs regarding their development, properties, and potential practical applications in energy storage systems.

The timeline of the development of halide SSEs is shown in Figure 1. Ionic conductive behavior was reported for lithium halides (LiX, X = F, Cl, Br, I) in the 1930s.²² However, LiX shows a relatively low RT ionic conductivity with the highest value achieved for LiI of $10^{-7} \text{ S cm}^{-1}$.²³⁻²⁵ With the discoveries of lithium ionic conductivity in LiX, thin-film type ASSLBs with LiI as SSE were developed at the end of the 1960s and the beginning of 1970s, such as Li/LiI/I₂ and Li/LiI/AgI, with open-circuit voltages around 2.45-3 V.^{26, 27, 28} However, those ASSLBs can not be recharged due to the increasing polarization caused by continuous LiI formation in the cathode/SSE interface. Later, another typical halide SSE of LiAlCl₄ was developed and applied in battery systems. Interestingly, molten LiCl-AlCl₃ was reported to possess an ionic conductivity of 0.35 S cm^{-1} at 174 °C in 1941, and has been applied in thermal batteries.²⁹ More commonly, LiAlCl₄ was dissolved in nonaqueous solvents (such as SOCl₂, butyrolactone) to function as a soluble cathode or electrolyte in lithium batteries.³⁰⁻³² The ionic conductivity of solid LiAlCl₄ was not reported until 1976, which is around $10^{-6} \text{ S cm}^{-1}$ (RT),^{33, 34} In 1992, E. J. Plichta and W. K. Behl successfully assembled a thin-film type Li_xTiS₂/LiAlCl₄/Li_{1-x}CoO₂ ASSLB which can cycle more than 150 cycles when operated at 100 °C.³⁵

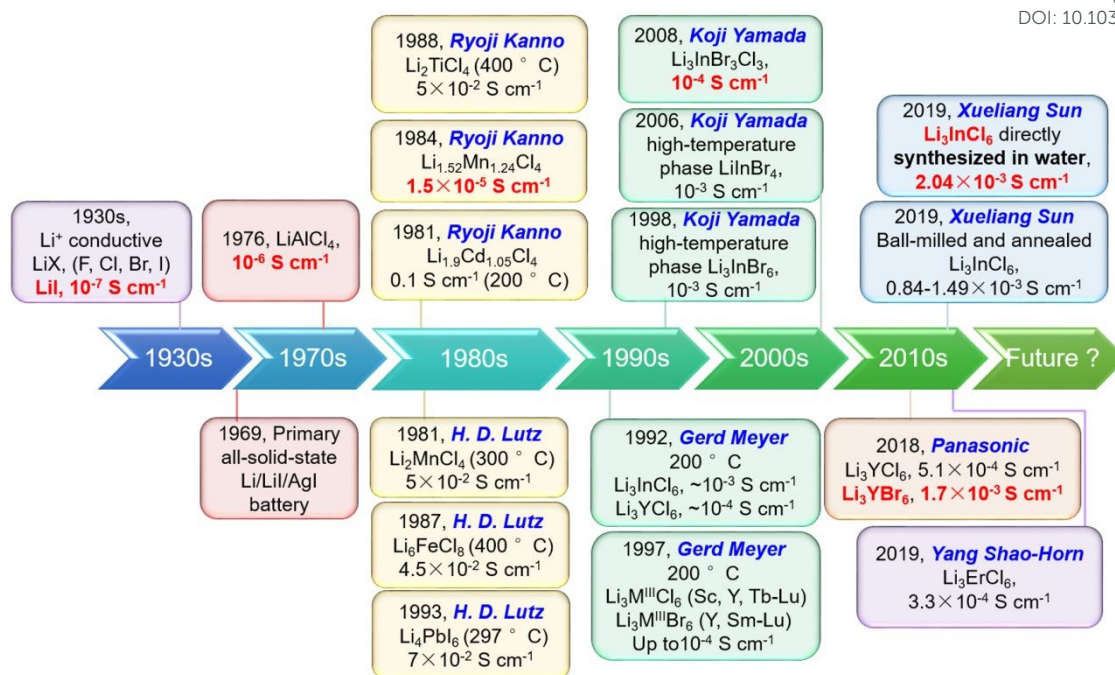


Figure 1. A brief chronology of the development of halide SSEs for ASSLBs.

In the 1980s-1990s, halide spinels which are mainly based on divalent metal cations (mainly the first transition metals and Mg, Pb, etc.) were systematically studied by Ryoji Kanno, H. D. Lutz, and other groups. The fluoride type SSEs showed relatively lower (RT) ionic conductivity around $10^{-8}\text{--}10^{-6} \text{ S cm}^{-1}$, and the lithium transference number is likely not 1 due to some contribution of F⁻ anions.³⁶⁻³⁸ The most studied are chloride- and bromide-based spinel types, which showed RT ionic conductivities up to $\sim 10^{-5} \text{ S cm}^{-1}$ and $\sim 10^{-1} \text{ S cm}^{-1}$ at 400 °C, respectively.^{39,40, 41} In addition to those containing divalent metal cations, halide SSEs with trivalent metal cations (mainly group 3 elements of Sc, Y, La-Lu, and group 13 elements of Ga, In) were also developed. Among them, the most studied halide type SSE is Li_3InBr_6 since 1998.⁴² The as-synthesized Li_3InBr_6 exhibits a relatively low RT ionic conductivity of $10^{-7} \text{ S cm}^{-1}$. Moreover, Li_3InBr_6 will undergo a phase transition during the heating process. The high-temperature phase Li_3InBr_6 (HT Li_3InBr_6) remained stable when cooling down and possess a RT ionic conductivity of $10^{-3} \text{ S cm}^{-1}$. Nevertheless, such a high-temperature structure will again degrade and yield significantly reduced ionic conductivity at -13 °C, which makes it not suitable for practical application. As can be concluded, the halide SSEs were proposed during the same period

as other types SSEs. Nevertheless, the relatively low ionic conductivity of halide SSEs compared to the fast development of other types SSEs (even 10^{-2} S cm $^{-1}$ for sulfide SSEs at 25 °C), made the halide SSEs relatively less attractive during the past years.

Until 2018, limited work has been conducted on halide SSEs with RT ionic conductivities on the order of 10^{-3} S cm $^{-1}$. A significant breakthrough was achieved by Tetsuya Asano et al. in 2018, where they synthesized Li₃YCl₆ and Li₃YBr₆ halide SSEs with high ionic conductivity of 0.03-1.7×10⁻³ S cm $^{-1}$ by using a high-energy ball milling and high-temperature annealing process.¹⁴ Subsequently, several other kinds of halide SSEs, such as Li₃ErCl₆ (0.17-3.3×10⁻⁴ S cm $^{-1}$),^{43, 44} Li₃InCl₆ (0.84-2.04×10⁻³ S cm $^{-1}$),^{15, 16} Li_{3-x}M_{1-x}Zr_xCl₆ (M = Y, Er, up to 1.4×10⁻³ S cm $^{-1}$),⁴⁵ and Li₃ErI₆ (3.9-6.5×10⁻⁴ S cm $^{-1}$)⁴⁶ were also developed. Remarkably, Li₃InCl₆ SSEs can be synthesized by a facile and scalable water-mediated synthesis route, and the high ionic conductivity is recoverable even after being redissolved into water.¹⁶ More recently, significant attention has been paid to halide SSEs and their application in ASSLBs. Halide SSEs present several advantages concerning other types of SSEs in terms of wide electrochemical windows, no side reaction with oxide cathode materials, good air stability, high humidity tolerance, and scalability.

In this review, we report on the progress of the halide SSEs for ASSLBs. Furthermore, we conclude with a discussion of 1) the development and different types of halide SSEs; 2) the different synthesis routes, including the promising liquid-phase synthesis route for halide SSEs; 3) chemical/electrochemical stability of halide SSEs, including thermal stability, air/humidity stability, stability toward cathode/anode, and intrinsic electrochemical stability windows; 4) potential application of halide SSEs in energy storage and evaluation of energy/volume densities of pouch cell. Finally, we discuss the challenges in realizing halide SSEs for practical applications in energy storage and offer perspectives on future opportunities and research directions.

2. The state-of-the-arts of various halide SSEs

Halide SSEs were rarely systematically summarized in previous reviews, and their definition and classification are relatively unclear. For example, Li_aMX_b ($X = \text{F}, \text{Cl}, \text{Br}, \text{I}$) ternary compounds with various metal elements, such as Li_2CdCl_4 , Li_2MgCl_4 , Li_2ZnI_4 , and Li_2CdI_4 , were classified as halide SSEs by Yang Shao-Horn et al. in their review paper.³ Comparatively, Arumugam Manthiram et al. also summarized typical anti-perovskite Li_3OCl as a halide SSE in their review paper, which means the central element can not only be metal but also nonmetal element.² However, it should be noted that the properties of them are quite different. For example, the halide SSEs with nonmetal elements (such as Li_3OCl) show relatively good stability with lithium metal while possessing a quite narrow electrochemical window (up to 2.55 or 3 V vs. Li/Li^+ for Li_3OCl);⁴⁷ however, the halide SSEs with metal elements (such as Li_3YCl_6) are typically unstable against lithium metal but possess a wider electrochemical window (0.62–4.21 V vs. Li/Li^+).¹⁷ The non-Li cation plays an important role to realize high-performance halide SSEs since it is closely related to the compatibility with Li metal. Thus, we will mainly focus on halide SSEs with metal components (Li_aMX_b , $M = \text{metal element}$, $X = \text{F}, \text{Cl}, \text{Br}, \text{I}$) as shown in Figure 2a. Based on the different types of metal elements, halide SSEs can generally be divided into three categories, i.e., 1) Li_aMX_b halide SSEs with group 3 elements ($M = \text{Sc}, \text{Y}, \text{La-Lu}$), 2) Li_aMX_b halide SSEs with group 13 elements ($M = \text{Al}, \text{Ga}, \text{In}$), and 3) Li_aMX_b halide SSEs with divalent metal elements ($M = \text{Ti}, \text{V}, \text{Cr}, \text{Mn}, \text{Fe}, \text{Co}, \text{Ni}, \text{Cu}, \text{Zn}, \text{Cd}, \text{Mg}, \text{Pb}$). The ionic conductivity evolution and ionic conductivities of several representative halide SSEs are presented in Figure 2b. As a supplement, we will also discuss nonmetal counterparts in the end of this section.

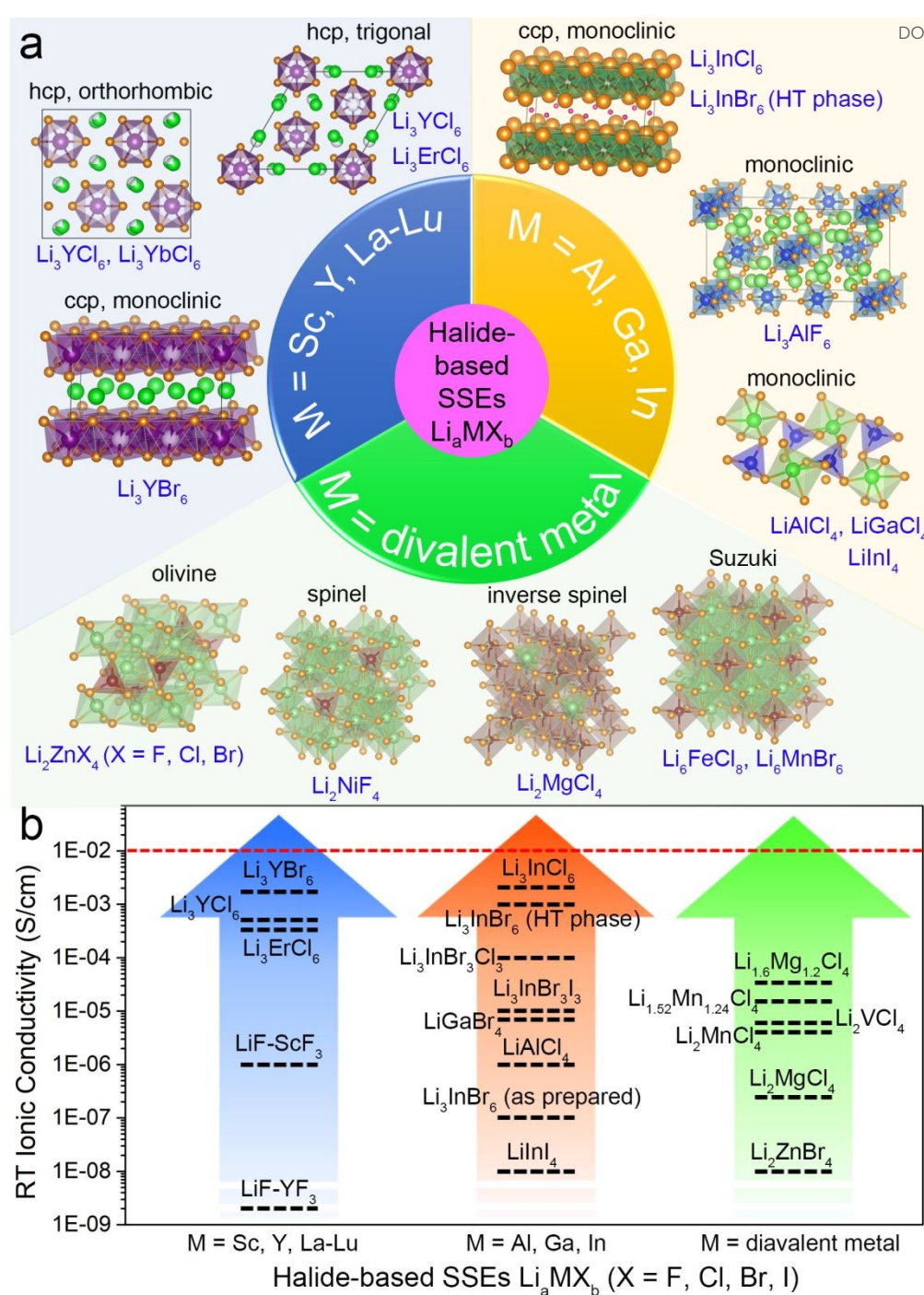


Figure 2. (a) Categories of existing halide Li_aMX_b (M = metal element, X = F, Cl, Br, I) SSEs. (b) Summary of the reported RT ionic conductivities of representative SSEs.^{14-16, 33, 37, 40, 42, 43, 48-55}

2.1 Halide SSEs with group 3 elements (Sc, Y, La-Lu)

Table 1. Radii of M^{3+} cations ($M = \text{Sc, Y, La-Lu}$)⁵⁶ and reported crystal compounds of Li-M-X ($X = \text{F, Cl, Br, I}$).

Group 3 elements	Radius (M^{3+} , pm)	Li-M-F	Li-M-Cl	Li-M-Br	Li-M-I	Ref.
Sc	74.5	LiScF_4 , Li_3ScF_6 (hcp)	Li_3ScCl_6 ccp (C2/m)	Li_3ScBr_6 ccp (C2/m)	LiScI_3	57-60
Y	90	LiYF_4	Li_3YCl_6 , hcp (P-3m1 or Pnma)	Li_3YBr_6 , ccp (C2/m)	-	14, 58, 59, 61, 62
La	103.2	-	-	-	-	
Ce	102	LiCeF_5 , Li_4CeF_8 , $\text{LiCe}_4\text{F}_{17}$, $\text{Li}_{5.5}\text{Ce}_{12}\text{F}_{50}$	-	-	-	63
Pr	99	Li_2PrF_6	-	-	-	64
Nd	98.3	-	-	-	-	
Pm	97	-	-	-	-	
Sm	95.8	-	-	Li_3SmBr_6 , ccp (C2/m)	-	62
Eu	94.7	LiEuF_4	-	Li_3EuBr_6 , ccp (C2/m)	-	62, 65
Gd	93.8	LiGdF_4	LiGdCl_4 , $\text{Li}_{0.23}\text{GdCl}$, LiGd_2Cl_2 ,	Li_3GdBr_6 , ccp (C2/m)	-	62, 66-68
Tb	92.3	LiTbF_4 , Li_2TbF_6 , Li_4TbF_8	Li_3TbCl_6 , hcp (P-3m1)	Li_3TbBr_6 , ccp (C2/m)	-	59, 62, 65, 69, 70
Dy	91.2	LiDyF_4	Li_3DyCl_6 , hcp (P-3m1)	Li_3DyBr_6 , ccp (C2/m)	-	59, 62, 65
Ho	90.1	LiHoF_4	Li_3HoCl_6 , hcp (P-3m1)	Li_3HoBr_6 , ccp (C2/m)	-	59, 62, 65
Er	89	LiErF_4	Li_3ErCl_6 , hcp (P-3m1)	Li_3ErBr_6 , ccp (C2/m)	Li_3ErI_6 , ccp (C2/c)	46, 59, 62, 71
Tm	88	LiTmF_4	Li_3TmCl_6 , hcp (P-3m1)	Li_3TmBr_6 , ccp (C2/m)	-	59, 62, 65
Yb	86.8	LiYbF_4	Li_3YbCl_6 , hcp (Pnma)	Li_3YbBr_6 , ccp (C2/m)	-	59, 62, 72
Lu	86.1	LiLuF_4	Li_3LuCl_6 , hcp (Pnma)	Li_3LuBr_6 , ccp (C2/m)	-	59, 62, 65

All the experimentally reported crystal compounds of Li-M-X with M for group 3 elements are listed in Table 1. It can be seen that the most obtained compounds are with the composition of LiMF_4 , Li_3MCl_6 , and Li_3MBr_6 . Due to the relative small radius of F^- (133 pm),⁵⁶ most of the reported fluoride halides are in the form of LiMF_4 (LiScF_4 ,⁵⁷ LiYF_4 ,⁵⁸ LiMF_4 ($\text{M} = \text{La-Lu}$)^{65, 66, 71, 72}) unless the existence of Li_3ScF_6 ,^{57, 73} which should be related to the smallest radius of Sc^{3+} as listed in Table 1. Some of the ionic conductivities of these fluoride-based SSEs have been reported, such as $1.4 \times 10^{-6} \text{ S cm}^{-1}$ at 200 °C for tetragonal (I41/a) LiYbF_4 .⁷² However, the contribution of ion migration might be caused by both Li^+ and F^- .^{72, 74, 75} Other fluorides that show higher room-temperature ionic conductivities such as LiF-YF_3 ($2 \times 10^{-9} \text{ S cm}^{-1}$),⁴⁸ and LiF-ScF_3 ($\sim 10^{-6} \text{ S cm}^{-1}$)³⁷ amorphous thin films have been obtained by thermal evaporation. It is supposed that the high ionic conductivity is attributed to the formation of amorphous intermediate phases with high coordination numbers for lithium.^{37, 48}

In the chloride-based ternary halides of the Li_3MCl_6 , there are mainly three kinds of structures. The first one is trigonal (P-3m1) structure, including Li_3MCl_6 ($\text{M} = \text{Y, Tb-Tm}$).^{59, 76} The second one is the orthorhombic (Pnma) structure, including Li_3MCl_6 ($\text{M} = \text{Y, Yb, and Lu}$).^{59, 61} The third one is the monoclinic (C2/m) structure, including Li_3ScCl_6 .⁵⁹ In contrast, all the bromide-based ternary halides of Li_3MBr_6 show the monoclinic structure.⁶² The trigonal and orthorhombic structures are based on the hexagonal close-packed (hcp) anion arrangement, while the monoclinic structure is based on the cubic close-packed (ccp)-like anion arrangement. The lack of Li-M-Cl compounds for La-Eu (radii of M^{3+} in the range of 94.7-103.2 pm) and the Li-M-Br compounds for La-Pm (radii of M^{3+} in the range of 97-103.2 pm) might be due to the too large radius of those metal cations. While due to the lanthanide contraction effect, the ionic radii of the lanthanides gradually decrease along with the increase of the atomic number.⁷⁷ It can be concluded that ccp structure can only be formed for relatively larger anionic halides (such as bromide halides) or relatively smaller metal cations (such as Sc^{3+}). In 1997, Gerd Meyer et al. systematically synthesized a series of Li_3MCl_6 ($\text{M} = \text{Tb-Lu, Y, Sc}$)⁵⁹ and Li_3MBr_6 ($\text{M} = \text{Sm-Lu, Y}$)⁶² halides and studied the crystal structures as well as ionic motion. All of the powder

samples of the ternary halides were obtained by annealing the binary components at 400 °C within two weeks. The reported ionic conductivities of those Li_3MCl_6 and Li_3MBr_6 SSEs are relatively low ranging from 10^{-4} - 10^{-3} S cm^{-1} even at 300 °C.^{59, 61, 62} In contrast, LiScI_3 and Li_3ErI_6 are the only reported compounds among Li-M-I compounds.^{46, 60}

Table 2. Halide SSEs with group 3 elements (Sc, Y, La-Lu)

Material	Conductivity (S cm^{-1})	Structure	Ref.
LiYbF_4	1.4×10^{-6} at 200 °C ^a	Tetragonal, I41/a	72
LiF-YF_3	2×10^{-9} at 25 °C	Amorphous thin film	48
LiF-ScF_3	$\sim 10^{-6}$ at 25 °C	Amorphous thin film	37
Li_3YCl_6	$\sim 10^{-3}$ at 300 °C	Orthorhombic, (Pnma)	61
Li_3YCl_6	$\sim 10^{-3}$ at 300 °C	Trigonal, (P-3m1)	59
Li_3YCl_6	$0.03\text{-}0.51 \times 10^{-3}$ at 25 °C	Trigonal, (P-3m1)	14
Li_3YCl_6	14×10^{-3} at 27 °C (Calculated)	Trigonal, (P-3m1)	17
$\text{Li}_{2.5}\text{Y}_{0.5}\text{Zr}_{0.5}\text{Cl}_6$	1.4×10^{-3} at 25 °C	Orthorhombic, (Pnma)	45
$\text{Li}_{2.633}\text{Er}_{0.633}\text{Zr}_{0.367}\text{Cl}_6$	1.1×10^{-3} at 25 °C	Orthorhombic, (Pnma)	45
Li_3ErCl_6	$3.1\text{-}3.3 \times 10^{-4}$ (ball mill) $0.17\text{-}1 \times 10^{-4}$ (anneal) at 25 °C	Trigonal, (P-3m1)	43, 44
Li_3YbCl_6	$\sim 10^{-4}$ at 300 °C	Orthorhombic, (Pnma)	59
Li_3MBr_6 (M = Sm-Lu, Y)	$\sim 10^{-2}$ over 300 °C $< 10^{-7}$ at 25 °C	Monoclinic, (C2/m)	62
Li_3YBr_6	$0.72\text{-}1.7 \times 10^{-3}$ at 25 °C	Monoclinic, (C2/m)	14
Li_3YBr_6	2.2×10^{-3} at 27 °C (Calculated)	Monoclinic, (C2/m)	17
Li_3ErCl_6	3×10^{-3} at 25 °C (Calculated)	Trigonal, (P-3m1)	18
Li_3ScCl_6	29×10^{-3} at 25 °C (Calculated)	Trigonal, (P-3m1)	17
Li_3HoCl_6	21×10^{-3} at 25 °C (Calculated)	Trigonal, (P-3m1)	17
Li_3ScBr_6	1.4×10^{-3} at 25 °C (Calculated)	Monoclinic, (C2/m)	17
Li_3HoBr_6	3.8×10^{-3} at 25 °C (Calculated)	Monoclinic, (C2/m)	17
Li_3ErI_6	$3.9\text{-}6.5 \times 10^{-4}$ at 25 °C	Monoclinic, (C2/c)	46
Li_3ScI_6	$2\text{-}3 \times 10^{-5}$ at 27 °C (Calculated)	Monoclinic, (C2)	21
Li_3YI_6	$1.3\text{-}1.9 \times 10^{-4}$ at 27 °C (Calculated)	Monoclinic, (C2)	21
Li_3LaI_6	$0.99\text{-}1.23 \times 10^{-3}$ at 27 °C (Calculated)	Monoclinic, (C2)	21

a. The ionic transport can be attributed to Li^+ and/or F^- .

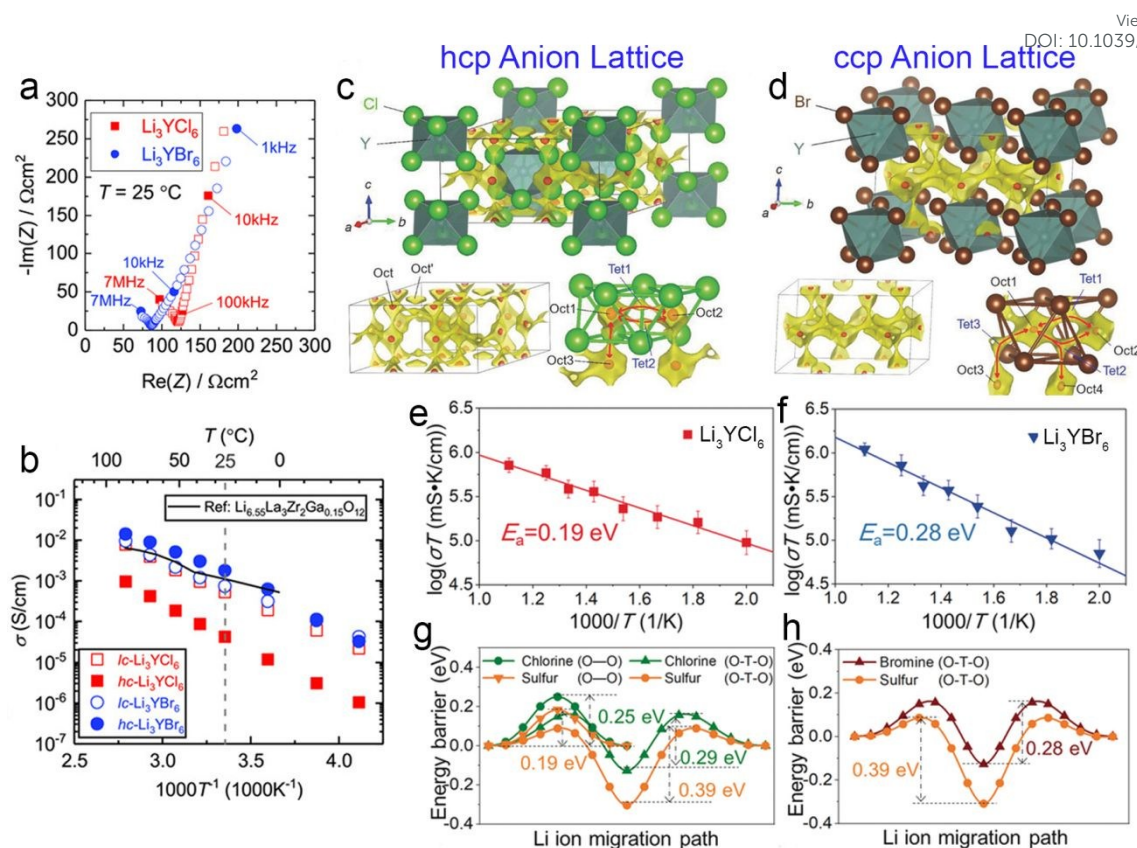


Figure 3. (a) The Nyquist plots of the EIS measurement results of Li_3YCl_6 and Li_3YBr_6 with nonreversible electrodes. (b) Arrhenius conductivity plots of Li_3YCl_6 and Li_3YBr_6 . The open symbols (labeled *lc*) are mechanochemically synthesized samples without heat treatment. The solid symbols (labeled *hc*) are measured after annealing, grinding into powders and then cold-pressing. (c,d) The crystal structures of Li_3YCl_6 and Li_3YBr_6 obtained after Rietveld refinement, superimposed with a calculated BVSE-based lithium-ion potential map. The yellow surface corresponds to the ionic conduction path, and the regions enclosed with red surfaces correspond to the stable lithium-ion positions. Reproduced with permission from ref. 14. Copyright (2018) Wiley. Arrhenius plot of Li^+ diffusivity in (e) Li_3YCl_6 and (f) Li_3YBr_6 from AIMD simulations. The energy landscape of single Li^+ migration in fixed (g) hcp and (h) fcc anion lattice at volume per anion of S^{2-} (LGPS: 40.0 \AA^3), Cl^- (Li_3YCl_6 : 37.4 \AA^3) and Br^- (Li_3YBr_6 : 44.8 \AA^3), respectively. Reproduced with permission from ref. 17. Copyright (2019) Wiley.

The big breakthrough of halide SSEs arrived in 2018 from the work of Tetsuya Asano et al.¹⁴

Li_3YCl_6 and Li_3YBr_6 with high RT ionic conductivities of $0.03\text{--}1.7 \times 10^{-3} \text{ S cm}^{-1}$ were successfully synthesized by a high-energy ball milling and high-temperature annealing process.¹⁴ The detailed ionic conductivities and structures of those reported halide SSEs with group 3 elements (La-Lu, Sc, Y) are listed in Table 2. The Li_3YCl_6 and Li_3YBr_6 SSEs synthesized by ball-milling for 50 h over 500 rpm exhibit lower crystallinity and ionic conductivities of 0.51×10^{-3} and $0.72 \times 10^{-3} \text{ S cm}^{-1}$ at 25°C (Figure 3a), respectively. Further annealing of these electrolytes to increase the crystallinity leads to significantly different effects on the ionic conductivity. The Li_3YCl_6 SSE after annealing showed reduced ionic conductivity to $0.03 \times 10^{-3} \text{ S cm}^{-1}$, while the value of Li_3YBr_6 SSE can be greatly improved to $1.7 \times 10^{-3} \text{ S cm}^{-1}$ after the annealing process (Figure 3b). The structures of Li_3YCl_6 and Li_3YBr_6 synthesized by Tetsuya Asano et al. are consistent with those obtained by Gerd Meyer et al., which possesses a trigonal (space group of $P\text{-}3m1$) structure with hcp anion sublattice and monoclinic (space group of $C2/m$) with ccp anion sublattice, respectively, as shown in Figure 3c. The significantly improved ionic conductivity for Li_3YCl_6 compared to that obtained by Gerd Meyer et al. is probably due to the different synthesis routes. In both Li_3YCl_6 and Li_3YBr_6 SSEs, both the Y^{3+} and Li^+ cations are located at the octahedral (Oct) sites with halogen anions (Cl^- or Br^-). It should be noted that due to the 3^+ valence state of Y^{3+} compared to that of 1^+ of Li^+ and 1^- for Cl^- or Br^- , the presence of Y^{3+} would involve two intrinsic vacancies, which means that the Oct sites are actually occupied by Li^+ , Y^{3+} , and vacancies with molar ratio of 3:1:2. The intrinsic vacancies within Li_3YCl_6 and Li_3YBr_6 are believed to be essential to their high ionic conductivity.¹⁷

The Li^+ migration pathways in Li_3YCl_6 and Li_3YBr_6 SSEs were simulated both by bond valence site energy (BVSE, Tetsuya Asano, et al.)¹⁴ and ab initio molecular dynamics (AIMD, Yifei Mo, et al.) methods¹⁷ as presented in Figure 3c,d. For Li_3YCl_6 with a hcp-like anion sublattice, the Li^+ migrate through adjacent face-sharing Oct sites directly along the c-axis (Oct-Oct), forming one-dimension (1 D) diffusion channels with fast diffusivity; while Li^+ has to migrate through additional tetrahedral (Tet) interstitial sites between two Oct sites among ab-planes (Oct-Tet-Oct), corresponding

to a slower diffusivity as shown in Figure 3c. For Li_3YBr_6 with a ccp-like anion sublattice, the Li^+ migration in all three directions is similar, with Li^+ migrate via a Tet interstitial site between two Oct sites in all three directions (Oct-Tet-Oct in Figure 3d). From this point of view, the Li_3YCl_6 should possess higher ionic conductivity than Li_3YBr_6 as calculated by AIMD simulations, corresponding to 14×10^{-3} and $2.2 \times 10^{-3} \text{ S cm}^{-1}$ respectively at 25°C (Table 2). Furthermore, the calculated activation energy (E_a) of Li_3YCl_6 is $0.19 \pm 0.03 \text{ eV}$, which is much lower than that of $0.28 \pm 0.02 \text{ eV}$ for Li_3YBr_6 (Figure 3g,h). It can be seen that there's a relatively larger difference between the simulation and experimental results for Li_3YCl_6 , especially the experimental reported ionic conductivity value ($0.51 \times 10^{-3} \text{ S cm}^{-1}$).

The discrepancy of ionic conductivity for Li_3YCl_6 can be explained by the channel-blocking defects: (1) anti-site defect caused by the disordering of Y^{3+} and Li^+ in the Oct sites considering the similar ionic radius ($r_{\text{Y}^{3+}} = 90 \text{ pm}$, $r_{\text{Li}^+} = 76 \text{ pm}$),⁵⁶ the Li^+ would be discontinuous and blocked by the repulsive interaction between Y^{3+} and Li^+ during migration; (2) other effects such as impurities, grain boundaries, and partial amorphization formed during the synthesis process. It is possible that the experimentally reported ionic conductivity can be further improved by sintering pellets rather than cold-pressing pellets, which is the case for sulfide SSEs, since all the reported sulfide-based SSEs with ionic conductivity over $10^{-2} \text{ S cm}^{-1}$ are sintered to decrease the influence of the grain boundaries.^{4, 5, 13, 78} They also predicted four other promising halide SSEs of Li_3ScCl_6 , Li_3HoCl_6 , Li_3ScBr_6 , and Li_3HoBr_6 . The calculated ionic conductivity can be as high as 1.4×10^{-3} to $29 \times 10^{-3} \text{ S cm}^{-1}$ as presented in Table 2. However, their calculation is based on hcp- Li_3ScCl_6 , which is totally different from the real monoclinic (C2/m) structure of Li_3ScCl_6 .^{17, 59}

Yifei Mo et al. further calculated the energy landscape of one Li^+ migration pathway in the fixed hcp and ccp anion sublattice of Cl^- , Br^- , and S^{2-} with no other cations present to directly evaluate the effect of the anion configuration (Figure 3f,g). The migration barrier of Li^+ in hcp and ccp anion sublattice of Cl^- and Br^- is ranging from 0.25 - 0.29 eV , which is much lower compared to that of 0.39

eV in S^{2-} anion sublattice. Moreover, as mentioned above, in the typical halide SSEs containing group 3 elements (Li_3MX_6), which can also be written as $Li_3MV_2X_6$, the theoretical intrinsic vacancy content is as high as 33% within the Oct sites. It is believed the much higher content of vacancies is another essential parameter to further boost fast Li^+ migration within the SSEs.^{79, 80} These two intrinsic properties of halide SSEs with group 3 elements (Li_3MX_6) enable high ionic conductivity though their relatively low symmetry (orthorhombic, trigonal, monoclinic) lattice structures and Li^+ occupation in Oct sites compared to the favored Tet sites in sulfide-based SSEs.⁸¹

Another type halide SSE, Li_3ErCl_6 with trigonal structure (space group P-3m1), was predicted to show a high ionic conductivity of $3 \times 10^{-3} \text{ S cm}^{-1}$ through a guided search model for material selection and density functional theory molecular dynamics simulations by Evan J. Reed et al. in 2018.¹⁸ The high ionic conductivity of Li_3ErCl_6 was further predicted by Sokseiha Muy et al. by high-throughput screening in the Materials Project database using a descriptor based on lattice dynamic.⁴³ The Li_3ErCl_6 SSE synthesized through ball-milling and annealing strategies shows 3×10^{-4} and $5 \times 10^{-5} \text{ S cm}^{-1}$ respectively at 25 °C.⁴³ As mentioned above, the structures of Li_3ErCl_6 and Li_3YCl_6 SSEs are the same. Furthermore, similar to the reported Li_3YCl_6 SSE,¹⁴ the ionic conductivity of Li_3ErCl_6 SSEs is reduced with increasing crystallinity during the subsequent annealing process, the difference should be related to the local structural features especially the site disorder effect⁴⁴. For these two trigonal Li_3ErCl_6 and Li_3YCl_6 SSEs, it was proved that substitution of Er^{3+} or Y^{3+} by Zr^{4+} can convert the trigonal structure to orthorhombic structure and triggered higher ionic conductivity up to $1.4 \times 10^{-3} \text{ S cm}^{-1}$.⁴⁵ It was supposed that the newly formed lithium sites and vacancies played key roles for the enhanced Li^+ conductivity. In addition, as presented in Table 2, though several iodide-type Li_3MI_6 compounds were predicted to show fast Li^+ migration, it's not until quite recently that Li_3ErI_6 with ionic conductivity of $3.9\text{-}6.5 \times 10^{-4} \text{ S cm}^{-1}$ was synthesized successfully by Wolfgang G. Zeier et al.⁴⁶

2.2 Halide SSEs with group 13 elements (Al, Ga, In)

The halide SSEs containing group 13 elements (Al, Ga, In) were initially developed in the 1970s, such as the typical LiAlCl_4 with RT ionic conductivity of $1 \times 10^{-6} \text{ S cm}^{-1}$.^{33, 34} Due to the relatively smaller ionic radius of Al^{3+} ($r_{\text{Al}^{3+}} = 53.5 \text{ pm}$) and Ga^{3+} ($r_{\text{Ga}^{3+}} = 62 \text{ pm}$) compared to that of In^{3+} ($r_{\text{In}^{3+}} = 80 \text{ pm}$) and other group 3 elements (74.5-103.2 pm), Al^{3+} and Ga^{3+} cations can only form low-coordinate structures with larger halide anions, such as LiAlCl_4 ^{33, 34}, LiGaCl_4 ⁸², LiGaCl_3 ⁸³, LiGaBr_4 ^{53, 84}, LiGaI_4 ⁸², LiGaI_3 ⁸³; higher six-coordination complexes can only be formed in smaller F⁻ anions ($r_{\text{F}^-} = 133 \text{ pm}$) for Al^{3+} and Ga^{3+} to form Li_3AlF_6 ^{85, 86}, Li_3GaF_6 ⁸⁷. In contrast, In^{3+} with ionic radius of 80 pm can form six-coordinated compounds with F⁻, Cl⁻ and Br⁻ ($r_{\text{Cl}^-} = 181 \text{ pm}$, $r_{\text{Br}^-} = 196 \text{ pm}$), such as Li_3InF_6 , Li_3InCl_6 ^{15, 16, 61}, Li_3InBr_6 ⁵³, while In^{3+} can only form four-coordinated LiInI_4 ⁵² due to the large radius of I⁻ ($r_{\text{I}^-} = 220 \text{ pm}$). Most of the aforementioned crystalline halide SSEs show a relatively low RT ionic conductivity around $10^{-6} \text{ S cm}^{-1}$ as shown in Table 3.

The applicability of fluoride-based halide SSEs has not been studied as extensively as chlorides and bromides. A typical example is the Li-Al-F system that can be found in the literature. Li_3AlF_6 , with orthorhombic structure (space group Pna21), has been reported to show an ionic conductivity of $\sim 10^{-6} \text{ S cm}^{-1}$ at 200 °C.³⁸ However, the ionic conductivity can be dramatically increased up to $2 \times 10^{-6} \text{ S cm}^{-1}$ at 200 °C by mechanically milling Li_3AlF_6 with LiCl in the form of $3\text{Li}_3\text{AlF}_6 \cdot \text{LiCl}$.⁸⁸ In addition, similar to the amorphous LiF-ScF₃ thin film mentioned above, the amorphous LiF-AlF₃ thin film grown by thermal evaporation with a nearly stoichiometric LiAlF₄ composition also shows higher RT ionic conductivity of $10^{-6} \text{ S cm}^{-1}$.^{36, 37} However, it should also be noted that the high ionic conductivity is not caused by pure Li⁺ migration, protons might be also involved for amorphous LiF-AlF₃.³⁶ In addition, the ionic conductivity of the LiF-AlF₃ thin film is highly depended on the synthesis method and composition. The reported LiF-AlF₃ alloy film with approximate atomic ratios of Li:Al:F=2.7:1:5.4 prepared by atomic layer deposition (ALD) was measured to $7.5 \times 10^{-6} \text{ S cm}^{-1}$.⁸⁹

Table 3. Halide SSEs with group 13 elements (Al, Ga, In).

Material	Conductivity (S cm^{-1})	Structure	Ref.
----------	-------------------------------------	-----------	------

α -Li ₃ AlF ₆	$\sim 10^{-6}$ at 200 °C	Orthorhombic, (Pna21)	38
β -Li ₃ AlF ₆	3.9×10^{-6} at 100 °C	Monoclinic, (C2/c)	90
β -Li ₃ AlF ₆ /γ-Al ₂ O ₃	1.8×10^{-5} at 100 °C		90
LiAlF ₄	1×10^{-6} at 25 °C ^a	Amorphous thin film	36, 37, 48
Li _{2.7} AlF _{5.4}	7.5×10^{-6} at 25 °C	Amorphous	89
LiAlCl ₄	1×10^{-6} at 25 °C	Monoclinic, (P21/c)	33, 34
LiGaBr ₄	7×10^{-6} (24 °C)	Monoclinic, (P21/a)	53
Li ₃ InCl ₆	$\sim 10^{-4}$ at 100 °C 0.2 at 300 °C	Monoclinic, (C2/m)	61
Li ₃ InCl ₆	0.84 - 1.49×10^{-3} at 25 °C	Monoclinic, (C2/m)	15
Li ₃ InCl ₆	2.04×10^{-3} at 25 °C	Monoclinic, (C2/m)	16
Li ₃ InCl ₆	6.4×10^{-3} at 25 °C (Calculated)		18, 20
LiInBr ₄ (HT phase)	1×10^{-3} at 25 °C	Defect cubic spinel structure, (Fd3m)	91
Li ₃ InBr ₆ (HT phase)	1×10^{-3} at 25 °C	Monoclinic, (C2/m)	42, 53, 91-93
Li ₃ InBr _{6-x} Cl _x with $x \leq 4$	1.2×10^{-4} at 27 °C	phase transition at 12 °C	50
Li ₃ InBr _{6-y} X _y (X=F, I)	3×10^{-3} at 60 °C for Li ₃ InBr ₃ I ₃ , Others $< 10^{-5}$ at 25 °C	phase transition at 60 °C	51
Li _{3-2x} Mg _x InBr ₆ (x=0.02-0.4)	$< 10^{-5}$ at 25 °C	phase transition at ~ 37 -57 °C	94
Li _{3-2x} M _x InBr ₆ (M=Mg, Ca, Sr, Ba; x=0-1.0)	2×10^{-5} at 25 °C for Li ₂ Ba _{0.5} InBr ₆ , Others $< 10^{-5}$ at 25 °C	phase transition at ~ 37 -57 °C for Mg or Sc compounds, ~ 111 °C for Ca compound	49
LiInI ₄	$\sim 10^{-8}$ (25 °C)	Monoclinic, (P21/c)	52

a. The ionic transport can be attributed to Li⁺ and/or protons.

The most studied halide SSE system is Li₃InBr₆,^{20, 42, 49-51, 53, 91-93, 95, 96} which was firstly reported by Koji Yamada et al. in 1998.⁴² However, the high conductivity in Li₃InBr₆ can only be achieved with the relatively high-temperature phase (HT phase).^{42, 92, 94} The pristine synthesized Li₃InBr₆ is almost an ionic insulator with a low RT ionic conductivity of 10^{-7} S cm⁻¹ (Figure 4a).⁴² Li₃InBr₆ undergoes a phase transition to a superionic conductor at 314 K (41 °C) revealed by differential scanning

calorimetry (DSC) analysis (Figure 4b), leading to an obvious sharp increase of ionic conductivity (Figure 4a). Furthermore, it seems that the HT phase is relatively stable when cooled down to room temperature, and ionic conductivity could still be as high as to $1 \times 10^{-3} \text{ S cm}^{-1}$ when decreasing to 27°C (Figure 4a).⁹⁴ The HT phase of Li_3InBr_6 exhibits a distorted rock-salt LiBr structure belonging to the monoclinic system (C2/m), which is quite similar to reported structure for Li_3YBr_6 ¹⁴ and Li_3InCl_6 ^{15, 16}. The similar structures suggest that larger cations such as In^{3+} and other trivalent cations (La-Lu, Sc, Y) are a good choice for introducing vacancies into halide SSEs. Brandon C. Wood et al. proposed that in addition to the contribution of intrinsic vacancies, the frustration of chemical environment due to the polarizable anions also contribute to the high ionic conductivity of HT Li_3InBr_6 (Figure 4c).⁹⁷ These findings can be mainly attributed to two factors: one is the disordered effect due to the existence of mixed ionic-covalent character facilitated by the high polarizability and relatively low electronegativity of the anion (Figure 4c2), the other one is the flattened energy landscape caused by the bond frustration and lattice incompatibility between ionic and covalent preferences (Figure 4c3).

Due to the significance of vacancies, some bivalent cations such as Mg^{2+} , Ca^{2+} , Sr^{2+} , and Ba^{2+} were introduced to replace some Li^+ to further improve the vacancy content to promote ionic conductivity.^{42, 49, 94} Nonetheless, the ionic conductivities were actually not improved (Figure 4a). This should be due to the reduced Li^+ content even though the vacancy content is higher. Other anions such as F^- , Cl^- , and I^- were also introduced into Li_3InBr_6 to modify the ionic conductivity and stabilize the structure.^{51, 95} However, there's still a phase transition for those substituted SSEs around room temperature, making them unsuitable for practical application. In addition to Li_3InBr_6 SSE, another LiInBr_4 was also proposed as a fast Li^+ conductor in Li-In-Br system.⁹¹ The properties of LiInBr_4 are similar to Li_3InBr_6 . The as-synthesized LiInBr_4 is also a poor Li^+ conductor, with a quite low ionic conductivity of $10^{-6} \text{ S cm}^{-1}$ at 300 K (27°C , Figure 4a). During the heating process, LiInBr_4 will convert to a high-temperature superionic phase (HT phase) at 316 K (43°C , Figure 4b). The HT phase can be retained during the cooling process, possessing an ionic conductivity of $10^{-3} \text{ S cm}^{-1}$ at 27°C . Again,

the high-temperature phase will be damaged at $-13\text{ }^{\circ}\text{C}$. The structure of HT-phase LiInBr_4 is a defect cubic spinel structure, which is totally different from that of Li_3InBr_6 .⁹¹

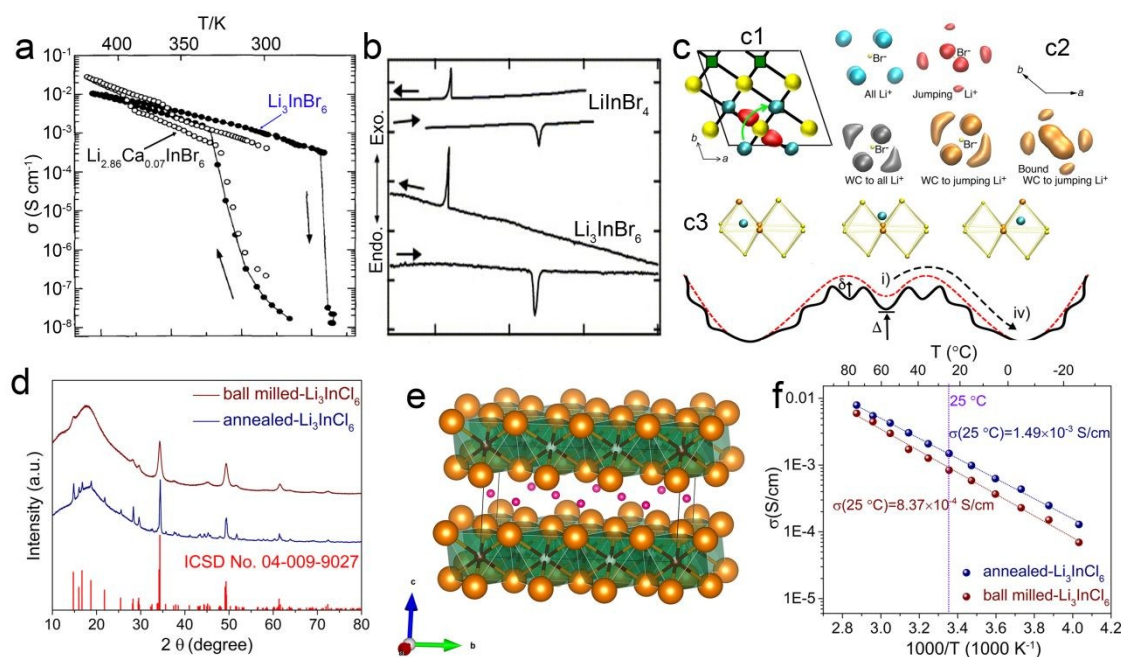


Figure 4. (a) Temperature dependence of ionic conductivity of Li_3InBr_6 (solid circle) and $\text{Li}_{2.86}\text{Ca}_{0.07}\text{InBr}_6$ (open circle). Reproduced with permission from ref. 42. Copyright (1998) Chemical Society of Japan. (b) DCS curves for Li_3InBr_6 and LiInBr_4 . Reproduced with permission from ref. 91. Copyright (2006) Elsevier. (c) Dynamically frustrated bond disorder in HT Li_3InBr_6 . (c1) Top view of HT Li_3InBr_6 and atomic density isosurfaces of Li^+ occupying octahedral sites (blue), interstitial tetrahedral sites (red), and Li^+ pathway (green arrow). (c2) Isosurfaces within HT Li_3InBr_6 . (c3) Polar-covalent effect on diffusion and frustration together with the energy landscape associated with jumping between octahedral sites through the metastable tetrahedral site. Reproduced with permission from ref. 97. Copyright (2016) American Chemical Society. (d) XRD patterns of the ball-milled and annealed Li_3InCl_6 samples, along with the standard pattern of the previously reported Li_3InCl_6 (ICSD No. 04-009-9027). (e) Structure of annealed- Li_3InCl_6 , showing two kinds of InCl_6^{3-} octahedra with the different occupations of In^{3+} (red wine) and vacancies (V'' , white); orange balls are Cl^- . (f) Arrhenius plots of ball-milled and annealed Li_3InCl_6 samples. Reproduced with permission from ref. 15. Copyright (2019) Royal Society of Chemistry.

Li_3InCl_6 is another promising halide SSE among this group. H. D. Lutz et al. synthesized Li_3InCl_6 SSE by melting together the anhydrous LiCl and InCl_3 in evacuated glass ampoules at 500–600 °C, and then slowly cooling down to room temperature at 2–10 °C h⁻¹ in 1992.⁶¹ Though it has a relatively low ionic conductivity of $\sim 10^{-5}$ S cm⁻¹ at 25 °C, the predicted RT ionic conductivity can be as high as 6.4×10^{-3} S cm⁻¹.^{18, 20} Furthermore, the phase transition temperature of Li_3InCl_6 is reported to be between 200 to 300 °C, which will have less influence on its application compared to Li_3InBr_6 .^{42, 61} Different from the synthesis method of H. D. Lutz, our group prepared Li_3InCl_6 SSE through ball-milling or followed by further annealing at relatively low temperature at 260 °C. The Li_3InCl_6 SSE synthesized by ball-milling approach exhibited relatively low crystallinity, while still can be indexed to Li_3InCl_6 with monoclinic structure, and the Li_3InCl_6 SSE synthesized by annealing approach presented high crystallinity (Figure 4d). Same as Li_3YBr_6 and HT Li_3InBr_6 , monoclinic Li_3InCl_6 is also a distorted LiCl structure as presented in Figure 4e, with Li^+ , In^{3+} , and vacancy located in the octahedron formed by Cl^- anions. In^{3+} and vacancy co-occupied in the octahedral sites 4g and 2a sites with different ratios. The ball-milled and annealed Li_3InCl_6 SSE can show RT high ionic conductivities of 0.84×10^{-3} and 1.49×10^{-3} S cm⁻¹ (Figure 4f).¹⁵ The much lower annealing temperature demonstrated its facile crystallization to achieve high ionic conductivity and is also more energy sustainable compared to that of 550 °C for the synthesis of $\text{Li}_3\text{YCl}_6/\text{Li}_3\text{YBr}_6$ ¹⁴ or Li_3ErCl_6 .⁴³

Recently, our group further synthesized Li_3InCl_6 SSE through a water-mediated approach, which can show a high RT ionic conductivity of 2.04×10^{-3} S cm⁻¹.¹⁶ In short, $\text{Li}_3\text{InCl}_6 \cdot 2\text{H}_2\text{O}$ intermediates can be formed by dissolving LiCl and InCl_3 into water, final Li_3InCl_6 can be obtained by the dehydration of the $\text{Li}_3\text{InCl}_6 \cdot 2\text{H}_2\text{O}$. The detailed synthesis process will be discussed in the following part. The water-mediated synthesized Li_3InCl_6 SSE still showed monoclinic structure, while it is slightly different from that of the database. Furthermore, it is demonstrated that the reversible conversion between Li_3InCl_6 and its hydrated form of $\text{Li}_3\text{InCl}_6 \cdot 2\text{H}_2\text{O}$ can ensure the recoverable

structure and ionic conductivity after exposed to humid air, which is quite different from that in the previous reports.²

As a short summary, Li_3MX_6 SSEs with trivalent metal elements ($74.5 \leq r_{\text{M}^{3+}} \leq 103.2$ pm) fulfill several requirements regarding to Li^+ conductive property: 1) small mobile Li^+ cations ($r_{\text{Li}^+} = 76$ pm); 2) energetically equivalent vacancy sites that available for the mobile Li^+ ; 3) statistic and uniform distribution of Li^+ cations within the octahedral sites; 4) pathways for the Li^+ cations with low energy barriers through the crystal structures based on hcp or ccp of anions.

2.3 Halide SSEs with divalent metal elements (Ti, V, Cr, Mn, Fe, Co, Ni, Cu, Zn, Cd, Mg, Pb)

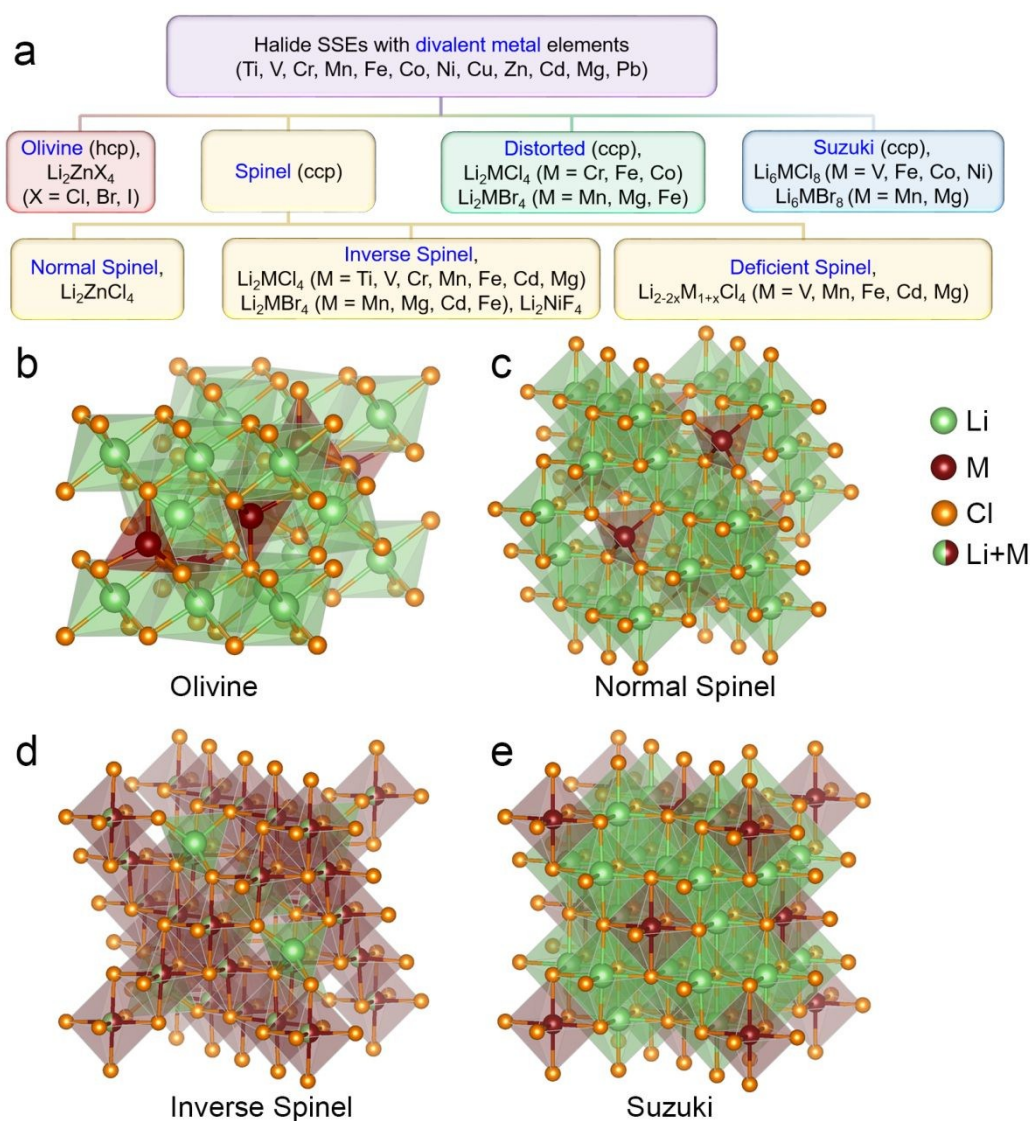


Figure 5. (a) Different structures of halide SSEs with divalent metal elements, (b) olivine type of Li_2MCl_4 , (c) Normal spinel type of Li_2MCl_4 , (d) Inverse spinel type of Li_2MCl_4 , and (e) Suzuki type Li_6MCl_8 .

The halide SSEs with divalent metal elements (Ti, V, Cr, Mn, Fe, Co, Ni, Cu, Zn, Cd, Mg, Pb) are mostly reported by Ryoji Kanno et al. and H. D. Lutz et al. These halide SSEs can generally be divided into four types based on structure, i.e., olivine structure, spinel structure (normal spinel, inverse spinel, deficient spinel), distorted structure, and Suzuki phases (Li_6MX_8 (V, Fe, Co, Ni, Mn, Mg), rock salt) structure (Figure 5a). Some typical structures are presented in Figure 5b-e, while the distorted structure is not shown here due to the complexity.

2.3.1 Olivine structure

Among the four structures, olivine structure (orthorhombic, Pnma) is the only one based on a hcp of X^- anions, and can be obtained in zinc (Zn) based Li_2ZnX_4 ($\text{X} = \text{Cl}, \text{Br}, \text{I}$) SSEs.^{54, 98, 99} All the Li^+ ions are located in the octahedral sites and Zn^{2+} ions in the tetrahedral sites (Figure 5b). It should be noted that Li_2ZnCl_4 with olivine structure is actually a high-temperature structure, by heating room-temperature normal spinel Li_2ZnCl_4 to 215 °C.⁹⁸

2.3.2 Spinel structure

Spinel has been found to possess a framework structure based on a ccp structure of X^- anions, which is suitable for high ionic conduction of Li_2MX_4 ($\text{X} = \text{Cl}, \text{Br}$) halide SSEs. Most chloride and bromide type halide SSEs belong to the spinel structure family. There are mainly three types of spinels among the halide SSEs. The first one is a normal spinel structure with all the Li^+ located in octahedral sites (surrounded by six halide ions) as presented in Figure 5c. The second one is the inverse spinel structure (Figure 5d), with half of the Li^+ located in tetrahedral sites (surrounded by four halide ions), and the other half of Li^+ , together with the divalent cations, are located in octahedral sites statistically. The third one is deficient inverse spinel-type solid solution $\text{Li}_{2-2x}\text{M}_{1+x}\text{Cl}_4$ ($\text{M} = \text{V}, \text{Mn}, \text{Fe}, \text{Cd}, \text{Mg}$) SSEs.

Low temperature Li_2ZnCl_4 is one of the typical halide SSEs with a normal spinel structure (space group of Fd-3m).^{100, 101} H. D. Lutz et al. successfully proved that all Li^+ are located solely in octahedral sites for spinel type Li_2ZnCl_4 , which is similar to the olivine-type Li_2ZnCl_4 .¹⁰¹ Comparatively, lots of other Li_2MCl_4 ($\text{M} = \text{Mg}, \text{Mn}, \text{Fe}, \text{Cd}, \text{V}, \text{Cr}, \text{Ti}$), and Li_2MBr_4 ($\text{Mg}, \text{Mn}, \text{Cd}, \text{Fe}$, some are high-temperature structure) halide SSEs have been determined to have the inverse spinel structure (space group of Fd-3m), with Li^+ located in both tetrahedral and octahedral sites, and the distribution of Li^+ and M^{2+} cations in octahedral sites are disordered.^{101, 102} The distribution of this structure can be described as $(\text{Li})_{\text{tet}}(\text{LiM})_{\text{oct}}\text{X}_4$.

It's believed that Li^+ transport occurs via the shared faces of octahedra and tetrahedra within those spinel structures, and the Li^+ on the tetrahedral sites play a predominant role for high ionic conductivity. Thus, the ionic conductivity of normal spinel Li_2ZnCl_4 with Li^+ only occupied in octahedral sites is relatively low. Moreover, the migration of Li^+ through tetrahedral interstitial sites is repulsive due to the closely situated tetrahedral Zn sites. In contrast, much higher ionic conductivity can be achieved for the inverse spinel type halide SSEs with Li^+ located both in tetrahedral and octahedral sites as shown in Table 4.

Table 4. Halide SSEs with divalent metal elements (Ti, V, Cr, Mn, Fe, Co, Ni, Cu, Zn, Cd, Mg, Pb)

Material	Conductivity (S cm^{-1})	Structure	Ref.
Li_2TiF_6	2×10^{-4} at 300 °C ^a	trirutile type, tetragonal	38
Li_2NiF_4	1.1×10^{-8} at 200 °C, 6.2×10^{-6} at 360 °C	Inverse spinel	103
LiF-MF ₂ thin film (Mg, Ca, Ti, Ni, Cu, Zn, Sr)	10^{-13} to 10^{-6} at 25 °C	amorphous	48
Li_2TiCl_4	$\sim 5 \times 10^{-3}$ at 300 °C, 5×10^{-2} at 400 °C	Inverse spinel	100
Li_2VCl_4	6×10^{-6} at 25 °C, 1.6×10^{-2} at 300 °C	Inverse spinel	55
Li_2CrCl_4	1.5×10^{-2} at 400 °C, 9×10^{-2} at 540 °C,	Distorted spinel	104
Li_2CrCl_4	6.3×10^{-2} at 400 °C	Distorted monoclinic structure	102
Li_2MnCl_4	4×10^{-6} at 25 °C, $\sim 5 \times 10^{-2}$ at 300 °C	Inverse spinel	55

Li_2MnCl_4	4×10^{-3} at 200 °C, $\sim 6 \times 10^{-2}$ at 300 °C	Inverse spinel	105
Li_2MnCl_4	5×10^{-2} at 300 °C	Inverse spinel	41
$\text{Li}_{1.6}\text{Mn}_{1.2}\text{Cl}_4$	0.4 at 300 °C	Deficient inverse spinel	106
$\text{Li}_{1.52}\text{Mn}_{1.24}\text{Cl}_4$	1.5×10^{-5} at 25 °C	Deficient inverse spinel	40
Li_2MnBr_4	2.2×10^{-2} at 300 °C, 8×10^{-2} at 400 °C	Inverse spinel	107
Li_2MnBr_4	7.3×10^{-2} at 400 °C	Distorted tetragonal structure	108
Li_2FeCl_4	1.9×10^{-3} at 200 °C, 6.3×10^{-2} at 400 °C	Distorted orthorhombic structure, Imma	105, 109
Li_6FeCl_8	2×10^{-3} at 200 °C, 5×10^{-2} at 400 °C	Suzuki structure, cubic	110
Li_6FeCl_8	2.2×10^{-4} at 200 °C, 4.5×10^{-2} at 400 °C	Suzuki structure, cubic	111
Li_2CoCl_4	$\sim 10^{-2}$ at 300 °C, 5×10^{-2} at 400 °C	Distorted orthorhombic structure	100
Li_6CoCl_8	$\sim 7 \times 10^{-4}$ at 200 °C, 9.3×10^{-2} at 400 °C	Suzuki structure, cubic	112
Li_6CoCl_8	6.2×10^{-5} at 200 °C, 7×10^{-2} at 400 °C	Suzuki structure, cubic	111
Li_6NiCl_8	4.9×10^{-6} at 200 °C, 1.3×10^{-2} at 400 °C	Suzuki structure, cubic	111
Li_2ZnCl_4	2×10^{-4} at 280 °C, 1×10^{-6} at 200 °C	Normal Spinel	100, 98
Li_2ZnCl_4	8×10^{-4} at 300 °C	Normal Spinel	113
Li_2ZnBr_4	$\sim 10^{-6}$ at 200 °C 5×10^{-4} at 300 °C	Olivine	54, 113
Li_2ZnI_4	3.5×10^{-3} at 247 °C	Olivine	113
Li_2CdCl_4	0.12 at 300 °C, 0.62 at 400 °C	Inverse spinel	41
Li_2CdCl_4	5.9×10^{-3} at 200 °C, 0.32 at 400 °C	Inverse spinel	105
$\text{Li}_{1.9}\text{Cd}_{1.05}\text{Cl}_4$	0.1 at 200 °C, 0.35 at 400 °C	Deficient inverse spinel	40, 105
Li_2CdBr_4	3×10^{-4} at 300 °C, 0.11 at 400 °C	Inverse spinel	107
Li_2CdI_4	0.1 at 297 °C	Deficient NaCl type	113
Li_2MgCl_4	$\sim 10^{-6}$ at 25 °C, $\sim 10^{-2}$ at 300 °C	Inverse spinel	55
$\text{Li}_{5/3}\text{Mg}_{7/6}\text{Cl}_4$	$\sim 10^{-5}$ at 25 °C, $\sim 10^{-2}$ at 300 °C	Deficient inverse spinel	55
Li_2MgCl_4	0.05 at 300 °C, 0.33 at 400 °C	Inverse spinel	41, 114
Li_2MgCl_4	4.5×10^{-3} at 200 °C, 0.14 at 400 °C	Inverse spinel	105
Li_2MgCl_4	2.4×10^{-7} at 25 °C	Inverse spinel	40
$\text{Li}_{1.6}\text{Mg}_{1.2}\text{Cl}_4$	3.4×10^{-5} at 25 °C	Deficient inverse spinel	40

View Article Online
DOI: 10.1039/C9EE03828K

Li_2MgBr_4	$\sim 2 \times 10^{-2}$ at 300 °C 4.5×10^{-2} at 400 °C	Distorted orthorhombic structure	108
Li_2MgBr_4	1.6×10^{-2} at 300 °C	Inverse spinel	113
Li_2PbI_4	3×10^{-2} at 297 °C	Deficient NaCl type	113
Li_4PbI_6	7×10^{-2} at 297 °C	Deficient NaCl type	113

a. The ionic transport can be partially attributed to electron. The valence of titanium is +4 in Li_2TiF_6 .

In addition to the stoichiometric chloride inverse spinels, deficient spinel-type solid solution $\text{Li}_{2-2x}\text{M}_{1+x}\text{Cl}_4$ ($\text{M} = \text{V}, \text{Mn}, \text{Fe}, \text{Cd}, \text{Mg}$) SSEs were also reported.^{39, 40, 105, 106, 115} In these structures, it was supposed that the vacancies would also be introduced theoretically by substitution of more M^{2+} cations to keep the charge neutrality. Furthermore, it was demonstrated that the extra vacancies that inducing by M^{2+} cations located in the tetrahedral sites within the structure. Thus, the deficient spinel-type $\text{Li}_{2-2x}\text{M}_{1+x}\text{Cl}_4$ can be further described as $(\text{Li}_{1-x}\text{V}_x)_{\text{tet}}(\text{Li}_{1-x}\text{M}_{1+x})_{\text{oct}}\text{Cl}_4$, where V" means vacancy. The full occupation of vacancies in tetrahedral sites was further proved by the structures of highly deficient spinel-type LiMgCl_3 and LiVCl_3 ($x = 1/3$)¹¹⁵.

In general, the deficient spinel-type $\text{Li}_{2-2x}\text{M}_{1+x}\text{Cl}_4$ SSEs exhibited higher ionic conductivity compared to their stoichiometric counterparts, as shown in Table 5. The significant increase in conductivity for the deficient spinels should be due to the presence of extra vacancies, which play a dominant role in ionic conductivity. Same as the above-mentioned Li_3MX_6 SSEs which possess intrinsic vacancies, the Li^+ migration within the close-packed anionic structures is more favored with the existence of vacancies. Nevertheless, the conductivity does not increase linearly along with the increasing of x value, and too much substitution of M^{2+} cations leads to a lower concentration of Li^+ within the structures, which in turn induce lower ionic conductivity. Thus, there should be a balance between the vacancy amount and Li^+ concentration, and the highest ionic conductivities are usually achieved for intermediate x values.

Table 5. Comparison of ionic conductivities for the deficient spinel-type $\text{Li}_{2-2x}\text{M}_{1+x}\text{Cl}_4$ SSEs and their stoichiometric counterpart.

Material	Conductivity (S cm^{-1})	Ref.
----------	-------------------------------------	------

$\text{Li}_{2-2x}\text{Mn}_{1+x}\text{Cl}_4$	Li_2MnCl_4	0.05 at 300 °C	41
	$\text{Li}_{1.6}\text{Mn}_{1.2}\text{Cl}_4$	0.4 at 300 °C	106
	$\text{Li}_{1.52}\text{Mn}_{1.24}\text{Cl}_4$	~ 0.5 at 300 °C, 1.5×10^{-5} at 25 °C	40
$\text{Li}_{2-2x}\text{Fe}_{1+x}\text{Cl}_4$	$\text{Li}_{1.6}\text{Fe}_{1.2}\text{Cl}_4$	1.3×10^{-5} at 20 °C, compared to $\sim 10^{-6}$ for Li_2FeCl_4	39
$\text{Li}_{2-2x}\text{Cd}_{1+x}\text{Cl}_4$	Li_2CdCl_4	5.9×10^{-3} at 200 °C, 0.32 at 400 °C	105
	$\text{Li}_{1.9}\text{Cd}_{1.05}\text{Cl}_4$	0.1 at 200 °C, 0.35 at 400 °C	40, 105
$\text{Li}_{2-2x}\text{Mg}_{1+x}\text{Cl}_4$	Li_2MgCl_4	2.4×10^{-7} at 25 °C	40
	$\text{Li}_{1.6}\text{Mg}_{1.2}\text{Cl}_4$	3.4×10^{-5} at 25 °C	40
$\text{Li}_{2-2x}\text{Mn}_{1+x}\text{Br}_4$	Li_2MnBr_4	7.3×10^{-2} at 400 °C	108
	$\text{Li}_{1.6}\text{Mn}_{1.2}\text{Br}_4$	8.9×10^{-2} at 400 °C	108
$\text{Li}_{2-2x}\text{Mg}_{1+x}\text{Br}_4$	Li_2MgBr_4	4.5×10^{-2} at 400 °C	108
	$\text{Li}_{1.6}\text{Mg}_{1.2}\text{Br}_4$	7.1×10^{-2} at 400 °C	108

2.3.3 Distorted structure

There's also another type of distorted structure, mainly including Li_2MCl_4 ($\text{M} = \text{Cr}, \text{Fe}, \text{Co}$) and Li_2MBr_4 ($\text{M} = \text{Mn}, \text{Mg}, \text{Fe}$) SSEs. Only Li_2CrCl_4 possesses a monoclinic lattice with a space group of C2/m .¹⁰⁰ Li_2FeCl_4 ¹⁰⁰ and Li_2CoCl_4 ¹⁰³ SSEs reported by Ryoji Kanno et al. were an orthorhombic structure with a space group of Imma , and the distribution of Li^+ and M^{2+} cations on the octahedral sites are ordered. However, H. D. Lutz et al. reported that distorted structure should be deficient ordered rock-salt type SnMn_2S_4 (space group Cmmm) for Li_2FeCl_4 ,¹¹⁶ Li_2CoCl_4 ,¹¹⁷ and Li_2MBr_4 ($\text{M} = \text{Mn}, \text{Mg}, \text{Fe}$),¹¹⁸⁻¹²⁰ which are different from that proposed by Kanno. Generally, the distorted SSEs exhibited relatively low ionic conductivity compared to their counterparts with a cubic inverse spinel structure caused by the ordered distribution of Li^+ and M^{2+} cations.

2.3.4 Suzuki structure (deficient LiCl-type)

Suzuki phases can only be found in chloride-based Li_6MCl_8 SSEs ($\text{M} = \text{V}, \text{Fe}, \text{Co}, \text{Ni}$)^{55, 110-112, 121}, and bromide-based Li_6MBr_8 SSEs ($\text{M} = \text{Mn}, \text{Mg}$)¹¹⁹ with deficient LiCl-type solid solution Li_{1-2x}

$M_xV_x''X$ (V'' = vacancy, $X = \text{Cl, Br}$), where $x = 0.125$ with $\text{Li/M ratio} = 6$. Such structure is rock salt derivatives with an ordered arrangement of cations (Li^+ , M^{2+}) and vacancies in the octahedral sites. Different from the inverse spinel structures, the MX_6 octahedron is isolated from each other in Suzuki structures, as shown in Figure 5e. Different from the poor ionic conduction properties of LiCl ($\sim 10^{-10} \text{ S cm}^{-1}$ at 25°C), with all of the octahedra occupied by Li^+ ions, the presence of the vacancies in Li_6MCl_8 SSEs ($\text{M} = \text{V, Fe, Co, Ni}$) were expected to significantly enhance the Li^+ migration. The much higher Li^+ ionic motion of those Li_6MX_8 SSEs compared to LiCl were proved by neutron diffraction¹²² and impedance tests^{110, 111}, and corresponding ionic conductivities are listed in Table 5.

In general, the ionic conductivities of halide SSEs with olivine and normal spinel structure are lower than that of inverse spine structures, which is also lower than deficient-type inverse spinel structures. The trend of ionic conductivity variation indicates that Li^+ ions in tetrahedral sites are highly mobile and partial empty sites are good for lowering energy barriers for mobile Li^+ ions. As clearly seen from Table 4, these types of halide SSEs were mainly developed around the 1990s and show low ionic conductivity compared to halide SSEs with trivalent metal elements. Further improvement of ionic conductivity should be the priority before their possible application in ASSLBs.

2.4 Halide SSEs with non-metal elements (N, O, S)

Besides the above-mentioned halide SSEs with metal elements, we also summarized the nonmetal counterparts here. The first type is ternary lithium-nitrogen-halogen (Li-N-X , $\text{X} = \text{Cl, Br, I}$) compounds. Those SSEs were mainly studied around the 1980s, including $\text{Li}_9\text{N}_2\text{Cl}_3$,^{123, 124} Li_6NBr_3 ,¹²⁴⁻¹²⁶ Li_5NI_2 ,^{124, 126, 127} and related compounds. As can be seen in Table 6, those SSEs exhibit relatively low ionic conductivities around 10^{-7} - $10^{-6} \text{ S cm}^{-1}$, and narrow electrochemical window up to $\sim 2.5 \text{ V}$ vs. Li/Li^+ .¹²⁴ The second type is lithium anti-perovskite electrolytes, including lithium-oxide halides (Li_3OX),^{47, 128-130} lithium-hydroxide halides (Li_2OHX , or $\text{Li}_{3-x}\text{OH}_x\text{Cl}$),¹³¹⁻¹³⁴ and related compounds.¹³⁵

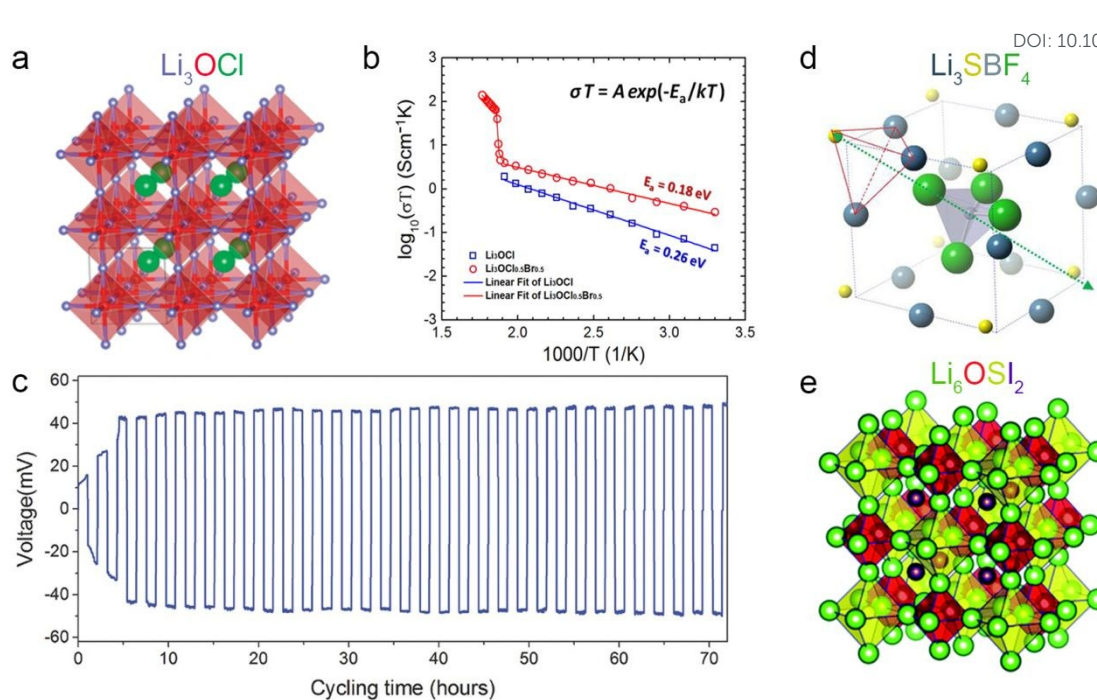


Figure 6. (a) Crystal structure of Li_3OCl with anti-perovskite structure. Reproduced with permission from ref. 136. Copyright (2014) Royal Society of Chemistry. (b) Arrhenius plots of Li_3OCl and $\text{Li}_3\text{OCl}_{0.5}\text{Br}_{0.5}$ anti-perovskites. Reproduced with permission from ref 129. Copyright (2012) American Chemical Society. (c) Cyclability of the $\text{Li}/\text{Li}_3\text{OCl}/\text{Li}$ symmetric cell at 1 mA (1 h per half a cycle). Reproduced with permission from ref. 137. Copyright (2016) Wiley. (d) The optimized unit cell of Li_3SBF_4 . The green arrow indicates the C_{3v} orientational symmetry adopted by the BF_4^- tetrahedral unit in the cubic cell. The red outline highlights the pyramidal configuration of Li_3S^+ . Reproduced with permission from ref. 138. Copyright (2017) U.S. National Academy of Sciences. (e) Typical double antiperovskite phase structure of Li_6OSI_2 . Reproduced with permission from ref. 139. Copyright (2018) Royal Society of Chemistry.

As presented in Figure 6a, Li_3OX possesses typical anti-perovskite structure by changing the normal perovskite ABO_3 to inverted charge $\text{A}^+\text{B}^{2-}\text{X}^{3-}$. In 2012, Yusheng Zhao et al. successfully synthesized Li_3OCl and $\text{Li}_3\text{OCl}_{0.5}\text{Br}_{0.5}$ anti-perovskite SSEs, which exhibited RT ionic conductivity of 0.85×10^{-3} and $1.94 \times 10^{-3} \text{ S cm}^{-1}$, respectively (Figure 6b).¹²⁹ Later, they also synthesized Li_3OCl films by pulsed laser deposition (PLD) method,^{136, 137} and declared that Li_3OCl SSE shows a self-stabilization when direct contact with Li metal, thus revealing good compatibility toward Li.^{136, 137, 140}

The cycling performance of the Li/Li₃OCl/Li symmetric cell at 1 mA was shown in Figure 6c. However, as mentioned above, Li₃OCl faces the problem of a narrow electrochemical window up to 2.5-3.0 V vs. Li/Li⁺.⁴⁷ Li₂OHX also adopts the A-B²-X₃ structure, where only two-thirds of the Li⁺ positions are occupied, leaving the others vacant. It is believed that the existence of vacancy as well as anion disorder would lead to facile Li⁺ migration,^{130, 141, 142} however, due to the repulsive force of H atoms that co-occupied together with O within the Li₂OHX structure, the Li⁺ migration is restricted. Thus, the reported ionic conductivities of Li₂OHX are about 10⁻⁸-10⁻⁵ S cm⁻¹, which are much lower than that of 10⁻⁶-10⁻³ S cm⁻¹ for Li₃OX (Table 6). Moreover, Li₂OHCl SSE was proved to display stability against metallic lithium even at 195 °C by Chengdu Liang et al., and they declared that the good stability is attributed to the stable solid electrolyte interphase (SEI) layer formation between Li₂OHCl SSE and Li metal.¹³⁴ It should be noted that the composition of Li₃OX is debatable since reported Li₃OX might also contain undesired OH in the final product.^{128, 143} Li₃OCl based glasses SSEs were also developed with ultra-high ionic conductivity even over 10 mS cm⁻¹.^{144, 145} Nevertheless, it seems that Li⁺, Cl⁻, and proton might be responsible for the conduction property,^{146, 147} and the “high” ionic conductivity of those glass SSEs is probably due to the decomposition product of amorphous LiCl·xH₂O that offer high conductivity.¹⁴⁸

Guided by the typical anti-perovskite structure of Li₃OX SSEs, Puru Jena et al. further explored other possible lithium-rich anti-perovskites based on cluster ions by theoretical calculations.¹³⁸ They demonstrated that using cluster ions, i. e. superhalogens, with properly larger ionic radius can stabilize the anti-perovskite structure and enlarge the channel size, thus leading to fast Li⁺ migration. Typically, Li₃SBF₄ (optimized unit cell of presented in Figure 6d), was estimated to have a RT ionic conductivity of 10⁻² S cm⁻¹ as well as low activation energy of 0.210 eV. They also predicted that partially replace the larger superhalogen with halogen can further increase the conductivity, and the mixed phase of Li₃S(BF₄)_{0.5}Cl_{0.5} is estimated to exhibit an ultra-high value of 10⁻¹ S cm⁻¹.¹³⁸ However, there's still no experimental result reported until now. Later, Guosheng Shao et al. also further explored double-anti-

perovskite structure by theoretical calculations.^{139, 149} A new double anti-perovskite compound with the stoichiometry of Li_6OSI_2 is identified theoretically by mixing O^{2-} and S^{2-} in the chalcogen site. As presented in Figure 6e, Li_6OSI_2 possesses a face centered structure, with an alternate arrangement of Li_6O and Li_6S octahedra within the structure. The estimated ionic conductivity of Li_6OSI_2 and its Li^+ enriched derivate form of $\text{Li}_{25}\text{O}_4\text{S}_5\text{I}_7$ can be as high as $0.1\text{--}1.25 \times 10^{-2} \text{ S cm}^{-1}$ at 300 K. Though they mentioned that Li_6OSI_2 was successfully synthesized and exhibited experimentally measured conductivity of $7.89 \times 10^{-3} \text{ S cm}^{-1}$, no any detailed ionic conductivity measurement information was given,¹³⁹ and the value is actually much lower about $5.53 \times 10^{-6} \text{ S cm}^{-1}$ even at 75°C in their later work.¹⁵⁰

Table 6. Halide SSEs with non-metal elements.

Material	Conductivity (S cm^{-1})	Ref.
$\text{Li}_{1.8}\text{N}_{0.4}\text{Cl}_{0.6}$	$\sim 8.4 \times 10^{-7} \text{ S cm}^{-1}$ at 25°C	123
$\text{Li}_{1.8}\text{N}_{0.6}\text{Cl}_{0.8}$	$\sim 10^{-6} \text{ S cm}^{-1}$ at 25°C	124, 126
Li_5NI_2	$\sim 10^{-7} \text{ S cm}^{-1}$ at 25°C	124, 126
Li_6NBr_3	$\sim 10^{-7} \text{ S cm}^{-1}$ at 25°C	124, 126
Li_5NI_2	$4 \times 10^{-6} \text{ S cm}^{-1}$ at 27°C	127
$\text{Li}_5\text{NI}_2\text{--}0.77\text{LiOH}$	$10^{-3} \text{ S cm}^{-1}$ at 27°C (NMR)	151
Li_6NBr_3	$1.86 \times 10^{-7} \text{ S cm}^{-1}$ at 65°C , $10^{-3} \text{ S cm}^{-1}$ at 250°C	125
Li_3OCl	$0.85 \times 10^{-3} \text{ S cm}^{-1}$ at 25°C	129
Li_3OCl	$0.2 \times 10^{-3} \text{ S cm}^{-1}$ at 25°C	137
$\text{Li}_3\text{OCl}_{0.5}\text{Br}_{0.5}$	$1.94 \times 10^{-3} \text{ S cm}^{-1}$ at 25°C	129
$\text{Li}_{2.85}\text{Mg}_{0.075}\text{OCl}$	$2 \times 10^{-9} \text{ S cm}^{-1}$ at 25°C	152
$\text{Li}_{2.9}\text{Ca}_{0.05}\text{OCl}_{0.68}\text{Br}_{0.32}$	$8 \times 10^{-6} \text{ S cm}^{-1}$ at 25°C	152
Li_3OBr	$1 \times 10^{-6} \text{ S cm}^{-1}$ at 25°C	128
$56\text{Li}_3\text{OBr}\text{--}44\text{Li}_7\text{O}_2\text{Br}_3$	2.4×10^{-5} at 25°C	153
$\text{Li}_2(\text{OH})\text{I}$	$3 \times 10^{-6} \text{ S cm}^{-1}$ at 150°C	131
$\text{Li}_5(\text{OH})_4\text{I}$	$2 \times 10^{-5} \text{ S cm}^{-1}$ at 150°C	131
$\text{Li}_2(\text{OH})\text{Cl}$	$3 \times 10^{-5} \text{ S cm}^{-1}$ at 200°C	131
$\text{Li}_5(\text{OH})_3\text{Cl}_2$	$7.5 \times 10^{-4} \text{ S cm}^{-1}$ at 200°C	131
$\text{Li}_{1.16}(\text{OH}_{1.84})\text{Cl}$	$\sim 10^{-6} \text{ S cm}^{-1}$ at 25°C	132

$\text{Li}_2(\text{OH})\text{Cl}$	$\sim 10^{-8} \text{ S cm}^{-1}$ at 25 °C	132
$\text{Li}_{1.04}(\text{OH}_{1.96})\text{Br}$	$\sim 10^{-7} \text{ S cm}^{-1}$ at 25 °C	132
$\text{Li}_2(\text{OH})\text{Br}$	$\sim 10^{-7} \text{ S cm}^{-1}$ at 25 °C	132
$\text{Li}_2(\text{OH})_{0.9}\text{F}_{0.1}\text{Cl}$	$3.5 \times 10^{-5} \text{ S cm}^{-1}$ at 25 °C, $1.9 \times 10^{-3} \text{ S cm}^{-1}$ at 100 °C	133
$\text{Li}_2\text{OHBr}_{0.98}\text{F}_{0.02}$	$1.1 \times 10^{-6} \text{ S cm}^{-1}$ at 25 °C	154
$\text{Li}_5(\text{OH})_2\text{Cl}_3$	$1.48 \times 10^{-7} \text{ S cm}^{-1}$ at 25 °C, $\sim 2.5 \times 10^{-8} \text{ S cm}^{-1}$ at 100 °C	134
$\text{Li}_2(\text{OH})\text{Cl}$	$\sim 4 \times 10^{-8} \text{ S cm}^{-1}$ at 25 °C, $\sim 2 \times 10^{-7} \text{ S cm}^{-1}$ at 100 °C	134
Li_6OSI_2	$1.03\text{-}5.0 \times 10^{-3} \text{ S cm}^{-1}$ at 27 °C (calculated)	139
$\text{Li}_{25}\text{O}_4\text{S}_5\text{I}_7$	$1.25 \times 10^{-2} \text{ S cm}^{-1}$ at 27 °C (calculated)	139
Li_6OSI_2	$7.89 \times 10^{-3} \text{ S cm}^{-1}$ at 25 °C ^a	139
Li_6OSI_2	$5.53 \times 10^{-6} \text{ S cm}^{-1}$ at 75 °C	150
$\text{Li}_{6.5}\text{OS}_{1.5}\text{I}_{1.5}$	$2.28 \times 10^{-5} \text{ S cm}^{-1}$ at 75 °C	150
Li_3SBF_4	$10^{-2} \text{ S cm}^{-1}$ at 25 °C (calculated)	138
$\text{Li}_3\text{S}(\text{BF}_4)_{0.5}\text{Cl}_{0.5}$	$10^{-1} \text{ S cm}^{-1}$ at 25 °C (calculated)	138

a. Not given any detailed experimentally ionic conductivity measurement information.

In general, the relatively low ionic conductivity of the halide SSEs achieved in the early stages of development has been significantly improved in recent years. A number of halide SSEs showing high Li^+ conductivities (around $10^{-3} \text{ S cm}^{-1}$) have been developed to date. Besides the experimentally identified highly conductive halide SSEs, a wide variety of halide SSEs that might possess ultra-high ionic conductivities have been calculated and predicted as listed above. Due to the diversity of halide SSEs with tunable components and advanced theoretical techniques that have accelerated the search for candidate SSEs with high ionic conductivity, the fast development of halide SSEs with superionic conductivities is expected in the near future. Moreover, crystallographic studies and atomic-level characterizations to explore the local structures and ionic conductive mechanisms are also required as they provide the guidelines for the development of new halide SSEs.

3. Synthesis

For the preparation of halide SSEs, conventional synthesis protocols, such as solid-state reaction methods (annealing, mechanical milling, or a combination of the two) and newly developed liquid-

phase synthesis methods have been applied. Moreover, the chemical vapor method was also developed for the synthesis of fluoride-based SSEs with thin films (Figure 7 and Table 7).

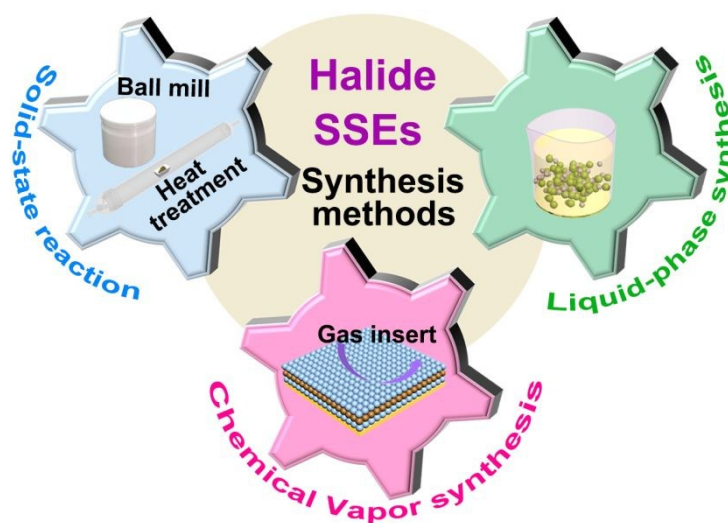


Figure 7. Synthesis methods of halide SSEs.

Table 7. Typical synthesis methods of halide SSEs.

Synthesis methods		Halide SSEs	Conductivity (25 °C, S cm ⁻¹)	Ref.
Solid state reaction	Mechanical mill	Li ₃ YCl ₆	5.1×10 ⁻⁴	14
		Li ₃ YCl ₆	9.5×10 ⁻⁵	44
		Li ₃ YBr ₆	7.2×10 ⁻⁴	14
		Li ₃ ErCl ₆	3.3×10 ⁻⁴	43
		Li ₃ ErCl ₆	3.1×10 ⁻⁴	44
		Li ₃ InCl ₆	8.4×10 ⁻⁴	15
		Li ₃ ErI ₆	6.5×10 ⁻⁴	46
	Annealing	Li ₃ YCl ₆	3×10 ⁻⁵	14
		Li ₃ YCl ₆	3.4-5.5×10 ⁻⁵	44
		Li ₃ YBr ₆	1.7×10 ⁻³	14
		Li ₃ ErCl ₆	5.0×10 ⁻⁵	43
		Li ₃ ErCl ₆	0.17-1.0×10 ⁻⁴	44
		Li ₃ InCl ₆	1.02-1.49×10 ⁻³	15
		Li ₃ YbCl ₆	~10 ⁻⁴ at 300 °C	59
		LiGaBr ₄	7×10 ⁻⁶	53
Liquid-phase synthesis	Water solvent	Li ₃ InCl ₆	2.04×10 ⁻³	16
	Water/ethanol solvent	Li ₂ TiF ₆	Not given	155
	Ionic liquid solvent	β-Li ₃ AlF ₆	2.04×10 ⁻⁵ a	156
	Hexane solvent	Li _{1.16} (OH _{1.84})Cl	~10 ⁻⁶	132

		$\text{Li}_{1.04}(\text{OH}_{1.96})\text{Br}$	$\sim 10^{-7}$	132
Chemical vapor synthesis	Thermal evaporation	$\text{mLiF} \cdot \text{nAlF}_3$ ($1/3 \leq m/n \leq 3$)	$\sim 10^{-6}$	36
		$\text{mLiF} \cdot \text{MF}_3$ (M = Al, Cr, Sc, or Al + Sc)	$\sim 10^{-6}$	37
	ALD	$(\text{AlF}_3)(\text{LiF})_x$ alloy	7.6×10^{-6}	89
		LiAlF_4	$3.5 \pm 0.5 \times 10^{-8}$	157
		Li_3AlF_6	Not given	158

a. The ionic conductivity might partially due to ionic liquid residual on the surface.

3.1 Solid-state reaction method (Mechanical milling, annealing)

Similar to the synthesis of other types of SSEs, the solid-state reaction is the most popular method of synthesizing halide SSEs, and most of the procedures have to be handled in a dry Ar-filled glove box. Initially, stoichiometric amounts of halide starting materials were directly sealed in quartz (or glass tubes) without a fine mixture process. Thus, the following annealing process usually needs a relatively long time over several days to complete the reactions. For example, Li_3MCl_6 (M = Tb-Lu, Y, Sc)⁵⁹, Li_3MBr_6 (M = Sm-Lu, Y)⁶² were synthesized in quartz ampoules at 400 °C for 2 weeks, as reported in 1997. More recently, the halide starting materials have been finely mixed by a mechanical ball-milling process before sealing in quartz tubes. Thus, the subsequent heating time is highly reduced, even to 1 h, to obtain the final halide SSEs (e. g., Li_3YCl_6 , Li_3InCl_6 , Li_3ErCl_6).^{14, 15, 43-45} Sokseiha Muy et al. synthesized highly-crystallized Li_3ErCl_6 by heating the mechanical ball-milled chloride mixtures at 550 °C for 1 h. However, it should be mentioned that the halide mixtures might not be a solid phase when the heating temperature is too high based on their corresponding phase diagram. For instance, based on $\text{LiCl}-\text{YCl}_3$ ¹⁵⁹ and $\text{LiCl}-\text{ErCl}_3$ ¹⁶⁰ phase diagram, Li_3YCl_6 ¹⁴ and Li_3ErCl_6 ⁴³ should exist in the melted liquid phase at 550 °C, while such melted liquid phases are rarely mentioned in previous work. Overall, the application of quartz tubes/ampoules for such synthetic approaches makes it difficult for scale-up synthesis.

Another method is the direct mechanical ball-milling approach without any further treatment. Halide SSEs with relatively lower crystallinity can be formed with appropriate milling time and speed.

It's supposed that the mechanical ball-milling is performed under room temperature, but there will be heat generated during the high energy ball-milling process. In general, the structure of halide SSEs is totally different from the halide starting materials, indicating the chemical reaction between the halide starting materials occurs rather than just obtaining a physical mixture of them. Moreover, the ionic conductivities of some halide SSEs obtained by the mechanical ball-milling approach are higher than the annealing route. This phenomenon can be found for both Li_3YCl_6 and Li_3ErCl_6 SSEs.^{14, 43, 44} Typically, the ball-milled Li_3YCl_6 and heated Li_3YCl_6 showed RT ionic conductivity of 5×10^{-4} and $3 \times 10^{-5} \text{ S cm}^{-1}$, respectively;¹⁴ the ball-milled Li_3ErCl_6 and heated Li_3ErCl_6 showed RT ionic conductivity of 3.3×10^{-4} and $5 \times 10^{-5} \text{ S cm}^{-1}$, respectively.⁴³ The authors explained that the noticeably high conductivity of ball-milled SSE might be related to subtle structural differences (cation site disorder) and more defects induced by ball-milling. The mechanical ball-milling approach can achieve SSEs with smaller size that can be directly used in ASSLBs without further pulverization. Nevertheless, the amount of SSEs is highly dependent on the size of the ball-milling jar. The homogeneity of SSEs would be poor in the condition of too many halide starting materials due to the possible agglomeration of particles on the inner surface of the ball-milling jar.

3.2 Liquid-phase synthesis

Similar to liquid-phase synthesis for sulfide-base SSEs,¹⁶¹⁻¹⁶⁵ some of halide SSEs can also be obtained through liquid-phase reactions. Moreover, some can even be directly synthesized in water solvent without the need of a protected argon atmosphere, which further opens several opportunities for scalable halide SSEs synthesis. In general, the liquid-phase synthesis strategy offers several advantages: 1) easy mass production by avoiding difficult mixing precursors procedures, getting rid of special apparatus, shortening the reaction time, and reducing the reaction temperature; 2) effective size/morphology control by homogeneous dissolution or dispersing of the raw materials/intermediates in the liquid-phase solution; 3) possible potential to be used as ionic conductive coating layer on the surface of electrode material particles.

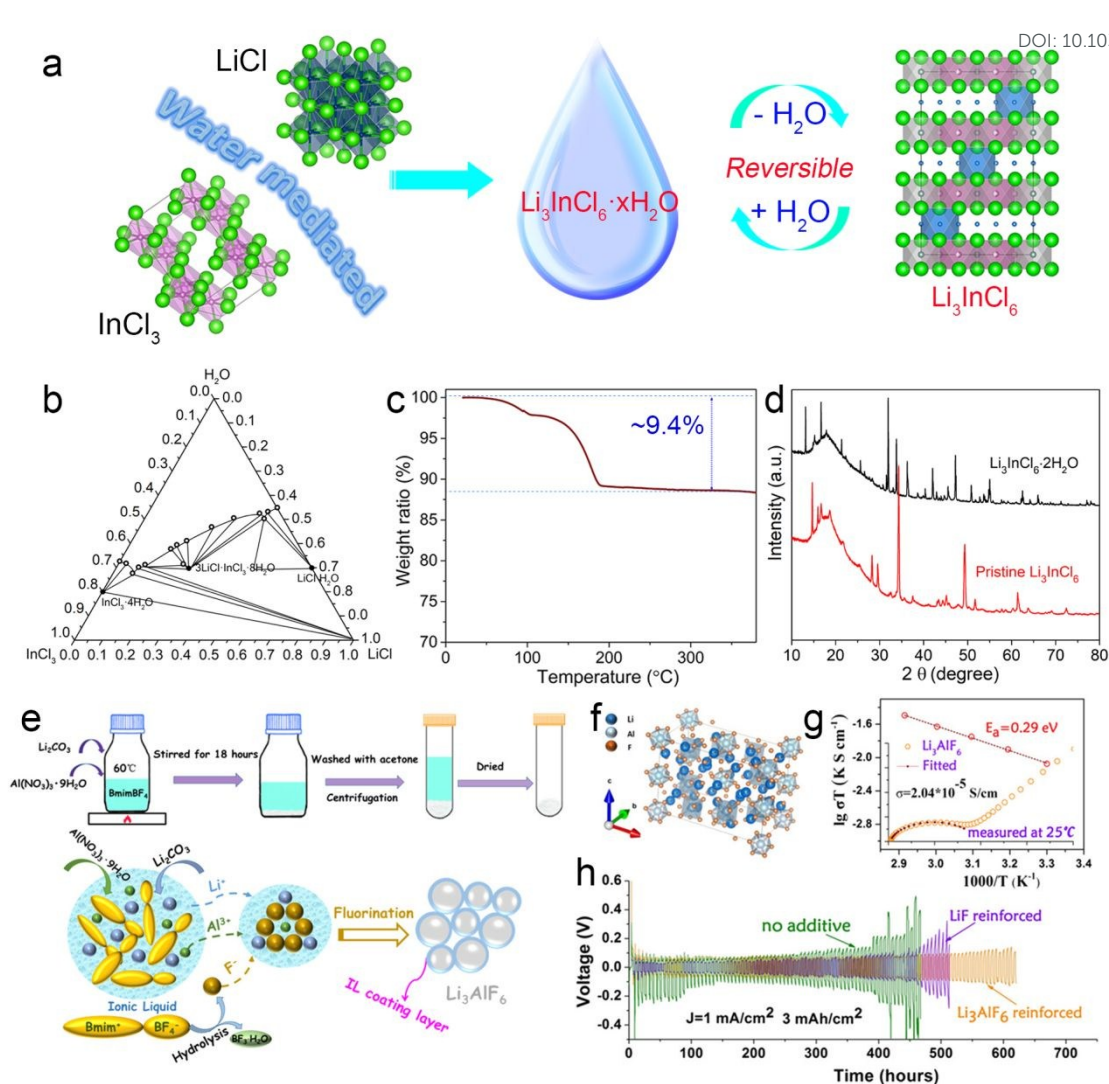


Figure 8. (a) Illustration of a water-mediated synthesis route for Li_3InCl_6 and the reversible conversion between the hydrated $\text{Li}_3\text{InCl}_6 \cdot x\text{H}_2\text{O}$ and dehydrated Li_3InCl_6 . Reproduced with permission from ref. 16. Copyright (2019) Wiley. (b) Phase diagram of system $\text{LiCl}-\text{InCl}_3-\text{H}_2\text{O}$ at 25 °C. Reproduced with permission from ref. 166. Copyright (1977) Canadian Science Publishing. (c) TGA of $\text{Li}_3\text{InCl}_6 \cdot x\text{H}_2\text{O}$ tested from room temperature to 380 °C under N_2 . (d) XRD pattern of the $\text{Li}_3\text{InCl}_6 \cdot x\text{H}_2\text{O}$ and Li_3InCl_6 . Reproduced with permission from ref. 16. Copyright (2019) Wiley. (e) Schematic synthesis of Li_3AlF_6 from BmimBF_4 ambience. (f) Crystal structure of $\beta\text{-Li}_3\text{AlF}_6$. (g) Impedance spectra of LAF-60. (h) Li plating/stripping performance of Li/Li symmetric cells in the EC-DMC- LiPF_6 system with and without 0.1 M LAF-60 as additive. Reproduced with permission from ref. 156. Copyright (2018) American Chemical Society.

3.2.1 Water-mediated synthesis of Li_3InCl_6 SSE

Recently, the first report of the liquid-phase synthesis of Li_3InCl_6 using H_2O solvent by our group has made halide SSEs very attractive compared to traditional sulfide-based SSEs.¹⁶ As presented in Figure 8a, Li_3InCl_6 can be successfully prepared through a facile and scalable water-mediated synthesis route ($3\text{LiCl} + \text{InCl}_3 \xrightarrow{\text{H}_2\text{O}} \text{Li}_3\text{InCl}_6 \cdot x\text{H}_2\text{O} \xrightarrow{\Delta} \text{Li}_3\text{InCl}_6$). Simply dissolving lithium chloride and indium chloride into water can obtain a white $\text{Li}_3\text{InCl}_6 \cdot x\text{H}_2\text{O}$ intermediate complex precursor. The amount of crystalline water is determined to be 2 based on the TGA curve (Figure 8c), which is different from that of $3\text{LiCl} \cdot \text{InCl}_3 \cdot 8\text{H}_2\text{O}$ ($\text{Li}_3\text{InCl}_6 \cdot 8\text{H}_2\text{O}$) in the phase diagram of system $\text{LiCl}-\text{InCl}_3-\text{H}_2\text{O}$ reported by Elinor M. Kartzmark in 1977 (Figure 8b).¹⁶⁶ Upon further heating at 200 °C under vacuum, the $\text{Li}_3\text{InCl}_6 \cdot 2\text{H}_2\text{O}$ intermediate complex precursor can totally convert to crystalline Li_3InCl_6 . The XRD patterns of the $\text{Li}_3\text{InCl}_6 \cdot 2\text{H}_2\text{O}$ intermediate complex precursor and final Li_3InCl_6 are totally different from each other (Figure 8d). Moreover, reversible conversion between Li_3InCl_6 and $\text{Li}_3\text{InCl}_6 \cdot 2\text{H}_2\text{O}$ has been confirmed, thus ensuring high tolerance toward air and humidity as well as recoverable high ionic conductivity as mentioned above. In addition, such water-mediated synthesis routes are highly favorable for practical manufacturing, the synthesis of Li_3InCl_6 SSEs can be easily scaled-up to 111 g with high purity and ionic conductivity.

Surprisingly, it was found that lots of double salts between InCl_3 and the alkali metal halides with coordinate water have been reported (such as $2\text{NH}_4\text{Cl} \cdot \text{InCl}_3 \cdot \text{H}_2\text{O}$, $3\text{KCl} \cdot \text{InCl}_3 \cdot \text{H}_2\text{O}$, $2\text{KCl} \cdot \text{InBr}_3 \cdot \text{H}_2\text{O}$, $\text{LiCl} \cdot \text{MgCl}_2 \cdot 7\text{H}_2\text{O}$, $\text{MgCl}_2 \cdot \text{InCl}_3 \cdot (6-8)\text{H}_2\text{O}$, $\text{CaCl}_2 \cdot \text{InCl}_3 \cdot 7\text{H}_2\text{O}$, $2\text{CsCl} \cdot \text{InCl}_3 \cdot \text{H}_2\text{O}$).¹⁶⁶⁻¹⁷⁰ The existence of these indium-based hydrated complexes indicates the possibility for synthesis of indium-based halide electrolytes with different ion conductivity, such as NH_4^+ , Li^+ , K^+ , Ga^{2+} , Mg^{2+} through a dehydration synthesis route. Typically, Na_3InCl_6 SSE has been successfully been prepared by our group via the water-mediated route.¹⁶ Moreover, those indium-based halide electrolytes should also possess reversible conversion between dehydrated and hydrated forms. Interestingly, the reversible conversion between $\text{Cs}_2\text{InBr}_5 \cdot \text{H}_2\text{O}$ and the dehydrated form together with

switchable dual emission make it function as a photoluminescence water-sensor in humidity detection.¹⁷¹

Furthermore, the above-mentioned liquid-phase synthesis routes based on water for halide SSEs have obvious advantages over the synthesis of sulfide-based SSEs. Firstly, the synthesis process can be performed directly in ambient air without an inert environment, making the synthesis significantly easier. Secondly, sulfide-based SSEs obtained from liquid-phase synthesis usually show relatively low ionic conductivity due to the residual organic solvent on the surface of electrolyte, which this is not a concern when using water as the solvent for the synthesis of halide SSEs.

3.2.2 Possible other liquid synthesis route based on halide hydrated complexes

In addition to indium-based compounds, there are many other kinds of halide hydrated complex, which also provides possible routes for synthesis halide SSEs directly from the liquid-phase synthesis route. For example, $\text{Li}_3\text{RuCl}_6 \cdot 6\text{H}_2\text{O}$ was synthesized in an ethanol solution from LiCl and $\text{RuCl}_3 \cdot n\text{H}_2\text{O}$ in 2004.¹⁷² Li_3RuCl_6 might be able to be obtained through dehydration of $\text{Li}_3\text{RuCl}_6 \cdot 6\text{H}_2\text{O}$. Similarly, alkali metal bismuth chloride double salts ($\text{Li}_2\text{BiCl}_5 \cdot 6\text{H}_2\text{O}$, $\text{K}_4\text{Bi}_2\text{Cl}_{10} \cdot 4\text{H}_2\text{O}$ ¹⁷³, $\text{Na}_2\text{BiCl}_5 \cdot 5\text{H}_2\text{O}$ ¹⁷⁴) can also be obtained through co-crystallization of alkali chloride with BiOCl or $(\text{BiO})_2\text{CO}_3$ in aqueous HCl . The existence of such kind of halide hydrated complex provides potential effective synthesis route to obtain halide SSEs directly through dehydration routes.

Fluoride-type SSEs can also be synthesized through liquid synthesis routes. Due to the high negativity of F^- , some Li-M-F materials have been proved to can be directly obtained with the existence of water. For example, alkali hexafluorogallates of A_3GaF_6 , ($\text{A} = \text{Li}, \text{Na}, \text{K}$) can be synthesized by milling AF and $\text{GaF}_3 \cdot 3\text{H}_2\text{O}$.¹⁷⁵ It's supposed that the dissolution of alkali fluorides in water is an important factor for the reaction, and LiF with the lowest solubility leads to the impurity of the final products. Li_2TiF_6 SSE was also synthesized based on the reaction between Li_2CO_3 and H_2TiF_6 in H_2O /ethanol solvent.¹⁵⁵

Moreover, the solvent for the synthesis of halide SSEs can not only dependent on water solvent, other organic solvents are also promising. For example, Chilin Li et al. synthesized β -Li₃AlF₆ SSE from the reaction among Li₂CO₃, Al(NO₃)₃·9H₂O, and 1-butyl-3-methylimidazolium tetrafluoroborate (BmimBF₄) ionic liquid in BmimBF₄ solution (Figure 8e).¹⁵⁶ β -Li₃AlF₆ SSE (structure shown in Figure 8f) obtained dried at 60 °C (denoted as LAF-60) exhibited a RT ionic conductivity of 2.04×10^{-5} S cm⁻¹ (Figure 8g). Comparatively, as mentioned above, previously reported β -Li₃AlF₆ can possess ionic conductivity of 5×10^{-5} S cm⁻¹ at 300 °C.³⁸ The significant improvement of ionic conductivity is partially due to the residual BmimBF₄ on the surface. It was supposed that LAF-60 can enable homogeneous Li⁺ flux and accelerate Li⁺ transport across the LAF-60 layer due to the relatively high ionic conductivity. Thus, the stable cyclability of Li/Li symmetric cells can be achieved with LAF-60 layer protection in liquid electrolyte systems (Figure 8h).

3.3 Chemical vapor synthesis

Besides the synthesis of powders, thin film type halide SSEs were also developed, especially for the fluoride-based SSEs. There are mainly two methods, including thermal evaporation and atomic layer deposition (ALD) approaches. Tetsu Oi et al. firstly synthesized mLiF·nAlF₃ ($1/3 \leq m/n \leq 3$) thin film Li⁺ conductor from the evaporation of a mixture of LiF and AlF₃ onto a glass substrate. The obtained mLiF·nAlF₃ thin film was amorphous and exhibited a RT ionic conductivity over 10^{-6} S cm⁻¹ in the range of $1 \leq m/n \leq 5/3$.³⁶ Later, they also developed amorphous mLiF-MF₃ (M = Al, Cr, Sc, or Al + Sc) thin films, where all four LiF-MF₃ systems can achieve ionic conductivities over 10^{-6} S cm⁻¹. They further studied the structures of compositions with high ionic conductivities and concluded that 8- or 9-coordination in the fluoride type SSEs would achieve higher ionic conductivity compared to 4- or 6-coordination. Nevertheless, as mentioned above, the migrated ions in these systems might not be pure Li⁺, proton, and F⁻ migration might also contribute to the total conduction.³⁷ (AlF₃)(LiF)_x alloy,⁸⁹ LiAlF₄,¹⁵⁷ Li₃AlF₆¹⁵⁸ films were also obtained by ALD approaches, with ionic conductivity ranging from 10^{-8} to 7.5×10^{-6} S cm⁻¹ achieved. Moreover, due to the wide intrinsic electrochemical window of

Li-Al-F,¹⁷ LiAlF₄ thin film was also applied as a coating on the high-voltage cathode in lithium batteries by ALD approach to form a relatively conformal coating.¹⁵⁷ Though lots of other coating layers by ALD approach have been applied in ASSLBs, few fluoride type SSEs coating have been reported.

As a short summary, the synthesis of halide SSEs is mainly based on time-consuming mechanical milling and high-temperature annealing methods. Quite recently, the liquid-phase synthesis method especially the water-mediated synthesis route that was developed to synthesize halide SSEs, whereas such synthesis route is applicable to limited SSEs. In this regard, effective methods based on the liquid-phase chemistry to obtain halide SSEs in mass production with high ionic conductivity are highly demanded. Thus, subsequent research should provide not only highly conductive SSEs, but also effective synthesis route for halide SSEs. Both liquid-phase and chemical vapor synthesis methods are promising for synthesizing halide SSEs as coating layers for active electrodes.

4. Chemical/electrochemical stability

Due to the fast development of halide SSEs, several types of halide SSEs with high RT ionic conductivity of 10⁻³ S cm⁻¹ has been fabricated.^{14-16, 45} In addition to further maximizing the ionic conductivity of halide SSEs and developing systems, there are some other key parameters that should be considered for application in real ASSLBs: 1) structure stability of halide SSE; 2) air/humidity stability; 3) electrochemical window of halide SSEs; 4) compatibility between the halide SSEs and electrode materials.

4.1 Structural stability (temperature influence)

Structural stability is an essential aspect for SSEs, and a stable structure with high conductivity must be achieved in a wide temperature range for battery operation. To obtain SSEs with optimized structure/composition and high ionic conductivity, an in-depth understanding of the structural stability and evolution is required. Furthermore, it would be useful to provide information for safety and stable

working conditions. Compared to sulfide and oxide SSEs, some halide SSEs face the problem of structural-transition-derived changes in conductivity. More concerning is the fact that some of the structure-transitions occur around room temperature, leading to unstable battery operation caused by the large change of ionic conductivity.

Among the aforementioned SSEs, some of halide SSEs with group 3 elements (Sc, Y, La-Lu) have been reported to show structural-transition at high temperatures. Gerd Meyer et al. revealed that Li_3YCl_6 that possessed a trigonal structure (space group of P-3m1) at room temperature that would transform into an orthorhombic (space group of Pnma) structure when heated up to 310 °C.^{59, 176} Though Tetsuya Asano et al. also reported that the trigonal Li_3YCl_6 was stable up to 450 °C based on DSC results, they did not show any structural analysis after heating up.¹⁴ Among halide SSEs with group 13 elements (Al, Ga, In), structural-transitions are typically found in materials such as Li_3InBr_6 and LiInBr_4 SSEs. They went through a structural transition to a HT phase during heating (41-43 °C), which was destroyed after a cooling process (around -13 °C). The corresponding ionic conductivity also changed by several orders of magnitude.⁹¹ The narrow thermal stability window for Li_3InBr_6 and LiInBr_4 SSEs is the fatal weakness that has hindered their development and application in ASSLBs.

The structure transition for halide SSEs with divalent metal elements is quite complicated due to the existence of several types of structures. Previous reports declared that the Arrhenius conductivity plots of these halide SSEs showed changes in slope around 200-400 °C, indicating transition among different structures with different conductive ability. Basically, both the cubic inverse spinel and distorted spinel structures transform into a disordered structure, with all cations in octahedral sites together with vacancies similar to defective rock salt structure. Further transformation into disordered rock salt solid solutions was also observed for some compounds at high temperatures. Similarly, Suzuki structured Li_6MX_8 (deficient LiCl-type) with ordered Li^+ , M^{2+} , and vacancies distributed within the octahedral sites will undergo a gradual disordering to the final disordered LiX-based solid solutions during a heating process (259-355 °C).^{111, 121, 112} Sometimes, an intermediate non-stoichiometric

Li_2MX_4 structure might also form.¹¹⁰ Moreover, in addition to those structure transitions, some halide SSEs completely decompose at certain temperatures. For example, Li_2CdBr_4 will decompose to LiBr and CdBr_2 below 250 °C.¹⁰⁷ Ternary lithium iodides of bivalent materials such as deficient NaCl-type $\text{Li}_{1-x}\text{M}^{\text{II}}_{0.5x}\text{I}$ ($\text{M}^{\text{II}}=\text{Mn, Cd, Pb}$) can only be formed at high-temperature above 540 K, and they will decompose to LiI and MI_2 once cooled down.¹¹³

4.2 Stability toward air/humidity

The synthesis, storage, and fabrication conditions of SSEs are highly dependent on their stability toward air/humidity. If the SSEs are sensitive to air/humidity, their synthesis must be carefully designed, and the handling of SSEs, as well as further application, have to be done in a dry inert gas atmosphere. In most cases, the tedious and complicated synthesis procedure will increase the processing cost.

Halide SSEs were reported to show good stability in a dry air atmosphere. For example, $\text{Li}_3\text{YCl}_6/\text{Li}_3\text{YBr}_6$ SSEs were demonstrated to be stable in Ar/dry oxygen atmosphere.¹⁴ However, it should be noted that the results are mainly based on DSC tests, and no further structure/composition information has been provided after exposure. The situation is not optimistic when SSEs are exposed to ambient air with humidity. Even the oxide SSEs ($\text{Li}_7\text{La}_3\text{Zr}_2\text{O}_{12}$, LLZO) face the problem of Li^+/H^+ exchange reaction.¹⁷⁷⁻¹⁷⁹ Most sulfide-based SSEs also bare no tolerance to humidity due to their hypersensitive P-S environment, leading to toxic H_2S generation, decomposition, as well as significantly reduced ionic conductivity when exposed to humid air.¹⁸⁰⁻¹⁸²

Halide SSEs were demonstrated to be sensitive to moisture in the previous reports and review paper by Arumugam Manthiram et al.² It's not surprising since they are actually a combination of lithium halide and metal halides, in which most metal halides are hypersensitive towards hydrolysis. However, due to the different halides (F, Cl, Br, I) and metals centers (rare earth metals, transition metals, etc.), the properties and reaction mechanism of halide SSEs in a humid environment are far

from being well understood. Recently, our group developed Li_3InCl_6 SSE that shows high tolerance toward ambient air. All the Li_3InCl_6 samples synthesized by different methods can remain almost the same ionic conductivities and structures by reheating process after exposed to different humidities or totally dissolved into water. It was demonstrated that $\text{Li}_3\text{InCl}_6 \cdot 2\text{H}_2\text{O}$ was formed when Li_3InCl_6 SSEs were exposed to a humid atmosphere or directly submerged into water.¹⁶ After a dehydration process, Li_3InCl_6 can be reformed and the initial high ionic conductivity is also recovered after removing the crystal water. The reversible conversion between Li_3InCl_6 and $\text{Li}_3\text{InCl}_6 \cdot 2\text{H}_2\text{O}$ is quite similar to the situation of Na_3SbS_4 SSEs.¹⁸³⁻¹⁸⁵ Moreover, there are many other types of potential halide SSEs which possess hydrated forms, which may enable similar properties. Nevertheless, a deep and comprehensive understanding of the decomposition or hydration/dehydration behavior of halide SSEs remains elusive.

4.3 Stability toward electrode materials

Though the rapid development of different types of SSEs has led to ionic conductivities that can rival liquid electrolytes, the performance of assembled ASSLBs is still inferior to that of liquid-based systems. In addition to the high bulk ionic conductivity of SSEs, it is believed that fast Li^+ migration across the SSEs/electrode interface is another dominating factor for battery performance.¹⁸⁶⁻¹⁸⁸ The large interfacial resistances are caused by various reasons, such as poor interfacial contact, interfacial stress due to volume change, and instability issues involved with chemical reactions.

4.3.1 Stability toward cathodes

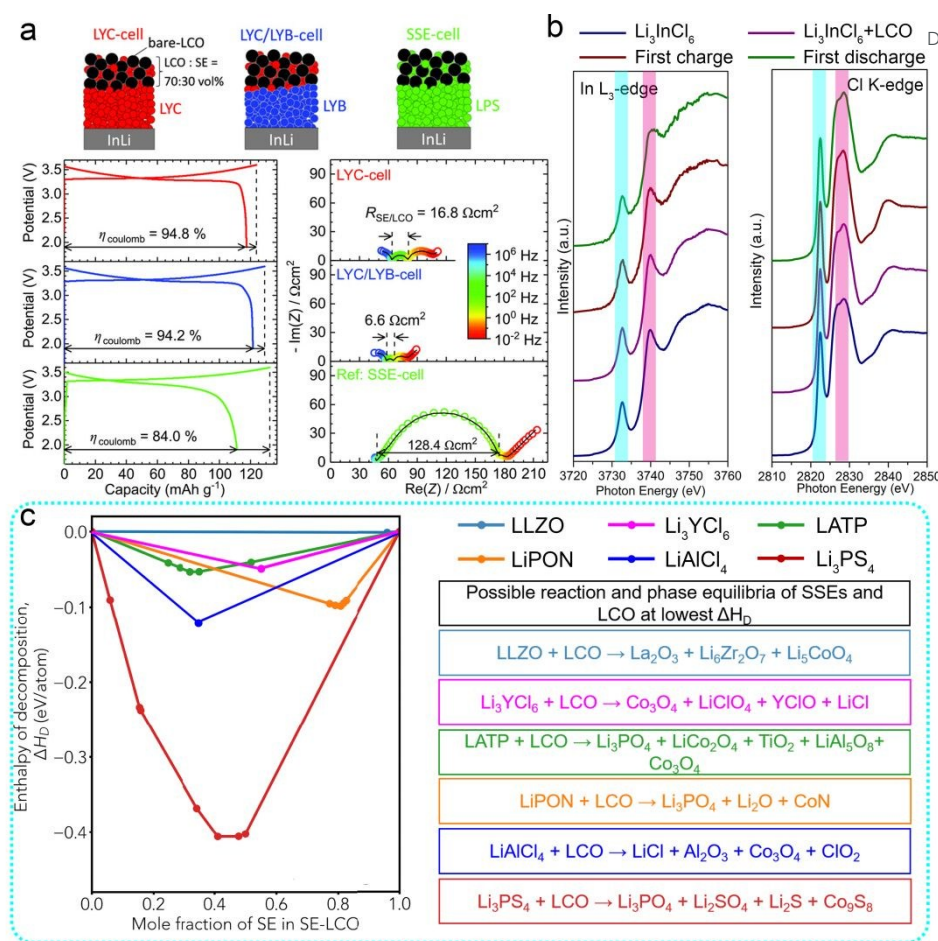


Figure 9. (a) Initial charge/discharge curves of bulk-type ASSLBs at 25 °C at 0.1 C, and corresponding Nyquist plots of the EIS spectra of ASSLBs after the first charging cycle. Reproduced with permission from ref. 14. Copyright (2018) Wiley. (b) In L₃-edge and Cl K-edge XANES spectra of pristine Li₃InCl₆, LiCoO₂-Li₃InCl₆ cathode composite, LiCoO₂-Li₃InCl₆ cathode composites collected after the first charge and after the first discharge. Reproduced with permission from ref. 15. Copyright (2019) Royal Society of Chemistry. (c) Calculated enthalpies of reaction between LCO and different types SSEs as a function of the mixing ratio of SSEs and phase equilibria (in box) with the largest magnitude of decomposition enthalpy. Reproduced with permission from ref. 17, 189. Copyright (2019) Wiley, Copyright (2018) Elsevier.

In most cases, halide SSEs exhibit good chemical stability toward oxide cathode materials based on experimental and theoretical results. Thin film type Li_xTiS₂/LiAlCl₄/Li_{1-x}CoO₂ ASSLBs with stable cycling performance over 150 cycles at 100 °C has been reported by W. K. Behl et al.³⁵ Though there is no detailed information of the stability between LiAlCl₄ SSE and electrodes, the good cycling

performance indicates good compatibility of LiAlCl_4 in the battery system. In the report of Li_3YCl_6 and Li_3YBr_6 SSEs, the author assembled bulk-type ASSLBs based on these two SSEs with bare LCO as the active component in cathode composites.¹⁴ The initial Coulombic efficiency of the Li_3YCl_6 -cell and Li_3YBr_6 -cell was as high as 94.8% and 94.2%, respectively, compared to that of 84% using Li_3PS_4 as SSEs (Figure 9a). Furthermore, the interfacial resistance between SSE and LCO after the first charging was 6.6-16.8 $\Omega \text{ cm}^{-2}$ when using Li_3YCl_6 and Li_3YBr_6 as SSEs compared to that of 128.4 $\Omega \text{ cm}^{-2}$ in the case of Li_3PS_4 SSE. The ASSLBs based on Li_3YCl_6 and Li_3YBr_6 SSEs also exhibit good cycling and rate performance as shown in their work. Thus, good chemical stability $\text{Li}_3\text{YCl}_6/\text{Li}_3\text{YBr}_6$ toward LiCoO_2 can be inferred from the electrochemical results. In addition, our group also assembled bulk-type ASSLBs based on Li_3InCl_6 SSE with bare LCO or bare NMC811 as active components in cathode composites.^{15, 16} Typically, the In L₃-edge and Cl K-edge X-ray absorption near-edge structure (XANES) spectra of pristine Li_3InCl_6 SSE, LiCoO_2 - Li_3InCl_6 cathode composites, and LiCoO_2 - Li_3InCl_6 cathode composites at different charge/discharge status remain unchanged as presented in Figure 9b. The results not only demonstrated the stability between Li_3InCl_6 and LiCoO_2 or its delithiated form (i.g. $\text{Li}_{0.5}\text{CoO}_2$) but also the electrochemical stability of Li_3InCl_6 even charge up to 4.2 V vs. Li/Li^+ .

The stabilities of different types of SSEs toward common oxide cathode materials of LiCoO_2 were systematically studied by theoretical calculations using the pseudo-binary model as shown in Figure 9c.^{17, 189} For the case of Li_3YCl_6 , the possible interfacial reaction energy of Li_3YCl_6 with LiCoO_2 or delithiated form $\text{Li}_{0.5}\text{CoO}_2$ is as small as < 45 meV/atom. The authors also calculated many other kinds of halide SSEs. Similarly, the possible interface energies for other types of halide SSEs (fluoride, chloride, bromide, and iodide) are also relatively small in the range of 0-164 meV/atom.¹⁷ As compared in Figure 9c, the value is comparable to that of LATP and LiPON, and significantly lower than sulfide type LPS. The results are consistent with the experimental results of high Coulombic efficiencies and cycling performance found in ASSLBs with Li_3YCl_6 - LiCoO_2 cathode without any

interfacial coatings. Nevertheless, the calculations may be misleading since the reaction energies are based on the formation of Co_3O_4 , LiClO_4 , YClO , and LiCl .¹⁷ In fact, LiClO_4 with Cl^{7+} valence state is difficult to form through the chemical reaction between Li_3YCl_6 and LiCoO_2 . A similar problem also can be found in their calculation for LiAlCl_4 , with ClO_2 (valence state of Cl^{4+}), which is one of the suggested reaction products (Figure 9c). Thus, further analysis of possible interfacial reactions between halide SSEs and oxide cathode materials is highly desired. In addition to the common oxide cathode materials, the stability toward sulfur or Li_2S type cathode materials should also be considered. However, related literatures have rarely been reported. Fundamental understanding of their compatibility needs to be developed before the application of halide SSEs in all-solid-state lithium-sulfur batteries.

4.3.2 Stability toward anodes

Lithium (Li) metal is the ideal anode for ASSLBs due to its extremely high theoretically capacity of 3860 mAh g^{-1} , the lowest negative electrochemical potential of -3.04 V vs. the standard hydrogen electrode, and low gravimetric density. However, due to the low electronegativity of Li, most SSEs with transition metal components will be reduced once contact with bare Li. Theoretically, there is no SSE that is thermodynamically stable with Li metal. Thus, the electrochemical reduction by Li is a common problem for most SSEs. Generally, SSEs have chemical/electrochemical instability against Li metal, inevitably causing unwanted side reactions at the interface. An interfacial layer will be formed between SSE and Li, which is similar to the “SEI” layer in liquid systems. The further reactions can be stopped if the interface between SSE and Li can be stabilized. In contrast, the reaction may be continuous and eventually lead to the increase of interfacial resistance as well as larger overpotential.

The different types of metal elements with high valence state make halide SSE unstable against bare Li. For example, the Li_3YCl_6 and Li_3YBr_6 SSEs can not come into direct contact with Li metal due to the reduction reactions, thus a LPS layer was inserted between Li_3YCl_6 or Li_3YBr_6 SSEs and Li metal during the cyclic voltammetry (CV) test.¹⁴ The $\text{Li}/\text{Li}_3\text{InCl}_6/\text{Au}$ cell also displayed Li plating

above 0 V vs. Li/Li⁺, which demonstrated that the Li₃InCl₆ is not stable towards Li metal.¹⁶ The reduction onset of various halide SSEs by Li is calculated based on the formation of LiX and reduced valent metal compounds and/or zero-valent metal by Yifei Mo et al. It seems that the reduction onset of halide SSEs is highly dependent on the metal component. For example, the Li₃MX₆ (X = F, Cl, Br) containing group 3 metal elements show reduction onset around 0.41-0.92 V vs. Li/Li⁺. Meanwhile, the value is much higher about 1.06-2.38 V vs. Li/Li⁺ for Li₃MX₆ (X = F, Cl, Br) with group 13 elements.¹⁷

To solve the problems associated with the anode materials, the assembled ASSLBs using SSEs mostly use lithium-alloy rather than bare Li metal as the anode, and Li-In alloy is the most popular choice.^{4, 6, 14, 190} However, the application of Li-In alloy as the anode significantly reduces the voltage of ASSLBs, leading to decreased energy density.¹⁹⁰ Nevertheless, there are many reported about the application of protected Li anodes (such as organic-inorganic nanocomposites-stabilized Li) and functional interlayers (such as plastic crystal electrolyte interlayer, alucone) to stabilize the interface between Li and SSEs^{191, 192}, which may also be applied for halide SSE systems. In addition, the combination with Li₃OX^{136, 137} or Li₃OHX¹³⁴ SSEs that stable toward Li metal would also be helpful. Further development of effective strategies needs to be investigated and developed.

4.4 Electrochemically stable window

One of the proposed advantages of SSEs is their extremely wide stable electrochemical windows of 0-5 V versus Li/Li⁺, which is usually confirmed by CV measurements on the Li/SSEs/Au blocking cell. It is claimed that the CV results can reflect the thermodynamic stability involving the reduction/oxidation reactions of the SSEs. However, with the fast development and evaluation of SSEs, many reports have pointed out the electrochemically stable windows for SSEs are actually overestimated by conventional CV measurements. The electrochemically stable window of Li₁₀GeP₂S₁₂ (LGPS),⁴ Li₂S-P₂S₅,^{164, 193} Li₆PS₅Cl (X=Cl, Br, I)¹⁹⁴ was reported to be up to 5 V tested by CV, while recent studies have confirmed that the mixture composites of those SSEs and conductive

carbon (SSEs/C) can be used as electrode materials in ASSBs, giving a reversible capacity around several hundreds of mAh g^{-1} .¹⁹⁵⁻¹⁹⁷ Furthermore, it has been shown that the carbon additives in cathode composites can trigger the decomposition of SSEs, especially at high working voltage.¹⁹⁸ The discrepancy between those results and CV testing is proposed to be due to the insufficient transport for electrons to match that of the migration of Li^+ .

First-principle calculations have been applied to predict the electrochemical stability window of SSEs by Yifei Mo and Gerbrand Ceder et al.^{186, 189} Theoretically, the electrochemical stability window is determined by the function of potential based on thermodynamic lithiation (reduction) and delithiation (oxidation) of SSEs. Their calculations results proposed that the thermodynamic electrochemical window of most sulfide-based SSEs (such as LGPS, Li_3PS_4 , $\text{Li}_7\text{PS}_{11}$, and $\text{Li}_6\text{PS}_5\text{Cl}$) show similarly narrow stability windows of 1.7-2.4 V vs. Li/Li^+ .

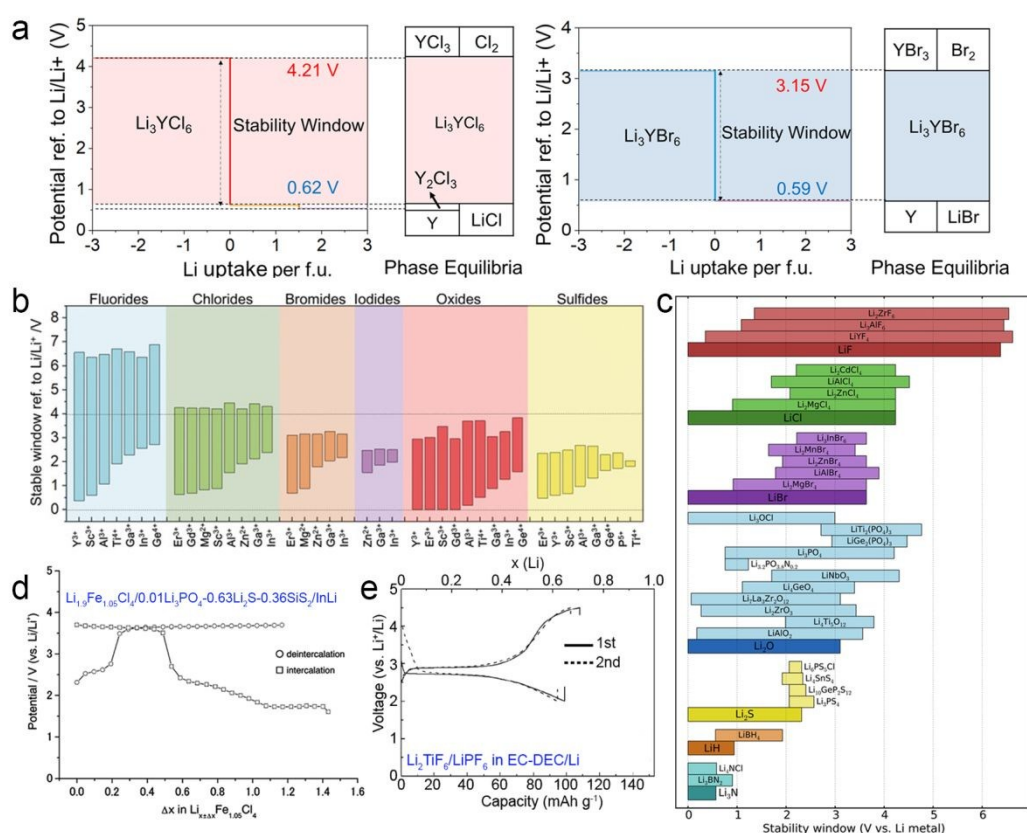


Figure 10. (a) Calculated thermodynamic equilibrium voltage profile and phase equilibria of Li_3YCl_6 and Li_3YBr_6 . Reproduced with permission from ref. 17. Copyright (2019) Wiley. (b) Calculated thermodynamics

intrinsic electrochemical window of Li-M-X ternary compounds in fluorides, chlorides, bromides, iodides, oxides and sulfides. M is a metal cation at its highest common valence state. Reproduced with permission from ref. 17. Copyright (2019) Wiley. (c) Calculated thermodynamics intrinsic electrochemical window of various electrolyte materials grouped by anion. Reproduced with permission from ref. 186. Copyright (2016) American Chemical Society. (d) Charge-discharge profiles of $\text{Li}_{1.9}\text{Fe}_{1.05}\text{Cl}_4/0.01\text{Li}_3\text{PO}_4\text{-}0.63\text{Li}_2\text{S-}0.36\text{SiS}_2/\text{InLi}$ ASSLBs. Reproduced with permission from ref. 199. Copyright (2002) Elsevier. (e) Galvanostatic discharge of $\text{Li}_2\text{TiF}_6/\text{LiPF}_6$ in EC-DEC/Li liquid cell at 0.2 mA cm^{-2} . Reproduced with permission from ref. 200. Copyright (2010) Japan Science and Technology Agency.

The upper limit of the stability window of Li_3YCl_6 and Li_3YBr_6 evaluated by Tetsuya Asano et al. was found to be about 4.5 V vs. Li/Li^+ using a cell configuration of SUS/SSE/LPS/Li.¹⁴ Bulk-type ASSBs with LiCoO_2 cathode cycled between 2.52-4.22 V vs. Li/Li^+ using these two SSEs were also proved to show high Coulombic Efficiency and good cycling performance. However, the synthesized Li_3YBr_6 can only be used as an SSE interlayer rather than in cathode composites. In contrast, Li_3YCl_6 can be used both in cathode composites and as an SSE interlayer.¹⁴ The failed ability to use Li_3YBr_6 SSE in a cathode mixture indicates that the Li_3YBr_6 SSE is actually unstable at high voltage compared to its chloride counterpart. This is further proved by the theoretical calculation results by Yifei Mo et al.¹⁷ Figure 10a shows the calculated thermodynamic equilibrium voltage plateaus for lithiation/delithiation reactions for Li_3YCl_6 and Li_3YBr_6 . In the case of Li_3YCl_6 , the lithiation plateau occurs at 0.62 V with Y^{3+} reduction, with the possible formation of Y_2Cl_3 , Y, and LiCl . The delithiation plateau at approximately 4.21 V corresponds to Cl^- oxidation reactions, with the possible formation of YCl_3 and Cl_2 . Therefore, the thermodynamic electrochemically stable window of Li_3YCl_6 is 0.62-4.21 V vs. Li/Li^+ , and the upper limit of the window is slightly lower than the 4.5 V measured by CV.¹⁴ In contrast, the calculated thermodynamic electrochemical window of Li_3YBr_6 is 0.59-3.15 V vs. Li/Li^+ , which is much narrower than that of measured using CV. This explains well why Li_3YBr_6 can not be used in a cathode layer.

As investigated by theoretical calculations, the thermodynamics electrochemical window of halide SSEs is highly dependent on the compositions. Figure 10b,c presents the general trend of electrochemical windows in some of Li-M-X ternary compounds ($M = \text{cation}$, $X = \text{F, Cl, Br, I, O, and S}$) and other SSEs systems.^{17, 186} Clearly, fluorides-based SSEs exhibit much higher oxidation stability, even over 6 V vs. Li/Li^+ , which is the best high voltage stability among all other halide SSEs. Nevertheless, there has been no reported fluoride-based SSEs with acceptable RT ionic conductivity ($10^{-3} \text{ S cm}^{-1}$) have been reported yet. On the other hand, chlorides-based SSEs also are quite promising, with oxidation potentials over 4 V vs. Li/Li^+ which meet the requirements of current Li-ion battery cathodes. In addition, there are several types of chloride-based SSEs (Li_3YCl_6 , Li_3InCl_6 , Li_3ErCl_6) that have been reported to exhibit high ionic conductivity. Comparatively, bromides and iodides exhibit narrower stability windows,^{17, 21} while the oxidation potential is still comparable to sulfides as shown in Figure 10b. As presented in Figure 10c, the upper stable window of typical LiCl and LiBr is estimated to be around 4 V vs. Li/Li^+ and is dominated by the anion oxidation of halide anions (Cl^- or Br^-). Promisingly, taking advantage of such anionic-redox reaction of halide anions, Chunsheng Wang et al. fabricated typical graphite intercalation compounds, i. e., $(\text{LiBr})_{0.5}(\text{LiCl})_{0.5}$ -graphite, as composite cathodes in aqueous LIBs.²⁰¹ Such $(\text{LiBr})_{0.5}(\text{LiCl})_{0.5}$ -graphite cathode exhibited average two distinct reaction voltage ranges, with 4.0-4.2 V for Br^- and 4.2-4.5 V for Cl^- . Further combining a graphite anode, the full cell can deliver quite a high energy density of 460 Wh kg^{-1} .

Furthermore, it is noticeable that some of the chloride and fluoride type SSEs (such as $\text{Li}_{2-x}\text{Fe}_{1+x}\text{Cl}_4$ ¹⁹⁹, Li_6VCl_8 ²⁰², Li_2MnCl_4 ,²⁰² and Li_xMF_y ($M = \text{Ti, V, Cr, Fe, Ni, Mn}$)^{200, 203-205}) also show redox reaction similar to sulfide SSEs,¹⁹⁵⁻¹⁹⁷ and thus can be used as cathode materials in solid-state lithium batteries and other battery systems. Akihisa Kajiyama et al. fabricated $\text{Li}_{1.9}\text{Fe}_{1.05}\text{Cl}_4/0.01\text{Li}_3\text{PO}_4-0.63\text{Li}_2\text{S}-0.36\text{SiS}_2/\text{InLi}$ ASSLBs, the charge/discharge profiles are shown in Figure 10d. It can be observed that a long plateau around 3.6 V vs. Li/Li^+ during charge (delithiation) process, corresponding to about 1.2 mol Li^+ ions extracted per formula unit of $\text{Li}_{1.9}\text{Fe}_{1.05}\text{Cl}_4$,

accompanied by oxidation of Fe^{2+} to Fe^{3+} .¹⁹⁹ John T. S. Irvine et al. also reported Li_2MnCl_4 and Li_6VCl_8 as cathode materials in primary Li thermal batteries, which showed discharge plateaus at ~ 2.5 V and 1.8 V vs. $\text{Li}/\text{Li}_{13}\text{Si}_4$ respectively, corresponding to the formation of LiCl and Mn or V as discharged products.²⁰² Thus, this kind of halide SSEs should not be suitable for ASSLBs due to the relatively easy redox reaction in quite narrow electrochemical windows. In most cases, the experimental electrochemical stability window of the SSEs are wider than the theoretical one. However, in some cases, the opposite results are obtained. For example, Li_2TiF_6 SSE, with a reported ionic conductivity of $2 \times 10^{-4} \text{ S cm}^{-1}$ at 300 °C, was calculated to show a wide electrochemically stable window of 1.9-6.71 V vs. Li/Li^+ . Shigeto Okada et al. demonstrated that Li_2TiF_6 can be used as an active cathode in liquid LIBs, with a discharge plateau at 2.7 V vs. Li/Li^+ and a reversible capacity around 100 mAh g^{-1} , as presented in Figure 10e.²⁰⁰ The results clearly demonstrated that Li_2TiF_6 SSE showed a significantly narrower electrochemical stability window than theoretically calculated values.

For halide SSEs with group 3 and group 13 elements, since the chemical state of non-Li cations is 3+ (which is the highest valence for these groups), the oxidation can only occur for halide anions. Thus, the electrochemical oxidation stability of those halide SSEs is largely determined by the oxidation of the halide anions. For halide SSEs with divalent metal elements, the oxidation can not only occur for halide anions, but also for those non-Li cations since they usually have multiple oxidation states (such as 2+, 3+, 4+). Thus, the oxidation of the metal cation in these type of halide SSEs can be reflected in the real electrochemical test if the oxidation potential of the metal cation is lower than that of the halide anion, such as the oxidation of Fe^{2+} to Fe^{3+} in the case of $\text{Li}_{1.9}\text{Fe}_{1.05}\text{Cl}_4$ as mentioned (Figure 10d). On the other hand, the electrochemical reduction stability of halide SSEs mainly originates from the reduction of non-Li cations due to the fact that the halide anions can not be further reduced (halide anions are already in the lowest chemical state). For example, from thermodynamic calculations, Li-M-X ternary compounds with Y^{3+} , Ga^{3+} , and Zn^{2+} cations exhibit the reduction of 0.36-0.62, 1.85-2.28, and 1.55-1.91 V vs. Li/Li^+ , respectively (Figure 10b,c).¹⁷ The halide

SSEs with group 3 element cations basically show the lowest reduction potentials compared to other types of cations. Thus, considering the potential ability to achieve higher oxidation as well as lower reduction voltages, halide SSEs with group 3 elements should be a better choice to provide more desirable electrochemical windows compared to other two types of halide SSEs.

Besides the further development of halide SSEs with high ionic conductivities, more attention should be put towards their chemical/electrochemical stabilities. The highly ignored structure instabilities of halide SSEs with temperature influence should get more attention since the structure-transition of SSEs might induce reduced ionic conductivities. Rational design of SSE compositions, such as the halide materials that possess reversible interconversion of hydrated forms, can be potential directions for developing halide SSEs with high humidity tolerance. Considering the stabilities toward electrode materials and electrochemical stability windows of halide SSEs, the engineering of stable interfaces between halide SSEs and Li anode seems to be imperative since most halide SSE containing non-Li cations can be readily reduced by Li metal. Moreover, limited works regarding the electrochemical stabilities of halide SSEs have been reported, and further experiments and analysis are highly needed to give deep insights into the real electrochemical stability windows of halide SSEs.

5. Applications of halide SSEs in energy storage

In the previous sections, we first introduced the development of halide SSEs. The various types of halide SSEs and their synthesis, as well as chemical/electrochemical stability, were further discussed. In this section, we will summarize the works related to the application of halide SSEs and their processability in different categories.

5.1 Applications of halide SSEs

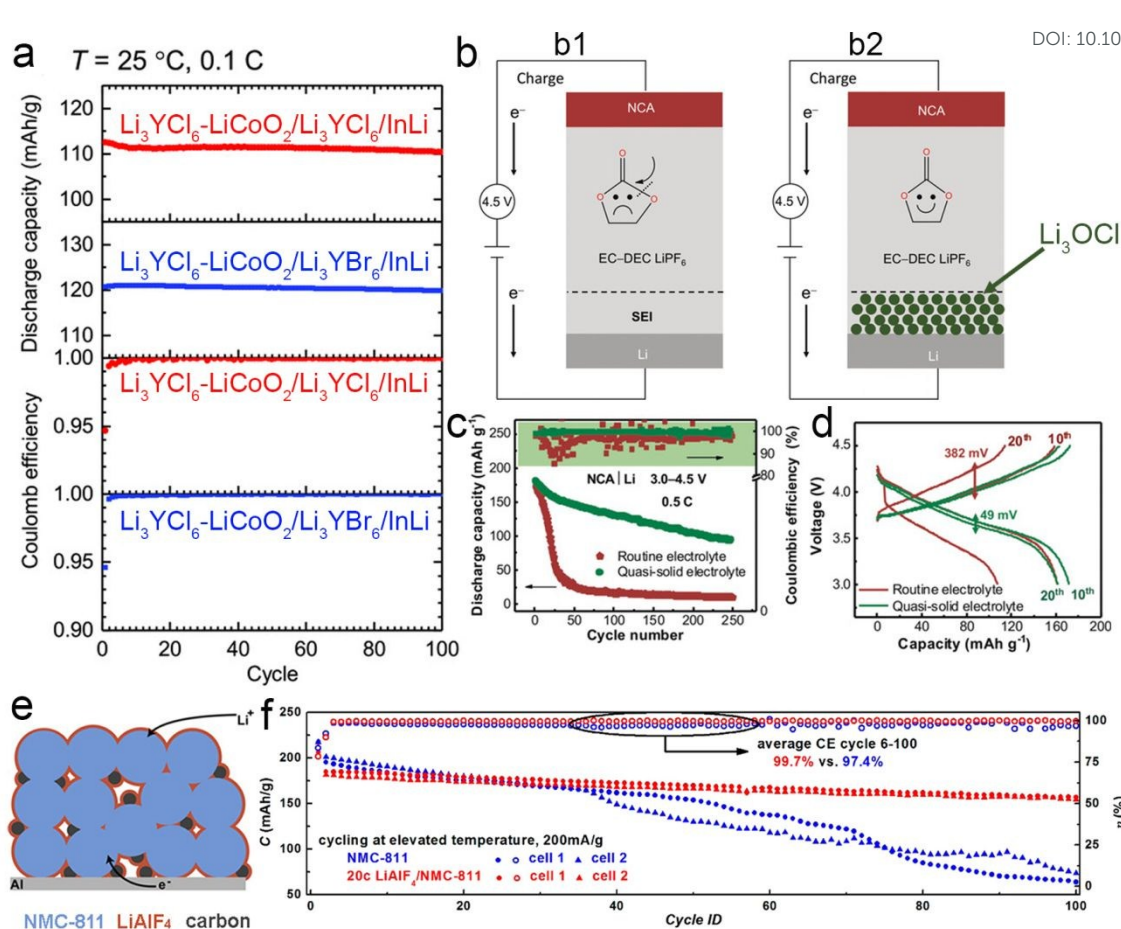


Figure 11. (a) The discharge capacity retention and coulombic efficiency of the $\text{Li}_3\text{YCl}_6\text{-LiCoO}_2/\text{Li}_3\text{YCl}_6/\text{InLi}$ and $\text{Li}_3\text{YCl}_6\text{-LiCoO}_2/\text{Li}_3\text{YBr}_6/\text{InLi}$ ASSLBs for 100 cycles. Reproduced with permission from ref. 14. Copyright (2018) Wiley. (b) Schematic of the influence of the reduced polarization on lithium metal anode. (b1) The solvent molecules in routine electrolyte decompose under 4.5 V high-voltage conditions. (b2) The Li_3OCl quasi-solid electrolyte layer that covers the lithium metal efficiently prohibits the decomposition of solvent molecules. Electrochemical performance of NCA|Li batteries. (c) The discharge capacity and Coulombic efficiency curves in routine and quasi-solid electrolytes, charge/discharge rate is 0.5 C and the voltage window is $3.0\text{--}4.5\text{ V}$. (d) Polarization voltage for different cycles. Reproduced with permission from ref. 206. Copyright (2019) Wiley. (e) Schematic illustration of LiAlF_4 coating on NMC811 cathode. (f) Cycle performance of pristine and 20-cycle-ALD LiAlF_4 coated NMC811 electrodes at $50\text{ }^{\circ}\text{C}$ at $2.75\text{--}4.50\text{ V}$ vs. Li/Li^+ . Reproduced with permission from ref. 157. Copyright (2017) American Chemical Society.

In view of the various of halide SSEs, they have many applications in different battery systems.

In terms of ASSLBs that are fabricated as a sandwiched structure including the anode layer, the SSE interlayer, and the cathode composite layer, halide SSEs are usually used as both SSE interlayer and ionic conductive components in the cathode composite layer. However, some halide SSEs are used just as an SSE interlayer due to concerns related to limited electrochemical stability windows. For example, as mentioned above, Tetsuya Asano et al. fabricated two kinds of $\text{Li}_3\text{YCl}_6\text{-LiCoO}_2/\text{Li}_3\text{YCl}_6/\text{InLi}$ and $\text{Li}_3\text{YCl}_6\text{-LiCoO}_2/\text{Li}_3\text{YBr}_6/\text{InLi}$ ASSLBs.¹⁴ Li_3YCl_6 can be used both in the SSE interlayer and cathode composites due to its high oxidation stability. In contrast, Li_3YBr_6 possesses a narrow electrochemically stable window (up to 3.15 V vs. Li/Li^+)¹⁷ and can only be used in the SSE interlayer (Figure 11a). The direct application of Li_3YBr_6 in cathode composite part may trigger its decomposition during cycling as proved in typical sulfide SSEs¹⁹⁵⁻¹⁹⁷, thus it should be careful and rational to choose appropriate SSEs for ASSLBs. In terms of halide SSEs that possess good compatibility toward Li metal, researchers have been trying to explore their potential applications in Li protection in liquid LIBs. As for typical Li_3OCl , its good compatibility toward Li metal was pointed out by both experimental and theoretical reports.^{136, 140} Jiaqi Huang et al. used Li_3OCl SSE together with a small amount of poly(vinylidene) fluoride (PVDF) to fabricate a Li_3OCl quasi-solid-state electrolyte layer on the surface of lithium anode to reduce the polarization of lithium anode in high-voltage liquid LIBs (Figure 11b).²⁰⁶ As shown in Figure 11c,d, the battery with Li_3OCl layer exhibited much higher reversible capacity, better cycling performance and smaller polarization compared to the battery without the Li_3OCl layer. It was demonstrated that the Li_3OCl quasi-solid-state interface can both reduce the polarization of lithium anode and enhance the Li^+ migration. Thus, benefiting from their Li^+ conductive property and good stability toward Li metal, these types of halide SSEs (Li_3OCl , Li_2OHCl , etc.) can also be used interlayer between Li anode and those SSEs that are unstable with Li to improve the total working voltage and energy density of ASSLBs. Another advantage of halide SSEs is their chemical stability toward oxide cathodes, which is a major issue for sulfide-type systems. Furthermore, some of halide SSEs exhibit wide electrochemical stability windows, especially

fluorides-types. Thus, halide SSEs are also can be used as coating layers on high-voltage oxide cathode materials. Yi Cui et al. coated LiAlF_4 on the surface of $\text{LiNi}_{0.8}\text{Mn}_{0.1}\text{Co}_{0.1}\text{O}_2$ (NMC811) electrodes by ALD approach (Figure 11e).¹⁵⁷ LiAlF_4 possesses a wide stable window from 2.0 ± 0.9 to 5.7 ± 0.7 V vs. Li/Li^+ and exhibited a RT ionic conductivity of $3.5 \pm 0.5 \times 10^{-8} \text{ S cm}^{-1}$. The stable and lithium ion conductive LiAlF_4 interfacial layer improved the stability of NMC811 electrodes cycled between 2.75-4.50 V vs. Li/Li^+ at 200 mA g^{-1} over 100 cycles (Figure 11f). Therefore, those halide SSEs are promising coating layers for oxide cathodes in different battery systems, which can not only avoid side reactions that trigger the destruction of oxide cathodes, but also can provide fast Li^+ migration within the cathodes. Of course, the premise is that these halide SSEs possess good chemical stability toward oxide cathodes as well as wide enough electrochemical stability window.

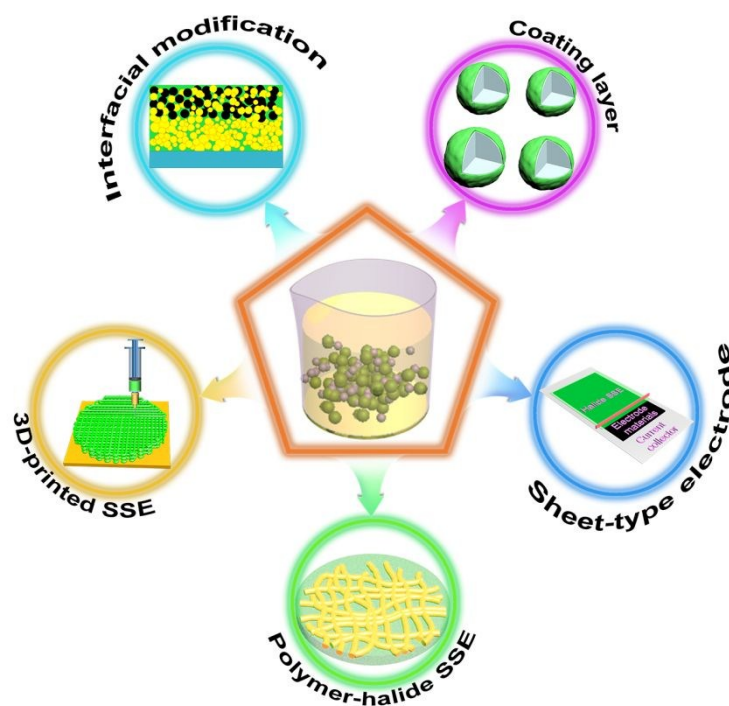


Figure 12. Potential liquid-processable applications of halide SSEs.

Moreover, halide SSEs possess the intrinsic advantage of solution processability, which leads to several different potential applications, especially for minimizing the interfacial resistance between electrode and electrolyte particles and the fabrication of thin SSE sheets. As presented in Figure 12, 1)

the liquid-phase synthesis of halide SSEs is useful for surface coating on cathode materials to form favorable electrode/electrolyte solid-solid interfaces, which can minimize the required amount of SSE in the cathode layer mixture; 2) solutions saturated with halide SSEs can also be infiltrated into the oxide SSEs particles to reduce grain boundary resistances; 3) it is possible to fabricate sheet-type electrode composites from active electrode material, binder, halide SSEs (or its raw materials), and carbon additives on the surface of current collectors for scalable fabrication processes; 4) the most prominent fabrication methods for SSEs layers are mainly based on cold-pressing strategies, thus the energy density is not too high due to the large thickness of the pressed pellets. The liquid-phase synthesis of halide SSEs can be further used to obtain quite thin SSE layers either by combining with a polymer matrix or by 3D printing using the halide SSE liquid with coagulating agents. Overall, all the aforementioned applications are highly dependent on the development of liquid-synthesis and solution-processable halide SSEs.

5.2 Evaluation of the energy density for halide-based solid-state lithium batteries

For the development of ASSLBs, their energy densities with different SSEs systems at cell level need to be evaluated based on practical parameters rather than just a rough estimation from cathode/anode active materials. Practically, to evaluate energy densities of batteries, the battery weight (or volume) includes everything from active materials (cathode and anode) and non-active materials (electrolyte, current collectors of Al/Cu foils, packaging materials, tabs, etc.) need to be considered. Thus, there's a large gap between real practical energy densities compared to theoretical values.²⁰⁷⁻²¹⁰

Herein, the gravimetric/volumetric energy densities of ASSLBs with practical parameters in a commercialized pouch cell for 4 common cathode/anode systems were evaluated, i. e., LiCoO₂ (LCO)/Li, Li(Li_{0.2}Mn_{0.54}Ni_{0.13}Co_{0.13})O₂ (Li-rich)/Li, LiNi_{0.8}Mn_{0.1}Co_{0.1}O₂ (NMC811)/Li, and S/Li. For the comparison of different SSE systems, four typical SSEs, including LGPS (sulfide), Li₃InCl₆ (halide), LLZO (oxide), and PEO (polymer) were chosen for the calculation of the corresponded gravimetric/volumetric energy densities of ASSLBs; another two halide SSEs (Li₃ScCl₆ and Li₃ErCl₆)

with different densities compared to Li_3InCl_6 were also evaluated. Detailed parameters of the selected electrode and SSE systems are listed in Table S1, S2.

Pouch cell was considered for the calculation of the energy densities due to its substantially higher energy values. The pouch-cell is built based on the lamination process by repeating units made of alternate layers of the cathode, SSE separator, Li-metal anode, with all materials packaged together. The calculations of ASSLBs energy densities in this review are mainly based on the calculation steps and parameters of Liquan Chen et al.²⁰⁷ The size of the pouch-cell is fixed at 138 mm \times 81.8 mm \times height (mm) (including lug and sealing edge), where the value of height varies with the SSEs thickness. A 16- μm aluminum (Al) current collector for the cathode and an 8- μm Cu foil for the anode are used. Table S3 lists the typical detailed cell parameters for constructing a 410.2 Wh/kg NMC811/Li pouch cell based on Li_3InCl_6 SSE. It should be noted that the compatibility of the selected SSEs with electrode materials are not considered for the calculation of energy densities here.

View Article Online

DOI: 10.1039/C9EE03828K

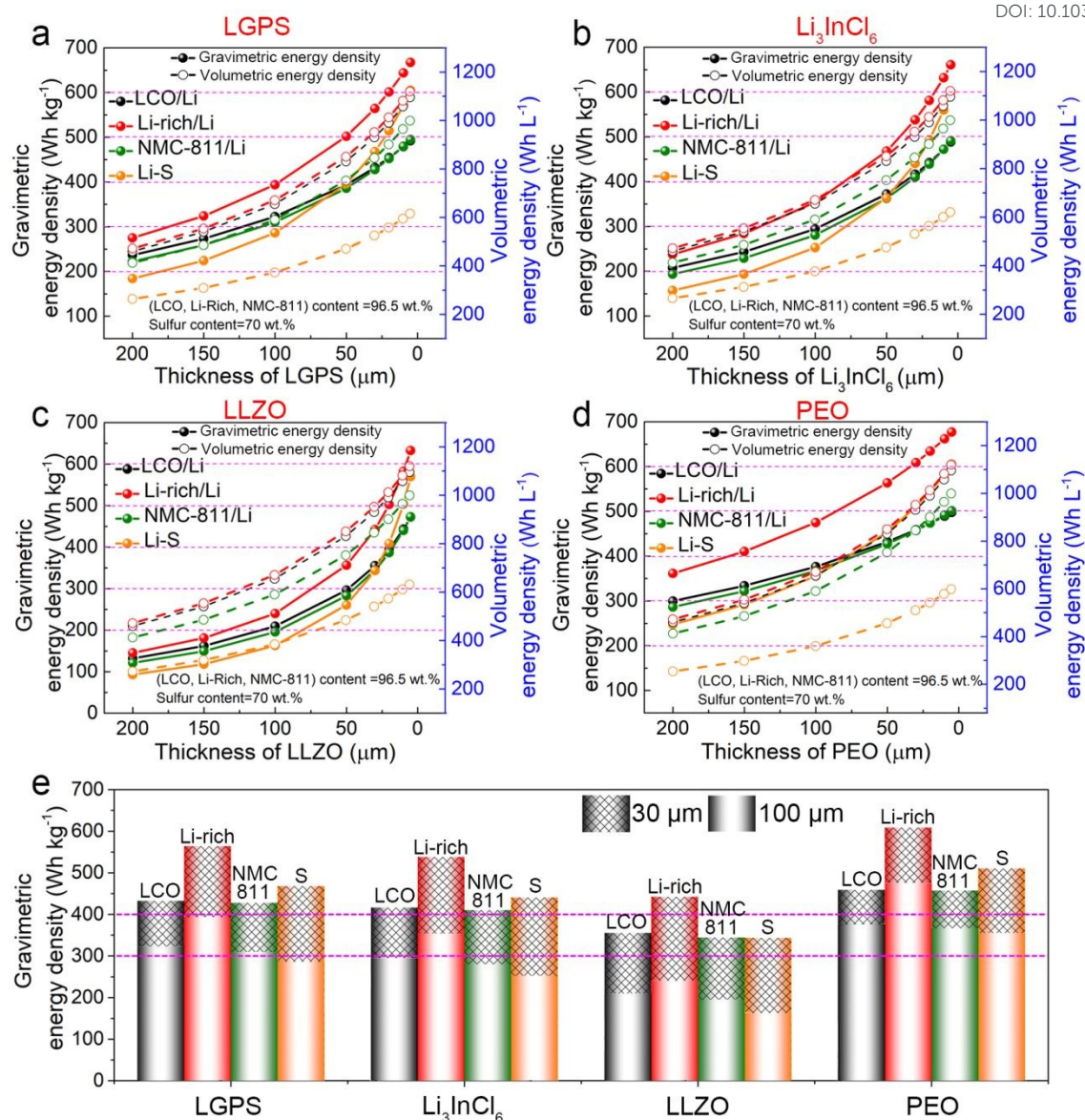


Figure 13. Gravimetric/volumetric energy densities of ASSLBs as a function of SSE thickness. (a) LGPS, (b) Li₃InCl₆, (c) LLZO, (d) PEO. (e) The gravimetric energy densities of ASSLBs based on two representative thicknesses (30 μm and 100 μm) of SSE; the black, red, green, and yellow colors refer to LCO, Li-rich, NMC811, and S cathodes, respectively. The weight percentage of the active materials is 96.5 wt% for LCO, Li-rich, and NMC811 cathodes and 70 wt% for S cathode. The calculation details are provided in the Supplemental Information.

The influence of the thickness of SSE layers on the final gravimetric/volumetric energy densities of the selected cathode/anode systems for Li₃InCl₆ as well as the other three kinds of SSEs (sulfide,

oxide, and polymer) are compared in Figure 13a-c. The weight percentage of LCO, Li-rich, and NMC811 active materials in electrodes was set as 96.5 wt%, 70 wt% in the case of S cathode, and 100 wt% in the case of Li metal anode. The N/P value here for Li metal anode was set as 2. The thickness of each cathode sheet was assumed to be 65.5 μm , thus the energy densities are dependent on the press density of the electrodes, weight percentage of active materials, and SSEs layers. Among the four selected cathode/anode systems, Li-rich/Li cell definitely exhibits the highest energy density with the same parameters since its higher capacity and voltage. Furthermore, the thickness of SSEs and their densities have pivotal impacts on the energy density of the cells. For example, as presented in Figure 13e, the reduction in thickness from 100 to 30 μm can increase the gravimetric energy density of NMC811/Li (with Li_3InCl_6 SSE) cells from 280.87 Wh kg^{-1} to 410.21 Wh kg^{-1} (590.32 Wh L^{-1} to 845.28 Wh L^{-1} for volumetric energy density). Moreover, the replacement of Li_3InCl_6 SSE to LLZO SSE with much higher density (5.07 g cm^{-3}) will decrease the gravimetric energy density of NMC811/Li cells from 410.21 Wh kg^{-1} to 344.35 Wh kg^{-1} if keep the same thicknesses of 30 μm . The gravimetric/volumetric energy densities of cells based on another two halide SSEs with different densities compared to Li_3InCl_6 (density: 2.18 g cm^{-3} for Li_3ScCl_6 , 3.07 g cm^{-3} for Li_3ErCl_6 , and 2.59 g cm^{-3} for Li_3InCl_6) were also calculated as shown in Figure S1. The values are highly agreement with the results showed in Figure 13, demonstrating the significant influences of the battery system, SSE density, and SSE thickness on the final gravimetric/volumetric energy densities. It is noteworthy that thin SSE layer (< 30 μm) can hardly be achieved. Haihui Wang et al. have successfully obtained a 25 μm free-standing ceramic $\text{Li}_{0.34}\text{La}_{0.56}\text{TiO}_3$ SSE film by tape-casting, which should be the thinnest free-standing SSE layer reported to date.²¹¹ Therefore, the processing of ultra-thin SSE layers is crucial to ensure their competitiveness of high-energy ASSLBs.

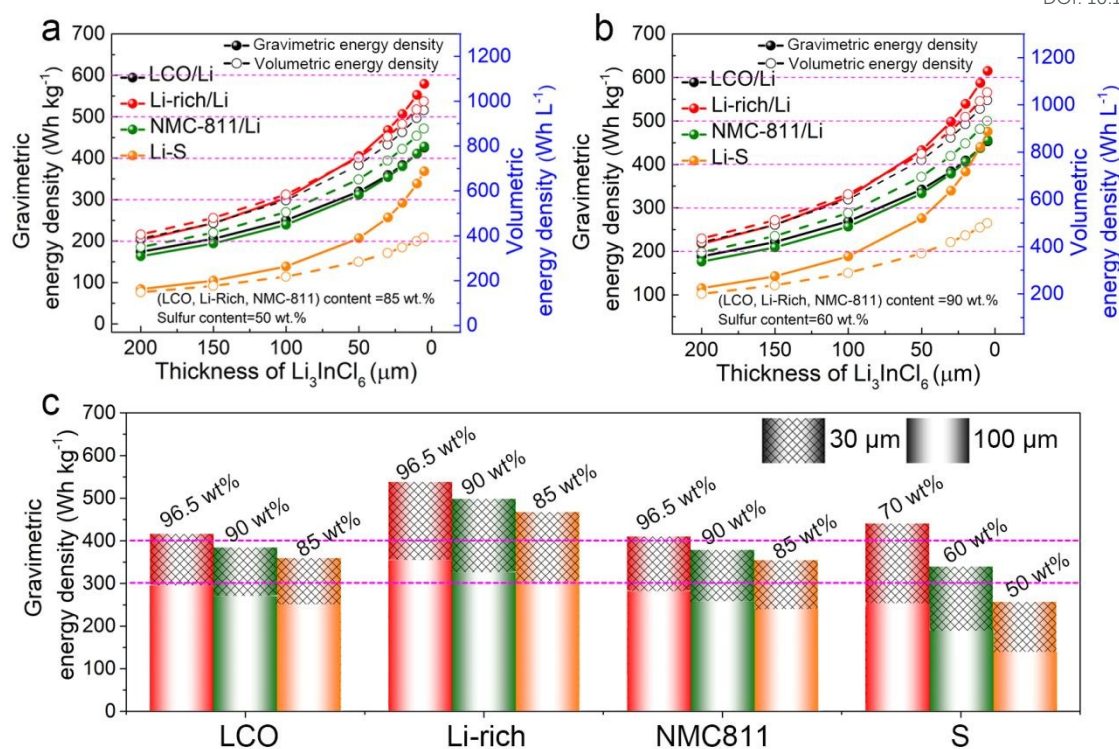


Figure 14. Gravimetric/volumetric energy densities of ASSLBs as a function of Li_3InCl_6 SSE thickness. (a) The weight percentage of the active materials is 85 wt% for LCO, Li-rich, and NMC811 cathodes and 50 wt% for S cathode, (b) the weight percentage of the active materials is 90 wt% for LCO, Li-rich, and NMC811 cathodes and 60 wt% for S cathode. (c) The gravimetric energy densities of ASSLBs based on two representative thicknesses (30 μm and 100 μm) of Li_3InCl_6 SSE; the red, green, and yellow colors refer to the highest, medium, and the lowest active material content. The calculation details are provided in the Supplemental Information.

Besides, as mentioned above, the weight percentage of active materials is also another significant influencing factor. The decrease of active material content will definitely reduce the energy density since the reduced area capacity and increased inactive components. Figure 14 shows the gravimetric/volumetric energy densities of the all-solid-state pouch cell with Li_3InCl_6 SSE with two lower active material contents (also as a function of SSE thickness). Typically, it can be seen that the lower active material contents of 90 wt% and 85 wt% can not reach 400 Wh kg^{-1} for LCO/Li cell based on Li_3InCl_6 , even the Li_3InCl_6 SSE thickness is only 30 μm . Similar results of other SSE systems are also compared in Figure S2-S6. However, the fact is that ASSLBs with high active cathode material

content over 90 wt% as well as good electrochemical performance are rarely achieved at the same time. Compared to liquid LIBs, larger amounts of conductive components need to be added into the electrode to ensure fast Li^+ /electron migration pathways due to the fact that the poor solid-solid contact among active material, SSEs particles, and conductive carbon additives. It should be noted that for sulfide and halide SSEs, newly emerged liquid-processable coating for electrode materials and fabricating of thin SSEs show more advantages in decreasing the inactive SSE content in ASSLBs.²¹²⁻

216

Besides those aforementioned parameters, there are still some other key issues need to be solved to realize the practical application of ASSLBs. For example, ASSLBs with polymer SSEs show the highest energy densities compared to other SSE systems since their lower density and easier fabrication of thin SSE layers. However, their relatively low ionic conductivity should also be considered. Furthermore, the most common issue for all SSEs should be paid more attention to is the compatibility between SSEs and electrodes (high-voltage oxides cathodes and Li metal anode).

In summary, first, the applications of halide SSEs are highly dependent on their chemical/electrochemical properties, especially their electrochemical stability windows. Second, recent advances of the liquid synthesis and solution-processable halide SSEs are also highly noteworthy as they open up the prospects of them being used for multiple applications. In addition, fabricating ultra-thin SSE layers and increasing the active electrode contents are of great importance to obtain high-performance halide-based ASSLBs. The compatibility of selected halide SSEs with electrode materials (particularly Li anode) is also a big challenge facing the application of halide SSEs in ASSLBs, which requires more effort in the near future.

6. Summary and Perspective

In this Review, we summarize the developments and understandings of halide SSEs for application in ASSLBs. First, halide Li_aMX_b SSEs, which include group 3 metal, group 13 elements,

and divalent elements (Zn, V, Fe, etc.) have been developed in the past years with different electrochemical properties. The structures of halide SSEs are mainly based on close-packed anion arrangements. Second, halide SSEs with high ionic conductivity have been synthesized by various strategies, especially the promising and scalable water-mediated synthesis route. Third, the chemical/electrochemical stabilities of halide SSEs are summarized and highlighted. Lastly, the application of halide SSEs is outlined in detail. Halide SSEs that generally present high ionic conductivity, high oxidation stability, and good stability toward oxide cathode materials are one of the most promising SSEs for application in ASSLBs.

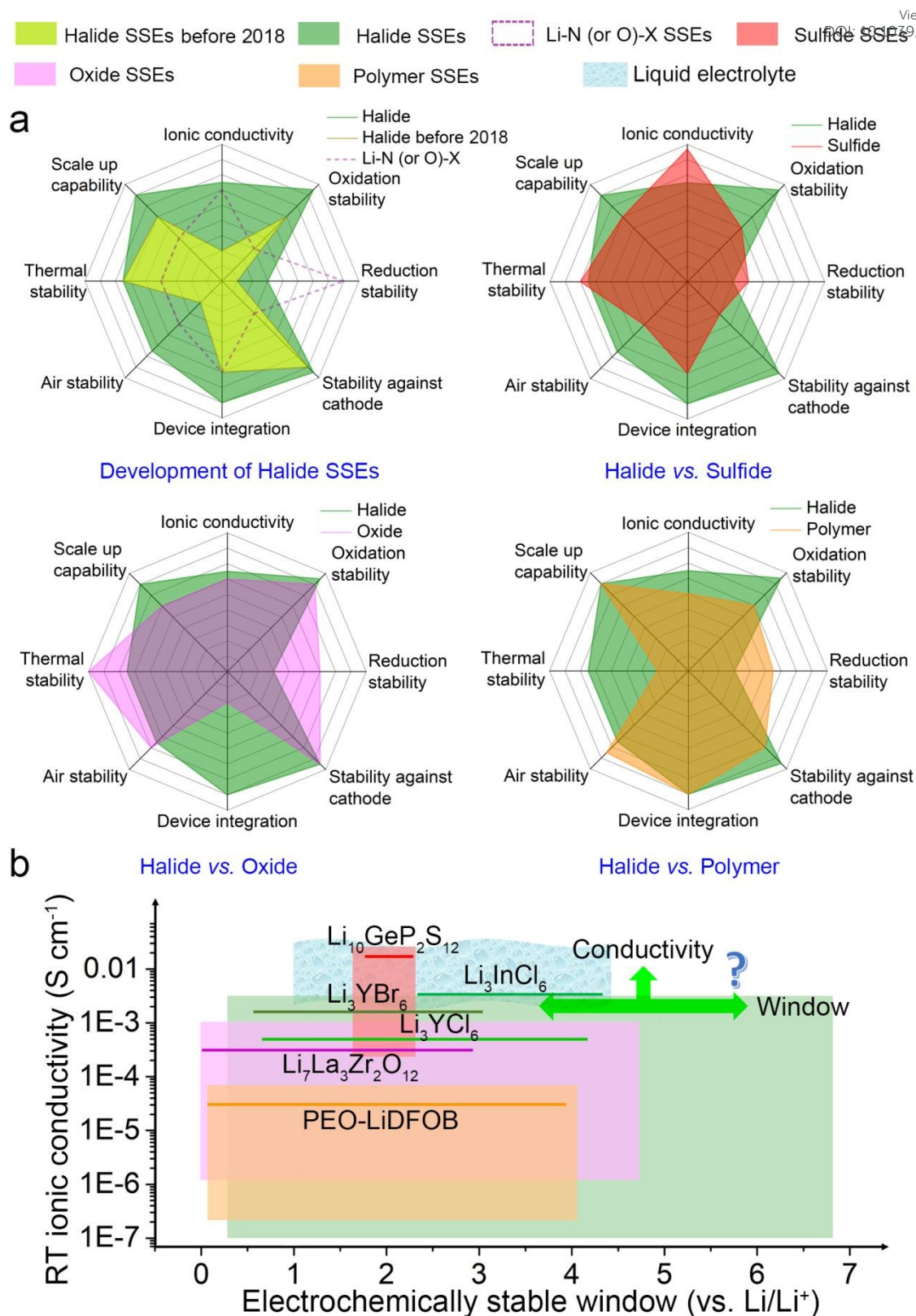


Figure 15. (a) Radar plots on the various properties of different types of SSEs. (b) RT ionic conductivity and electrochemically stable windows of different solid electrolytes. (LGPS,^{4, 186, 217} Li₃InCl₆,^{16,17} Li₃YBr₆,^{14, 17} Li₃YCl₆,^{14, 17} LLZO^{186, 218}, PEO-LiDFOB^{219, 220}) The intrinsic stability windows of oxide-, sulfide-, and halide

SSEs are based on the theoretical results of Gerbrand Ceder and Yifei Mo et al., and the value of polymer SSEs and liquid electrolytes are based on experimental values. The x-axis is the electrochemical stability windows of different kinds of SSEs and the y-axis represents the room-temperature ionic conductivities of the corresponding SSEs. The color of each rectangle corresponds to the different SSEs presented in the top of the figure, with green, red, purple, orange, and light blue stands for halide-, sulfide-, oxide-, polymer-, and liquid electrolytes, respectively.

The Radar plots of the different properties relevant to the development of halide SSEs and comparison with other SSEs are shown in Figure 15a. It is clear that both the ionic conductivity and air stability of halide SSEs dramatically improved since 2018. Furthermore, it is difficult to find a perfect SSEs that possesses all of the desired properties presented in the Radar plots. For sulfide SSEs, the severe air instability, low oxidation stability and unavoidable interfacial reaction with cathode materials hinder their application in ASSLBs. For oxide SSEs, the most egregious problem is their rigid mechanical properties that induce large grain boundary resistance among SSEs particles as well as interfacial resistance between oxide SSEs and electrodes. For polymer SSEs, the ionic conductivities are not high at room temperature, thus polymer-based ASSLBs require high operating temperatures or the addition of a small amount of liquid electrolyte to ensure fast Li^+ migration. Moreover, polymer SSEs also are not suitable for high voltage oxide cathode materials due to their oxidation at high voltage. For halide SSEs with metal elements, the poor reduction stability is the biggest issue due to the existence of high valence state metal elements. More specifically, the two key parameters of ionic conductivity and the electrochemical stability window of different types of SSEs are compared in Figure 15b. Though sulfide SSEs exhibit higher ionic conductivity compared to other SSEs, the narrow stable window restricts their application for high-energy battery systems. Due to the abundance of halide SSEs including various cations and anions, their potential stable windows are quite wide in theory, making them quite attractive and more deserving of in-depth attention.

Although promising results have been achieved using halide SSEs in ASSLBs, there are still challenges to be overcome and new properties to be developed in the future. The potential directions and perspectives are listed in detail as follows:

a) Improving the ionic conductivity of halide SSEs.

To date, only a few halide SSEs (e.g., Li_3YBr_6 and Li_3InCl_6) can experimentally exhibit RT ionic conductivity over $10^{-3} \text{ S cm}^{-1}$ that can enable operation of ASSLBs at ambient temperature with moderate current densities. Based on theoretical results, halide SSEs with trivalent metal elements, such as Li_3MX_6 ($\text{M} = \text{Sc}, \text{Y}, \text{Ho}, \text{Er}, \text{X} = \text{Cl}, \text{Br}$) might possess high ionic conductivity even up to $10^{-2} \text{ S cm}^{-1}$. The ionic conductivity of Li_3InCl_6 was also simulated to be as high as $6.4 \times 10^{-3} \text{ S cm}^{-1}$. Though there has been a gap between theoretical and experimental results, there should be significant room to further improve the ionic conductivity by optimizing the synthesis methods, vacancy content, lithium concentration, etc. On the other hand, halide SSEs with divalent metal elements may not be suitable regarding the narrower electrochemical stability windows. Furthermore, fluoride type SSEs are promising due to their high voltage stability, however, they possess significantly lower ionic conductivities. In this context, fluoride SSEs shall receive more attention in the near future. Moreover, the anion packing, ionic transport mechanism, and material design principles of halide SSEs are quite different from traditional design principles for other inorganic SSEs. Firstly, halide SSEs with high ionic conductivity is mainly achieved for those with ccp-like or hcp-like anion arrangements. Thus, Li^+ ions migrate among adjacent face-sharing Oct sites (Oct-Oct), or migrate through additional Tet interstitial sites between two Oct sites (Oct-Tet-Oct). These Li^+ pathways in halide SSEs are in contrast to traditional highly conducting SSEs where Li^+ ions transport via face-shared distorted Tet sites of a body-centered cubic (bcc)-like anion arrangement. Secondly, due to the fact that the halide SSEs can be regarded as composites of LiX and MX_a with M as a multivalent cation, halide SSEs consist of lots of intrinsic vacancies in their structures. Those intrinsic vacancies are believed to be essential to their high ionic conductivity by providing large numbers of sites for Li^+ migrations and there should be a

balance between vacancy content and Li^+ concentration. A better fundamental understanding and exploration of the Li^+ conductivity in SSEs structures by various advanced characterization techniques and simulations are urgently required to provide material design principles in order to achieve higher ionic conductivity.

b) Efficient synthesis strategies for halide SSEs.

Further efforts are required to develop simple and scalable synthesis methods for halide SSEs for industrial applications. For the preparation of halide SSE, high-energy ball-milling and high-temperature annealing are widely used. Comparatively, liquid-phase synthesis is more attractive due to the simplicity, quick synthesis times, homogeneous particle size, scalability, potential use as a coating layer and manufacturing for thin sheet SSEs. Nevertheless, only a few halide SSEs can be successfully synthesized by this strategy. Thus, obtaining novel halide SSEs through the liquid-phase synthesis route appears to be an interesting prospect. As aforementioned, the existence of various types of hydrated halide compounds can potentially provide effective synthesis routes to obtain targeted halide SSEs via dehydration procedures. However, a deeper and comprehensive understanding of the fundamental liquid chemistry and detailed reaction mechanisms is needed to provide further clarification. Further efforts are also required to extend the application of liquid-phase synthesis of halide SSEs to ASSLBs. The energy densities of ASSLBs are highly dependent on the thickness of SSEs layers and the weight percentage of active materials in the cathode part. The liquid-processable halide SSEs show obvious advantages in decreasing both the SSE thickness and content to fabricate bulk-type ASSLBs, which is important for improving the energy densities at the cell level.

c) Optimization of the electrochemical stability window of halide SSEs.

The electrochemically stable window of halide SSEs is highly dependent on the metal elements and anions. The oxidation onset voltage of halide SSEs is mainly dominated by the oxidation of the anions. Thus, the oxidation onset voltage of halide SSEs follows the order of

fluoride>chloride>bromide>iodine. Though the wide electrochemically stable window of fluoride-based SSEs can surpass 6 V vs. Li/Li⁺, the truth is that most fluoride-based SSEs exhibit quite low ionic conductivity due to the small radius of F⁻ anion. In contrast, iodine-based SSEs show the lowest oxidation onset voltage around 2 V vs. Li/Li⁺. The chloride-based SSEs are relatively more suitable with an acceptable oxidation onset over 4 V vs. Li/Li⁺ as well as high ionic conductivity over 10⁻³ S cm⁻¹. It should be noted that due to the kinetic limitations, the oxidation reactions of halide anions that lead to gas lease should occur at significantly higher potentials than the thermodynamic oxidation potential. Furthermore, the electrochemical oxidation stabilities of halide SSEs will also be influenced by the non-Li cations if there are higher oxidation states. In that case, the non-Li cations might be oxidized first at relatively lower potential than the oxidation of halide anions (such as Li₂MnCl₄, Li₆VCl₈). The oxidation of this type of SSEs has been confirmed in experimental studies and they are unable to provide a wide electrochemical stability windows compared to others.

The reduction onset voltage of halide SSEs is mainly dominated by the reduction of non-Li cations, and such reduction at low potential is the root cause for their instability toward Li anode. All the Li-M-X halide SSEs containing non-Li metal cations are thermodynamically unstable against Li metal with unavoidable side reactions at the interface. Generally, halide SSEs with group 3 element cations exhibit the lowest reduction potentials. Nevertheless, the detailed analysis of the halide SSEs/Li interfacial reaction is rarely reported and advanced techniques to investigate the buried halide SSEs/Li interfaces need to be developed. Moreover, effective strategies to stabilize the halide SSEs/Li interfaces should be further explored. Tuning the chemical composition of halide SSEs can alter the stability to some extent, especially in the case of LiF-enriched interface formation. In addition, lithium compounds that are thermodynamically stable against Li metal can be used as functional interlayers to protect halide SSEs from reduction by Li. In short, it's hard to find a perfect SSEs that possesses both high oxidation and low reduction voltages. Possible solutions might be the combination of multiple

SSEs compatible with their respective cathode and anode materials or the formation of stable interfacial layers at both cathode and anode sides to enable more electrochemically stable ASSLBs.

Even though the development of halide SSEs has been relatively slower than other SSEs and several issues need to be solved, promising approaches to solve these problems could draw inspiration from recent investigations in other SSEs systems. For example, further increase of the ionic conductivity by optimizing the vacancy concentration, or increasing the stability toward Li metal can be achieved by tuning the chemical composition or combining functional interlayers. Foreseeably, the opportunities and application of halide SSEs in ASSLBs will be addressed in the following years to come.

Acknowledgements

This research was supported by Natural Sciences and Engineering Research Council of Canada (NSERC), Canada Research Chair Program (CRC), Canada Foundation for Innovation (CFI), Ontario Research Fund, Canada MITACS fellow, and University of Western Ontario.

Declaration of interests

The authors declare no competing interests.

References

1. J.-M. Tarascon and M. Armand, in *Materials for Sustainable Energy: A Collection of Peer-Reviewed Research and Review Articles from Nature Publishing Group*, World Scientific, 2011, pp. 171-179.
2. A. Manthiram, X. Yu and S. Wang, *Nat. Rev. Mater.*, 2017, **2**, 16103.
3. J. C. Bachman, S. Muy, A. Grimaud, H.-H. Chang, N. Pour, S. F. Lux, O. Paschos, F. Maglia, S. Lupart and P. Lamp, *Chem. Rev.*, 2015, **116**, 140-162.
4. N. Kamaya, K. Homma, Y. Yamakawa, M. Hirayama, R. Kanno, M. Yonemura, T. Kamiyama, Y. Kato, S. Hama, K. Kawamoto and A. Mitsui, *Nat. Mater.*, 2011, **10**, 682.

5. Y. Kato, S. Hori, T. Saito, K. Suzuki, M. Hirayama, A. Mitsui, M. Yonemura, H. Iba and R. Kanno, *Nat. Energy*, 2016, **1**, 16030.
6. S. Choi, M. Jeon, B.-K. Kim, B.-I. Sang and H. Kim, *Chem. Commun.*, 2018, **54**, 14116-14119.
7. Y. Jin, K. Liu, J. Lang, D. Zhuo, Z. Huang, C.-a. Wang, H. Wu and Y. Cui, *Nat. Energy*, 2018, **3**, 732.
8. M. Monchak, T. Hupfer, A. Senyshyn, H. Boysen, D. Chernyshov, T. Hansen, K. G. Schell, E. C. Bucharsky, M. J. Hoffmann and H. Ehrenberg, *Inorg. Chem.*, 2016, **55**, 2941-2945.
9. S. Yu, R. D. Schmidt, R. Garcia-Mendez, E. Herbert, N. J. Dudley, J. B. Wolfenstine, J. Sakamoto and D. J. Siegel, *Chem. Mater.*, 2015, **28**, 197-206.
10. J. Liang, X. Li, Y. Zhao, L. V. Goncharova, G. Wang, K. R. Adair, C. Wang, R. Li, Y. Zhu and Y. Qian, *Adv. Mater.*, 2018, **30**, 1804684.
11. S. Kim, H. Oguchi, N. Toyama, T. Sato, S. Takagi, T. Otomo, D. Arunkumar, N. Kuwata, J. Kawamura and S.-i. Orimo, *Nat. Commun.*, 2019, **10**, 1081.
12. J. Cuan, Y. Zhou, T. Zhou, S. Ling, K. Rui, Z. Guo, H. Liu and X. Yu, *Adv. Mater.*, 2019, **31**, 1803533.
13. L. Nazar, P. Adeli, J. D. Bazak, K.-H. Park, I. Kochetkov, A. Huq and G. Goward, *Angew. Chem. Int. Ed.*, 2019, **58**, 8681-8686.
14. T. Asano, A. Sakai, S. Ouchi, M. Sakaida, A. Miyazaki and S. Hasegawa, *Adv. Mater.*, 2018, **30**, 1803075.
15. X. Li, J. Liang, J. Luo, M. Norouzi Banis, C. Wang, W. Li, S. Deng, C. Yu, F. Zhao, Y. Hu, T.-K. Sham, L. Zhang, S. Zhao, S. Lu, H. Huang, R. Li, K. R. Adair and X. Sun, *Energy Environ. Sci.*, 2019, **12**, 2665-2671.
16. X. Li, J. Liang, N. Chen, J. Luo, K. Adair, C. Wang, M. Norouzi Banis, T.-K. Sham, L. Zhang, S. Zhao, S. Lu, H. Huang, R. Li, and X. Sun, *Angew. Chem. Int. Ed.*, 2019, **58**, 16427-16432.
17. S. Wang, Q. Bai, A. M. Nolan, Y. Liu, S. Gong, Q. Sun and Y. Mo, *Angew. Chem. Int. Ed.*, 2019, **58**, 8039-8043.
18. A. D. Sendek, E. D. Cubuk, E. R. Antoniuk, G. Cheon, Y. Cui and E. J. Reed, *Chem. Mater.*, 2018, **31**, 342-352.
19. A. D. Sendek, Q. Yang, E. D. Cubuk, K.-A. N. Duerloo, Y. Cui and E. J. Reed, *Energy Environ. Sci.*, 2017, **10**, 306-320.
20. A. Zevgolits, B. C. Wood, Z. Mehmedović, A. T. Hall, T. C. Alves and N. Adelstein, *Appl. Mater.*, 2018, **6**, 047903.
21. Z. Xu, X. Chen, K. Liu, R. Chen, X. Zeng and H. Zhu, *Chem. Mater.*, 2019, **31**, 7425-7433.
22. D. Ginnings and T. Phipps, *J. Am. Chem. Soc.*, 1930, **52**, 1340-1345.
23. Y. Haven, *Recl. Trav. Chim. Pays-Bas*, 1950, **69**, 1471-1489.
24. B. Jackson and D. Young, *J. Phys. Chem. Solids*, 1969, **30**, 1973-1976.
25. C. R. Schlaikjer and C. C. Liang, *J. Electrochem. Soc.*, 1971, **118**, 1447-1450.
26. M. L. B. Rao, *U.S. Patent* No. 3,455,742. 15 Jul. 1969.
27. C. C. Liang, J. Epstein and G. H. Boyle, *J. Electrochem. Soc.*, 1969, **116**, 1452-1454.
28. C. C. Liang, *J. Electrochem. Soc.*, 1971, **118**, 894-895.

29. Y. Yamaguti and S. Sisido, *J. Chem. Soc. Japan*, 1941, **62**, 304-307.
30. L. Campanella and G. Pistoia, *J. Electrochem. Soc.*, 1973, **120**, 383-384.
31. J. J. Auborn, *U.S. Patent No.* 3,897,265. 29 Jul. 1975.
32. H. Venkatesetty and D. Saathoff, *J. Electrochem. Soc.*, 1981, **128**, 773-777.
33. W. Weppner and R. Huggins, *Physics Letters A*, 1976, **58**, 245-248.
34. W. Weppner and R. Huggins, *J. Electrochem. Soc.*, 1977, **124**, 35-38.
35. E. Plichta, W. Behl, D. Vujic, W. Chang and D. Schleich, *J. Electrochem. Soc.*, 1992, **139**, 1509-1513.
36. T. Oi and K. Miyauchi, *Mater. Res. Bull.*, 1981, **16**, 1281-1289.
37. T. Oi, *Mater. Res. Bull.*, 1984, **19**, 1343-1348.
38. T. Esaka, R. Okuyama and H. Iwahara, *Solid State Ionics*, 1989, **34**, 201-205.
39. R. Kanno, Y. Takeda, K. Takada and O. Yamamoto, *Solid State Ionics*, 1983, **9**, 153-156.
40. R. Kanno, Y. Takeda, K. Takada and O. Yamamoto, *J. Electrochem. Soc.*, 1984, **131**, 469-474.
41. H. D. Lutz, W. Schmidt and H. Haeuseler, *J. Phys. Chem. Solids*, 1981, **42**, 287-289.
42. Y. Tomita, A. Fuji-i, H. Ohki, K. Yamada and T. Okuda, *Chem. Lett.*, 1998, **27**, 223-224.
43. S. Muy, J. Voss, R. Schlem, R. Koerver, S. J. Sedlmaier, F. Maglia, P. Lamp, W. G. Zeier and Y. Shao-Horn, *iScience*, 2019, **16**, 270-282.
44. R. Schlem, S. Muy, N. Prinz, A. Banik, Y. Shao-Horn, M. Zobel and W. G. Zeier, *Adv. Energy Mater.*, 2019, DOI: 10.1002/aenm.201903719.
45. K.-H. Park, K. Kaup, A. Assoud, Q. Zhang, X. Wu and L. F. Nazar, *ACS Energy Lett.*, 2020, DOI: 10.1021/acseenergylett.9b02599.
46. S. Roman, B. Tim, L. Cheng, K. Marvin, M. Nicolo and Z. Wolfgang, *A Lattice Dynamical Approach for Finding the Lithium Superionic Conductor Li3ErI6*, *ChemRxiv*, 2020, doi:10.26434/chemrxiv.11627451.
47. A. Emly, E. Kioupakis and A. Van der Ven, *Chem. Mater.*, 2013, **25**, 4663-4670.
48. T. Oi, *Mater. Res. Bull.*, 1984, **19**, 451-457.
49. Y. Tomita, H. Matsushita, H. Yonekura, Y. Yamauchi, K. Yamada and K. Kobayashi, *Solid State Ionics*, 2004, **174**, 35-39.
50. Y. Tomita, H. Matsushita, K. Kobayashi, Y. Maeda and K. Yamada, *Solid State Ionics*, 2008, **179**, 867-870.
51. Y. Tomita, H. Nishiyama, K. Kobayashi, Y. Kohno, Y. Maeda and K. Yamada, *ECS Trans.*, 2009, **16**, 137-141.
52. K. Yamada, S. Matsuyama, Y. Tomita and Y. Yamane, *Solid State Ionics*, 2011, **189**, 7-12.
53. Y. Tomita, H. Ohki, K. Yamada and T. Okuda, *Solid State Ionics*, 2000, **136**, 351-355.
54. A. Pfitzner, J. K. Crockett, I. Solinas and H. D. Lutz, *Z. Anorg. Allg. Chem.*, 1993, **619**, 993-998.
55. C. Cros, L. Hanebali, L. Latie and W. Gang, *Solid State Ionics*, 1983, **9**, 139-147.
56. R. D. Shannon, *Acta Crystallogr., Sect. A: Cryst. Phys. Diff., Theor. Gen. Crystallogr.*, 1976, **32**, 751-767.
57. A. Tyagi, J. Köhler, P. Balog and J. Weber, *J. Solid State Chem.*, 2005, **178**, 2620-2625.
58. B. Choi, B. Moon, H. Seo, J. Jeong, H. Lee and W. Seo, *Mater. Design*, 2000, **21**, 567-570.

View Article Online
DOI: 10.1039/C9EE03828K

59. A. Bohnsack, F. Stenzel, A. Zajonc, G. Balzer, M. S. Wickleder and G. Meyer, *Z. Anorg. Allg. Chem.*, 1997, **623**, 1067-1073. View Article Online
DOI: 10.1039/CP97E03828K
60. A. Lachgar, D. S. Dudis, P. K. Dorhout and J. D. Corbett, *Inorg. Chem.*, 1991, **30**, 3321-3326.
61. H.-J. Steiner and H. D. Lutz, *Z. Anorg. Allg. Chem.*, 1992, **613**, 26-30.
62. A. Bohnsack, G. Balzer, H. U. Güdel, M. S. Wickleder and G. Meyer, *Z. Anorg. Allg. Chem.*, 1997, **623**, 1352-1356.
63. A. Delaigue and J. Cousseins, *Rev. Chim. Miner.*, 1972, **9**, 789.
64. K. Feldner and R. Hoppe, *Rev. Chim. Miner.*, 1983, **20**, 351.
65. D. Klimm, I. A. Dos Santos, I. M. Ranieri and S. L. Baldochi, *MRS Online Proceedings Library Archive*, 2008, **1111**, D01-07.
66. A. Grzechnik, W. A. Crichton, P. Bouvier, V. Dmitriev, H.-P. Weber and J.-Y. Gesland, *J. Phys. Condens. Matter*, 2004, **16**, 7779.
67. J. E. Ford, G. Meyer and J. D. Corbett, *Inorg. Chem.*, 1984, **23**, 2094-2098.
68. G. Meyer and T. Schleid, *Inorg. Chem.*, 1987, **26**, 217-218.
69. M. El-Ghozzi and D. Avignant, *J. Fluor. Chem.*, 2001, **107**, 229-233.
70. M. EL - GHOZZI, D. Avignant and J. Cousseins, *ChemInform*, 1993, **24**, no-no.
71. N. Garg, A. Mishra, H. Poswal, A. Tyagi and S. M. Sharma, *J. Solid State Chem.*, 2015, **229**, 164-172.
72. N. Sorokin, D. Karimov and O. Komar'kova, *Crystallogr. Rep.*, 2010, **55**, 448-449.
73. A. Rakhmatullin, I. B. Polovov, D. Maltsev, M. Allix, V. Volkovich, A. V. Chukin, M. Boča and C. Bessada, *Inorg. Chem.*, 2018, **57**, 1184-1195.
74. B. Kubíková, J. Mlynáriková, O. Beneš, E. Mikšíková, J. Prišćák, A. Tosolin and M. Boča, *J. Mol. Liq.*, 2018, **268**, 754-761.
75. V. Trnovcová, P. P. Fedorov and I. Furár, *Russ. J. Electrochem.*, 2009, **45**, 630-639.
76. F. Altorfer, *Investigations into the fast ionic conductors γ -CuBr, Li 2 S, Na 2 S, Ba 2 NH, NaTaN 2 and Li 3 HoCl 6 by means of neutron scattering*, Eidgenoessische Technische Hochschule, 1994, **25**, LNS--171.
77. S. Siekierski, *J. Inorg. Nucl. Chem.*, 1971, **33**, 377-386.
78. M. A. Kraft, S. Ohno, T. Zinkevich, R. Koerver, S. P. Culver, T. Fuchs, A. Senyshyn, S. Indris, B. J. Morgan and W. G. Zeier, *J. Am. Chem. Soc.*, 2018, **140**, 16330-16339.
79. S.-H. Bo, Y. Wang, J. C. Kim, W. D. Richards and G. Ceder, *Chem. Mater.*, 2016, **28**, 252-258.
80. C. K. Moon, H.-J. Lee, K. H. Park, H. Kwak, J. W. Heo, K. Choi, H. Yang, M.-S. Kim, S.-T. Hong and J. H. Lee, *ACS Energy Lett.*, 2018, **3**, 2504-2512.
81. Y. Wang, W. D. Richards, S. P. Ong, L. J. Miara, J. C. Kim, Y. Mo and G. Ceder, *Nat. Mater.*, 2015, **14**, 1026.
82. W. Hönle, B. Hettich and A. Simon, *Z. Naturforsch. B*, 1987, **42**, 248-250.
83. W. Hönle, G. Miller and A. Simon, *J. Solid State Chem.*, 1988, **75**, 147-155.
84. W. Hönle and A. Simon, *Z. Naturforsch. B*, 1986, **41**, 1391-1398.

85. J. H. Burns, A. C. Tennissen and G. D. Brunton, *Acta Crystallogr., Sect. B: Struct. Crystallogr. Cryst. Chem.*, 1968, **24**, 225-230.
86. G. Garton and B. Wanklyn, *J. Inorg. Nucl. Chem.*, 1965, **27**, 2466-2469.
87. J. Köhler and A. Tyagi, *Z. Kristallogr. - New Cryst. Struct.*, 1999, **214**, 25-26.
88. R. Miyazaki and H. Maekawa, *ECS Electrochem. Lett.*, 2012, **1**, A87-A89.
89. Y. Lee, D. M. Piper, A. S. Cavanagh, M. J. Young, S.-H. Lee and S. M. George, 2017, DOI: 10.26434/chemrxiv.5459653.v1.
90. M. Feinauer, H. Euchner, M. Fichtner and M. Anji Reddy, *ACS Appl. Energy Mater.*, 2019, **2**, 7196-7203.
91. K. Yamada, K. Kumano and T. Okuda, *Solid State Ionics*, 2006, **177**, 1691-1695.
92. K. Yamada, K. Iwaki, T. Okuda and Y. Tomita, in *Solid State Ionics: Trends in the New Millennium*, World Scientific, 2002, pp. 621-628.
93. Y. Tomita, H. Matsushita, Y. Maeda, K. Kobayashi and K. Yamada, 2005, Trans Tech Publ, pp. 17-26.
94. Y. Tomita, H. Yonekura, Y. Yamauchi, K. Yamada and K. Kobayashi, *Z. Naturforsch. A*, 2002, **57**, 447-450.
95. Y. Tomita, H. Matsushita, K. Kobayashi and K. Yamada, in *Solid State Ionics: The Science and Technology of Ions in Motion*, World Scientific, 2004, pp. 985-990.
96. A. Zevgolis, A. Hall, T. Alvez, Z. Mehmedovic, P. Shea, J. Varley, B. Wood and N. Adelstein, *Subcontract Report: Diffusion Mechanisms and Bond Dynamics in Solid Electrolyte Ion-Conductors*, Lawrence Livermore National Lab.(LLNL), Livermore, CA (United States), 2017.
97. N. Adelstein and B. C. Wood, *Chem. Mater.*, 2016, **28**, 7218-7231.
98. R. Kanno, Y. Takeda, M. Mori and O. Yamamoto, *Chem. Lett.*, 1989, **18**, 223-226.
99. A. Pfitzner, H. Lutz and J. Cockcroft, *J. Solid State Chem.*, 1990, **87**, 463-466.
100. R. Kanno, Y. Takeda and O. Yamamoto, *Solid State Ionics*, 1988, **28**, 1276-1281.
101. P. Kuske, W. Schäfer and H. D. Lutz, *Mater. Res. Bull.*, 1988, **23**, 1805-1808.
102. R. Kanno, Y. Takeda, A. Matsumoto, O. Yamamoto, R. Suyama and S. Kume, *J. Solid State Chem.*, 1988, **75**, 41-51.
103. R. Kanno, Y. Takeda, A. Takahashi, O. Yamamoto, R. Suyama and S. Kume, *J. Solid State Chem.*, 1987, **71**, 196-204.
104. H. Lutz, P. Kuske and K. Wussow, *Naturwiss.*, 1986, **73**, 623-623.
105. R. Kanno, Y. Takeda and O. Yamamoto, *Mater. Res. Bull.*, 1981, **16**, 999-1005.
106. C. Wickel, Z. Zhang and H. D. Lutz, *Z. Anorg. Allg. Chem.*, 1994, **620**, 1537-1542.
107. W. Schmidt and H. Lutz, *Ber. Bunsen Ges. Phys. Chem.*, 1984, **88**, 720-723.
108. R. Kanno, Y. Takeda, O. Yamamoto, C. Cros, W. Gang and P. Hagenmuller, *Solid State Ionics*, 1986, **20**, 99-103.
109. R. Kanno, Y. Takeda, A. Takahashi, O. Yamamoto, R. Suyama and S. Kume, *J. Solid State Chem.*, 1988, **72**, 363-375.
110. R. Kanno, Y. Takeda, M. Mori and O. Yamamoto, *Chem. Lett.*, 1987, **16**, 1465-1468.

111. H. D. Lutz, P. Kuske and K. Wussow, *Z. Anorg. Allg. Chem.*, 1987, **553**, 172-178. View Article Online
DOI: 10.1039/C9EE03828K
112. R. Kanno, Y. Takeda, A. Takahashi, O. Yamamoto, R. Suyama and M. Koizumi, *J. Solid State Chem.*, 1987, **71**, 189-195.
113. H. Lutz, Z. Zhang and A. Pfitzner, *Solid State Ionics*, 1993, **62**, 1-3.
114. H. Lutz, A. Pfitzner and C. Wickel, *Solid State Ionics*, 1991, **48**, 131-138.
115. J. L. Soubeyroux, C. Cros, W. Gang, R. Kanno and M. Pouchard, *Solid State Ionics*, 1985, **15**, 293-300.
116. H. Lutz, A. Pfitzner and J. Cockcroft, *J. Solid State Chem.*, 1993, **107**, 245-249.
117. M. Schneider, H. Lutz and J. Cockcroft, *Z. Krist.-Cryst. Mater.*, 1993, **203**, 183-198.
118. M. Partik, C. Wickel, H. Lutz and T. Roisnel, *J. Solid State Chem.*, 1996, **124**, 292-299.
119. M. Schneider, P. Kuske and H. D. Lutz, *Z. Naturforsch. B*, 1993, **48**, 1-6.
120. H. C. Gupta, J. Zwinscher and H. D. Lutz, *J. Phys. Chem. Solids*, 1997, **58**, 173-175.
121. L. Hanebali, T. Machej, C. Cros and P. Hagemuller, *Mater. Res. Bull.*, 1981, **16**, 887-901.
122. G. Villeneuve, L. Latié, C. Cros and P. Hagemuller, *Mater. Res. Bull.*, 1984, **19**, 1515-1526.
123. P. Hartwig, W. Weppner and W. Wichelhaus, *Mater. Res. Bull.*, 1979, **14**, 493-498.
124. P. Hartwig, W. Weppner, W. Wichelhaus and A. Rabenau, *Angew. Chem. Int. Ed.*, 1980, **19**, 74-75.
125. M. Howard, O. Clemens, P. Slater and P. Anderson, *J. Alloy. Compd.*, 2015, **645**, S174-S177.
126. W. Weppner, P. Hartwig and A. Rabenau, *J. Power Sources*, 1981, **6**, 251-259.
127. H. Obayashi, A. Gotoh and R. Nagai, *Mater. Res. Bull.*, 1981, **16**, 581-585.
128. S. Li, J. Zhu, Y. Wang, J. W. Howard, X. Lü, Y. Li, R. S. Kumar, L. Wang, L. L. Daemen and Y. Zhao, *Solid State Ionics*, 2016, **284**, 14-19.
129. Y. Zhao and L. L. Daemen, *J. Am. Chem. Soc.*, 2012, **134**, 15042-15047.
130. R. Mouta, E. Diniz and C. Paschoal, *J. Mater. Chem. A*, 2016, **4**, 1586-1590.
131. P. Hartwig, A. Rabenau and W. Weppner, *J. Less Common Met.*, 1981, **78**, 227-233.
132. G. Schwering, A. Hönnerscheid, L. van Wüllen and M. Jansen, *ChemPhysChem*, 2003, **4**, 343-348.
133. Y. Li, W. Zhou, S. Xin, S. Li, J. Zhu, X. Lü, Z. Cui, Q. Jia, J. Zhou, Y. Zhao and J. B. Goodenough, *Angew. Chem. Int. Ed.*, 2016, **55**, 9965-9968.
134. Z. D. Hood, H. Wang, A. Samuthira Pandian, J. K. Keum and C. Liang, *J. Am. Chem. Soc.*, 2016, **138**, 1768-1771.
135. J. Zhang, J. Han, J. Zhu, Z. Lin, M. H. Braga, L. L. Daemen, L. Wang and Y. Zhao, *Inorg. Chem. Commun.*, 2014, **48**, 140-143.
136. X. Lü, G. Wu, J. W. Howard, A. Chen, Y. Zhao, L. L. Daemen and Q. Jia, *Chem. Commun.*, 2014, **50**, 11520-11522.
137. X. Lü, J. W. Howard, A. Chen, J. Zhu, S. Li, G. Wu, P. Dowden, H. Xu, Y. Zhao and Q. Jia, *Adv. Sci.*, 2016, **3**, 1500359.
138. H. Fang and P. Jena, *Proc. Natl. Acad. Sci.*, 2017, **114**, 11046-11051.
139. Z. Wang, H. Xu, M. Xuan and G. Shao, *J. Mater. Chem. A*, 2018, **6**, 73-83.
140. M. Dondelinger, J. Swanson, G. Nasymov, C. Jahnke, Q. Qiao, J. Wu, C. Widener, A. M. Numan-Al-Mobin and A. Smirnova, *Electrochim. Acta*, 2019, **306**, 498-505.

141. Y. Zhang, Y. Zhao and C. Chen, *Phys. Rev. B*, 2013, **87**, 134303.
142. R. Mouta, M. A. B. Melo, E. M. Diniz and C. W. A. Paschoal, *Chem. Mater.*, 2014, **26**, 7137-7144.
143. A.-Y. Song, Y. Xiao, K. Turcheniuk, P. Upadhyay, A. Ramanujapuram, J. Benson, A. Magasinski, M. Olguin, L. Meda, O. Borodin and G. Yushin, *Adv. Energy Mater.*, 2018, **8**, 1700971.
144. M. H. Braga, A. J. Murchison, J. A. Ferreira, P. Singh and J. B. Goodenough, *Energy Environ. Sci.*, 2016, **9**, 948-954.
145. M. Braga, J. A. Ferreira, V. Stockhausen, J. Oliveira and A. El-Azab, *J. Mater. Chem. A*, 2014, **2**, 5470-5480.
146. J. A. Dawson, T. S. Attari, H. Chen, S. P. Emge, K. E. Johnston and M. S. Islam, *Energy Environ. Sci.*, 2018, **11**, 2993-3002.
147. H. H. Heenen, J. Voss, C. Scheurer, K. Reuter and A. C. Luntz, *J. Phys. Chem. Lett.*, 2019, **10**, 2264-2269.
148. I. Hanghofer, G. n. J. Redhammer, S. Rohde, I. Hanzu, A. Senyshyn, H. M. R. Wilkening and D. Rettenwander, *Chem. Mater.*, 2018, **30**, 8134-8144.
149. Y. Yu, Z. Wang and G. Shao, *J. Mater. Chem. A*, 2018, **6**, 19843-19852.
150. H. Xu, M. Xuan, W. Xiao, Y. Shen, Z. Li, Z. Wang, J. Hu and G. Shao, *ACS Appl. Energy Mater.*, 2019, **2**, 6288-6294.
151. T. Asai, S. Kawai, R. Nagai and S. Mochizuki, *J. Phys. Chem. Solids*, 1984, **45**, 173-179.
152. J. W. Howard, 2014, UNLV Theses, Dissertations, Professional Papers, and Capstones. 2269.
153. J. Zhu, S. Li, Y. Zhang, J. W. Howard, X. Lü, Y. Li, Y. Wang, R. S. Kumar, L. Wang and Y. Zhao, *Appl. Phys. Lett.*, 2016, **109**, 101904.
154. L.-H. Yin, H. Yuan, L. Kong, Z.-G. Lu and Y. Zhao, *Chem. Commun.*, 2020, DOI: 10.1039/C9CC08382K.
155. W. Choi, A. Benayard, J.-H. Park, J. Park, S.-G. Doo and J. Mun, *Electrochim. Acta*, 2014, **117**, 492-497.
156. J. Hu, K. Chen and C. Li, *ACS Appl. Mater. Interfaces*, 2018, **10**, 34322-34331.
157. J. Xie, A. D. Sendek, E. D. Cubuk, X. Zhang, Z. Lu, Y. Gong, T. Wu, F. Shi, W. Liu and E. J. Reed, *ACS Nano*, 2017, **11**, 7019-7027.
158. M. Mäntymäki, K. Mizohata, M. J. Heikkilä, J. Räisänen, M. Ritala and M. Leskelä, *Thin Solid Films*, 2017, **636**, 26-33.
159. Y. Sun, G. Bian, W. Tao, C. Zhai, M. Zhong and Z. Qiao, *Calphad*, 2012, **39**, 1-10.
160. X. Meng, Y. Sun, S. Yuan, Z. Ma, Y. Wang and Z. Qiao, *Calphad*, 2006, **30**, 301-307.
161. A. Miura, N. C. Rosero-Navarro, A. Sakuda, K. Tadanaga, N. H. H. Phuc, A. Matsuda, N. Machida, A. Hayashi and M. Tatsumisago, *Nat. Rev. Chem.*, 2019, **3**, 189-198.
162. L. Zhou, K.-H. Park, X. Sun, F. Lalère, T. Adermann, P. Hartmann and L. F. Nazar, *ACS Energy Lett.*, 2019, **4**, 265-270.
163. E. Rangasamy, Z. Liu, M. Gobet, K. Pilar, G. Sahu, W. Zhou, H. Wu, S. Greenbaum and C. Liang, *J. Am. Chem. Soc.*, 2015, **137**, 1384-1387.
164. Z. Liu, W. Fu, E. A. Payzant, X. Yu, Z. Wu, N. J. Dudney, J. Kiggans, K. Hong, A. J. Rondinone and C. Liang, *J. Am. Chem. Soc.*, 2013, **135**, 975-978.

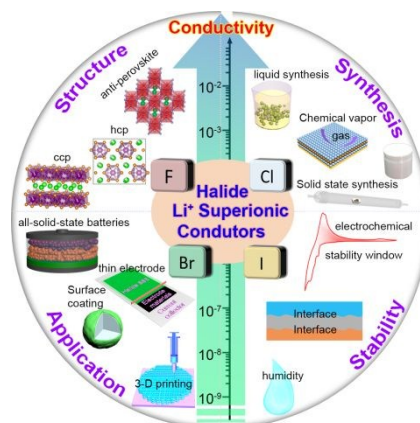
165. S. J. Sedlmaier, S. Indris, C. Dietrich, M. Yavuz, C. Dräger, F. von Seggern, H. Sommer and J. Janek, *Chem. Mater.*, 2017, **29**, 1830-1835. View Article Online
DOI: 10.1039/C6EE03828K
166. E. M. Kartzmark, *Can. J. Chem.*, 1977, **55**, 2792-2798.
167. E. M. Kartzmark, *Can. J. Chem.*, 1980, **58**, 539-545.
168. J. Wignacourt, G. Mairesse, P. Barbier, A. Lorriaux-Rubbens and F. Wallart, *Can. J. Chem.*, 1982, **60**, 1747-1750.
169. K. Yamada and A. Weiss, *Ber. Bunsen Ges. Phys. Chem.*, 1983, **87**, 932-944.
170. H. Schmidt, B. Euler, W. Voigt and G. Heide, *Acta Crystallogr. Sect. C*, 2009, **65**, i57-i59.
171. L. Zhou, J.-F. Liao, Z.-G. Huang, J.-H. Wei, X.-D. Wang, W.-G. Li, H.-Y. Chen, D.-B. Kuang and C.-Y. Su, *Angew. Chem. Int. Ed.*, 2019, **58**, 5277-5281.
172. L. X. Bai, X. Liu, W. Z. Wang, D. Z. Liao and Q. L. Wang, *Z. Anorg. Allg. Chem.*, 2004, **630**, 1143-1146.
173. M. Khelifi, R. Zouari and A. Ben Salah, *Acta Crystallogr. Sect. E: Struct. Rep.*, 2008, **64**, i80-i80.
174. A. W. Kelly, A. Nicholas, J. C. Ahern, B. Chan, H. H. Patterson and R. D. Pike, *J. Alloy. Compd.*, 2016, **670**, 337-345.
175. J. Lu, Q. Zhang, J. Wang and F. Saito, *J. Am. Ceram. Soc.*, 2004, **87**, 1814-1816.
176. G. Meyer and M. S. Wickleder, *Handbook on the Physics and Chemistry of Rare Earths*, 2000, **28**, 53-129.
177. R. H. Brugge, A. K. O. Hekselman, A. Cavallaro, F. M. Pesci, R. J. Chater, J. A. Kilner and A. Aguadero, *Chem. Mater.*, 2018, **30**, 3704-3713.
178. C. Galven, J. Dittmer, E. Suard, F. Le Berre and M.-P. Crosnier-Lopez, *Chem. Mater.*, 2012, **24**, 3335-3345.
179. X. Liu, Y. Chen, Z. D. Hood, C. Ma, S. Yu, A. Sharafi, H. Wang, K. An, J. Sakamoto, D. J. Siegel, Y. Cheng, N. H. Jalarvo and M. Chi, *Energy Environ. Sci.*, 2019, **12**, 945-951.
180. H. Muramatsu, A. Hayashi, T. Ohtomo, S. Hama and M. Tatsumisago, *Solid State Ionics*, 2011, **182**, 116-119.
181. Y. Tian, Y. Sun, D. C. Hannah, Y. Xiao, H. Liu, K. W. Chapman, S.-H. Bo and G. Ceder, *Joule*, 2019, **3**, 1037-1050.
182. A. Hayashi, H. Muramatsu, T. Ohtomo, S. Hama and M. Tatsumisago, *J. Mater. Chem. A*, 2013, **1**, 6320-6326.
183. H. Wang, Y. Chen, Z. D. Hood, G. Sahu, A. S. Pandian, J. K. Keum, K. An and C. Liang, *Angew. Chem. Int. Ed.*, 2016, **55**, 8551-8555.
184. A. Banerjee, K. H. Park, J. W. Heo, Y. J. Nam, C. K. Moon, S. M. Oh, S.-T. Hong and Y. S. Jung, *Angew. Chem. Int. Ed.*, 2016, **55**, 9634-9638.
185. T. W. Kim, K. H. Park, Y. E. Choi, J. Y. Lee and Y. S. Jung, *J. Mater. Chem. A*, 2018, **6**, 840-844.
186. W. D. Richards, L. J. Miara, Y. Wang, J. C. Kim and G. Ceder, *Chem. Mater.*, 2016, **28**, 266-273.
187. S. P. Culver, R. Koerver, W. G. Zeier and J. Janek, *Adv. Energy Mater.*, 2019, **9**, 1900626.
188. X. Han, Y. Gong, K. Fu, X. He, G. T. Hitz, J. Dai, A. Pearse, B. Liu, H. Wang, G. Rubloff, Y. Mo, V. Thangadurai, E. D. Wachsman and L. Hu, *Nat. Mater.*, 2016, **16**, 572.

189. A. M. Nolan, Y. Zhu, X. He, Q. Bai and Y. Mo, *Joule*, 2018, **2**, 2016-2046. View Article Online
DOI: 10.1039/C9EE03828K
190. K. Takada, N. Aotani, K. Iwamoto and S. Kondo, *Solid State Ionics*, 1996, **86**, 877-882.
191. Y. Gao, D. Wang, Y. C. Li, Z. Yu, T. E. Mallouk and D. Wang, *Angew. Chem. Int. Ed.*, 2018, **57**, 13608-13612.
192. C. Wang, K. R. Adair, J. Liang, X. Li, Y. Sun, X. Li, J. Wang, Q. Sun, F. Zhao and X. Lin, *Adv. Funct. Mater.*, 2019, **29**, 1900392.
193. Y. Seino, T. Ota, K. Takada, A. Hayashi and M. Tatsumisago, *Energy Environ. Sci.*, 2014, **7**, 627-631.
194. S. Boulineau, M. Courty, J.-M. Tarascon and V. Viallet, *Solid State Ionics*, 2012, **221**, 1-5.
195. T. Hakari, M. Deguchi, K. Mitsuhashi, T. Ohta, K. Saito, Y. Orikasa, Y. Uchimoto, Y. Kowada, A. Hayashi and M. Tatsumisago, *Chem. Mater.*, 2017, **29**, 4768-4774.
196. Y. Zhang, R. Chen, T. Liu, B. Xu, X. Zhang, L. Li, Y. Lin, C.-W. Nan and Y. Shen, *ACS Appl. Mater. Interfaces*, 2018, **10**, 10029-10035.
197. F. Han, T. Gao, Y. Zhu, K. J. Gaskell and C. Wang, *Adv. Mater.*, 2015, **27**, 3473-3483.
198. W. Zhang, T. Leichtweiß, S. P. Culver, R. Koerver, D. Das, D. A. Weber, W. G. Zeier and J. Janek, *ACS Appl. Mater. Interfaces*, 2017, **9**, 35888-35896.
199. A. Kajiyama, K. Takada, T. Inada, M. Kouguchi, S. Kondo, M. Watanabe and M. Tabuchi, *Solid state ionics*, 2002, **152**, 295-302.
200. I. D. Gocheva, S. OKADA and J.-i. YAMAKI, *Electrochem.*, 2010, **78**, 471-474.
201. C. Yang, J. Chen, X. Ji, T. P. Pollard, X. Lü, C.-J. Sun, S. Hou, Q. Liu, C. Liu and T. Qing, *Nat.*, 2019, **569**, 245.
202. K. Giagloglou, J. L. Payne, C. Crouch, R. K. Gover, P. A. Connor and J. T. Irvine, *J. Electrochem. Soc.*, 2018, **165**, A3510-A3516.
203. H. Zhang, Y.-N. Zhou, Q. Sun and Z.-W. Fu, *Solid State Sci.*, 2008, **10**, 1166-1172.
204. E. Gonzalo, A. Kuhn and F. Garcia-Alvarado, *J. Electrochem. Soc.*, 2010, **157**, A1002-A1006.
205. N. Twu, X. Li, C. Moore and G. Ceder, *J. Electrochem. Soc.*, 2013, **160**, A1944-A1951.
206. C. Yan, R. Xu, J.-L. Qin, H. Yuan, Y. Xiao, L. Xu and J.-Q. Huang, *Angew. Chem. Int. Ed.*, 2019, **58**, 15235-15238.
207. L. Liu, J. Xu, S. Wang, F. Wu, H. Li and L. Chen, *eTransportation*, 2019, **1**, 100010.
208. S. Chen, C. Niu, H. Lee, Q. Li, L. Yu, W. Xu, J.-G. Zhang, E. J. Dufek, M. S. Whittingham and S. Meng, *Joule*, 2019, **3**, 1094-1105.
209. J. Liu, Z. Bao, Y. Cui, E. J. Dufek, J. B. Goodenough, P. Khalifah, Q. Li, B. Y. Liaw, P. Liu and A. Manthiram, *Nat. Energy*, 2019, **4**, 180-186.
210. H. Li, *Joule*, 2019, **3**, 911-914.
211. Z. Jiang, S. Wang, X. Chen, W. Yang, X. Yao, X. Hu, Q. Han and H. Wang, *Adv. Mater.*, 2019, **31**, 1906221.
212. D. H. Kim, H. A. Lee, Y. B. Song, J. W. Park, S.-M. Lee and Y. S. Jung, *J. Power Sources*, 2019, **426**, 143-150.

213. Y. E. Choi, K. H. Park, D. H. Kim, D. Y. Oh, H. R. Kwak, Y.-G. Lee and Y. S. Jung, *ChemSusChem*, 2017, **10**, 2605-2611. View Article Online
DOI: 10.1039/C6SC03828K
214. K. H. Park, D. Y. Oh, Y. E. Choi, Y. J. Nam, L. Han, J. Y. Kim, H. Xin, F. Lin, S. M. Oh and Y. S. Jung, *Adv. Mater.*, 2016, **28**, 1874-1883.
215. Y. J. Nam, S.-J. Cho, D. Y. Oh, J.-M. Lim, S. Y. Kim, J. H. Song, Y.-G. Lee, S.-Y. Lee and Y. S. Jung, *Nano Lett.*, 2015, **15**, 3317-3323.
216. S. Yubuchi, S. Teragawa, K. Aso, K. Tadanaga, A. Hayashi and M. Tatsumisago, *J. Power Sources*, 2015, **293**, 941-945.
217. F. Han, Y. Zhu, X. He, Y. Mo and C. Wang, *Adv. Energy Mater.*, 2016, **6**, 1501590.
218. R. Murugan, V. Thangadurai and W. Weppner, *Angew. Chem. Int. Ed.*, 2007, **46**, 7778-7781.
219. A. R. Polu, D. K. Kim and H.-W. Rhee, *Ionics*, 2015, **21**, 2771-2780.
220. A. R. Polu and H.-W. Rhee, *Int. J. Hydrog. Energy*, 2017, **42**, 7212-7219.

Table of Contents

This review focus on the fundamental understanding, various and the newly promising liquid-phase (especially water-mediated) synthesis route, chemical/electrochemical stability of halide-based lithium superionic conductors, and their potential applications in energy storage as well as the related challenges.



The development of rechargeable batteries with high specific energy and extended cycling lifetime is required to satisfy the stringent demands of large-scale energy-storage devices and consumer electronics. All-solid-state lithium batteries (ASSLBs) utilizing solid-state electrolytes (SSEs) rather than combustible liquid electrolytes are considered as one of the most promising energy storage technologies due to improved safety and high energy densities. Among the various SSEs, halide-based SSEs have attracted increasing attention for their high Li^+ conductivity, wide electrochemical stability windows, and good compatibility toward oxide cathodes. In this review, we present a comprehensive overview of the recent developments and understandings of halide-based SSEs. We also focus on synthetic strategies of highly conductive halide-based SSEs from traditional solid-state reaction to liquid-phase synthesis methods. The significant advantages, challenges, and opportunities of halide-based SSEs have been presented. The rational design of halide-based SSEs with high Li^+ conductivity, good chemical/electrochemically stability and mass-production synthesis route will lead to new highly attractive SSEs for ASSLBs. The perspectives of current challenges and future directions, as well as prospects for practical applications of halide-based SSEs are also proposed.